EXAMINATION OF THE IMPACT OF HELMETS ON THE LEVEL OF TRANSFERRED

LOADS TO THE HEAD UNDER BALLISTIC AND BLAST LOADS

A Dissertation
Submitted to the Graduate Faculty
of the
North Dakota State University
of Agriculture and Applied Science

By

Mehdi Salimi Jazi

In Partial Fulfillment of the Requirements
of the Degree of
DOCTOR OF PHILOSOPHY

Major Department:
Mechanical Engineering

December 2014

Fargo, North Dakota

North Dakota State University
Graduate School

Title

Examination of the Impact of Helmets on the Level of Transferred Loads to the
Head Under Ballistic and Blast Loads

By

Mehdi Salimi Jazi

The Supervisory Committee certifies that this ***disquisition*** complies with North Dakota

State University's regulations and meets the accepted standards for the degree of

DOCTOR OF PHILOSOPHY

SUPERVISORY COMMITTEE:

Dr. Ghodrat Karami

Co-Chair

Dr. Fardad Azarmi

Co-Chair

Dr. Annie Tangpong

Dr. Mariusz Ziejewski

Dr. M. Abdelrahman

Approved:

7/10/2015	Dr. Gary Smith
Date	Department Chair

ABSTRACT

The main causes of human Traumatic Brain Injuries (TBIs) in war zones are ballistic impacts and blast waves. While understanding the mechanism of TBI and the brain injury thresholds are in urgent needs, efficiency of helmets as injury protective is not well-examined. To address these gaps, this study investigates the impact of ballistic helmets and padding systems on the biomechanical responses of the brain under dynamic ballistics and blasts loads. A nonlinear human head-neck finite element modeling procedure has been employed for the analysis. The results are examined against de-facto standard experimental data. The response of the finite element head model (FEHM) in terms of biomechanical parameters of the brain has been examined to measure the influence of padding system materials on the level of the loads transferred to the head. The results show when a bullet hits the front of the helmet vertically, the brain experiences the highest amount of stresses in comparisons with other impact orientations. Also, low stiffness foams cause less amount of load to be transferred to the head, indicating the importance of the mechanical properties of the padding system in helmet design.

Parametric studies have also been carried out to examine the efficiency of the helmet under various blast situations and intensities by varying standoff distances and orientation angles of the FEHM. The results indicate that the protected heads experience lower accelerations, and stresses than unprotected heads. In general it was found that the performance of the helmet depends on the extent of the coverage of the head by helmet.

To examine the influence of the entire human body in comparison with the only head model, the torso and attached to the head was modeled and the responses of the brain to equivalent loadings were examined. In general for the first few milliseconds of the assault on the head, biomechanical parameters of the brain remain independent of the torso. However, one can

see the body influence as times goes by. As a conclusion one can rely on the results of the head

and neck model to be credible enough for brain injury analysis.

ACKNOWLEDGMENTS

I would like to express my sincere appreciation my advisors Dr. Ghodrat Karami and Dr. Fardad Azarmi for their continuous support, encouragement, and valued advice through this research. Their extensive knowledge and vision have been the source of motivation in this research. I would like to thank Dr. Mariusz Ziejewski for his help and guidance. His creative thinking and vision have been a wonderful source for our group. I would also express my gratitude to my committee members Dr. Annie Tangpong and Dr. Magdy Abdelrahman. I would like to thank my friends in the Mechanical Engineering Department who have been there for me. Also thanks to all my friends who helped me stay sane through these difficult years. Their support and care helped me overcome setbacks and focused on my study. I greatly value their friendship and appreciate their belief in me. I am also grateful for the Army Research Office (ARO) for the financial support of this work.

DEDICATION

I would like to dedicate this thesis

To my family for their unconditional and continuous support, and to the memory of my father.

TABLE OF CONTENTS

LIST OF TABLES

LIST OF FIGURES

LIST OF EQUATIONS

1. INTRODUCTION

1.1. Importance of Traumatic Brain Injury

Traumatic Brain Injury (TBI) is one of the major sources of disability and death in the world. Over time, there has been considerable research and interest in studying TBI both in medical and biomechanical fields. While medicines are considered the pathological and physiological remedy, researchers could learn and understand the mechanism of TBI by considering the biomechanical responses of the brain under the external loads. Engineers study the physical phenomena of the injury using the principles of mechanics to quantify the source of brain injury due to impact loads to provide protective equipment and consequently reduce the level of the brain injury. Currently, a large number of literatures are available to explain the mechanisms of different types of TBI. TBI can be classified in several ways according to the purpose of study and available data.

One simple method of categorizing TBI is to open and close injury relating to the skull fracture. Open, or penetrating, TBI happens when the skull is broken and usually a specific area of the brain is damaged due to the penetration. However, the skull would not be fractured due to external impact force and close TBI still can happen. Close TBI can happen at several parts of the brain under such circumstances which is known as a diffuse damage. The close TBI often occurs because of rapid kinematical motions of the human brain in the skull. Despite the fact that the skull protects the brain against external forces, the opposite is also true. Outside of the skull is hard and strong, but the interior surface of the skull has many sharp edges. The brain is a soft material floating in cerebrospinal fluid (CSF). External loads push the brain to move forward or backward or even rotate in the skull cavity. The brain hits the sharp edges in the interior surface which leads to bruising, bleeding, and destruction of nerve cells. The damaged part of the brain

corresponding to the impact area is known as coup injury. If the impact force is large enough to move the brain to hit the opposite site of the skull, contrecoup injury can also occur. Localized or diffuse damage and coup or contrecoup injuries can happen independently or together under some circumstances. When a moving object strikes the skull, the initial coup injury will be more substantial than the secondary, contrecoup injury. On the other hand, when the moving skull strikes a fixed object, the contrecoup injury will be more significant than the initial coup injury. Different injury and consequences may happen corresponding to the area that is damaged. Human brain is divided into two hemispheric sides that interact with the opposite side of the body, so the right part of the brain controls the left side of the body and vice versa. Each hemisphere is divided into four parts, or lobes, which are called as frontal, temporal, parietal, and occipital lobes (Figure 1-1) [1]. Each lobe controls different tasks. Thus, injury of each part has different sings as below:

1.1.1. Frontal lobe injury

This lobe controls several elements including creative thought, problem solving, intellect, judgment, behavior, attention, abstract thinking, physical reactions, muscle movements, coordinated movements, smell and personality. Behavioral problems and cognitive are the consequences of the injury of this part of the brain.

1.1.2. Temporal lobe injury

 The temporal lobe controls visual and auditory memories. It includes areas that help manage some speech and hearing capabilities, behavioral elements, and language. Short term memory difficulties, loss of the sense of smell and/or taste, and vestibular difficulties are typical results of injury of the temporal lobe. The patient usually is not able to perform multiple tasks simultaneously.

2

1.1.3. Parietal lobe injury

Visual functions, language, reading, internal stimuli, tactile sensation and sensory comprehension will be monitored here. Human sense of touch and is controlled by this part of the brain. Parietal lobe plays an important role in our ability to read as well. Injury to parietal lobs affect verbal memory and the ability to remember series of digits [2].

1.1.4. Occipital lobe injury

The occipital lobe is located in the back of the head. It helps to control vision. The occipital lobe is the primary area of the brain involved in the processing of visual information. Injury to occipital lobe reduce the ability of detecting movements of the objective correctly and makes the vision blurry.
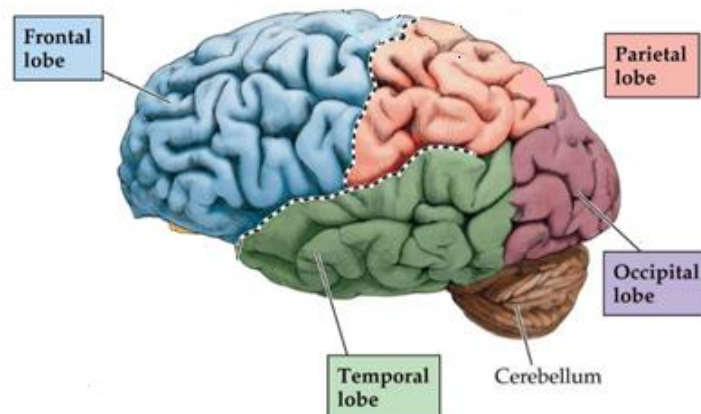
Figure 1-1. Different parts of the brain [1].

TBI can be also classified based on the severity of the injury. Several parameters affect the severity of TBI. For instance, injuries to occupants of vehicles are directly related to at least three key factors: (1) the mass of the vehicles involved in the impact; (2) the change of the velocity during the impact; (3) and the use of safety equipment that controls the occupants' movements [3]. The intensity of TBI is categorized into mild, moderate, and severe, depending on the severity of the injury:

- Mild TBI: Typically a few seconds loss of consciousness, but normal brain imaging;

- Moderate TBI: Unusual brain imaging and loss of consciousness for a long time, but less than 24 hours;

- Severe TBI: Irregular brain imaging and loss of consciousness for more than 24 hours (or coma).

The majority of TBIs that happen each year are in the form of concussions [4]. In the USA, more than 1.7 million people experience different levels of TBIs every year [5]. The most common causes of brain injury in civilians are crashes due to falls, motor vehicle collisions, violence related injuries, and collisions in sports (Figure 1-2) [4]. Among all people suffering TBI in the USA around 20% to 25% experience moderate or higher TBIs that may cause permanent disabilities and death. The remaining 80% to 75% TBI cases are mild one from which a person can recover in most cases [4]. According to the Center for Disease Control (CDC) from 2006 to 2010 around one-third of fatalities in the USA have been due to TBI among all kind of injuries. Moreover, some people experience physical or psychological problems such as aggressive social behavior, impaired abilities (thinking, language, learning, emotions, behavior, sensation), and neuro-degenerative diseases (epilepsy, Alzheimer's disease, Parkinson's disease) as direct results of TBI or poor treatment after that [4].
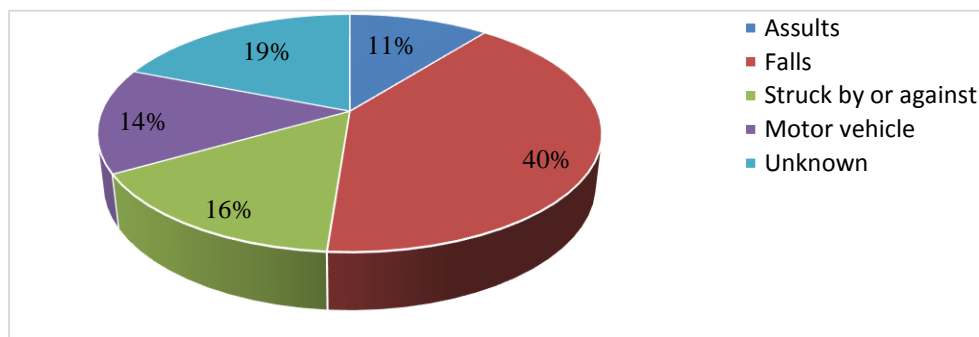
Figure 1-2. Common causes of TBI, during 2006-2010 (Data based on [4]).

The majority of TBI in combat zones are due to exposure to the shock waves resulting from explosions, debris and fragmentations, and ballistic impact. Since parameters such as intensity level and type of the transferred load to the head due to the different impact incidents govern the mechanism of the brain injury, the mechanisms of TBI that happen in war zones are different from those that occur in civilians. During the Iraq and Afghanistan wars, mild TBI has become a considerable issue for the US military service. The head and neck typically correspond to 12% of the volume of the body; however, it receives up to 25% of all "strikes" in the combat zone. The Defense Medical Surveillance System (DMSS) reported that significant numbers of military personnel have been affected by various levels of TBIs each year (Figure 1-3) [6]. DMSS data shows that there were over 280,000 different types and levels of TBIs among the US service members from 2000 to first quarter 2014 (Figure 1-4) [6].
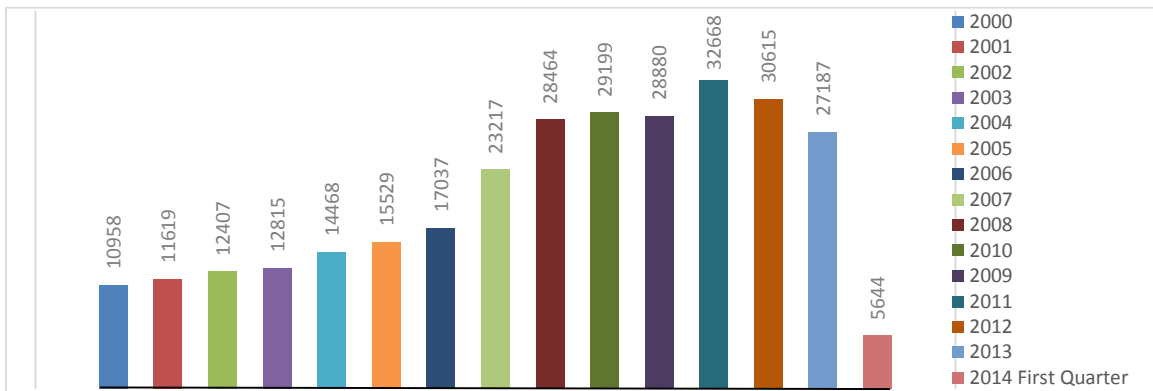
Figure 1-3. Annual total number of TBIs in the U.S. Army (Data based on [6]).

PENETRATING

275, 288, 239, 283, 358, 322, 337, 402, 463, 506, 301, 324, 205, 155, 19

SEVERE

178, 188, 153, 173, 162, 190, 216, 236, 260, 342, 252, 261, 247, 162, 21

MODERATE

1616, 1681, 1448, 1435, 1581, 1629, 1645, 2261, 1972, 1920, 1886, 1857, 1733, 1751, 362

MILD

7179, 8299, 9645, 10272, 11924, 12894, 14537, 19849, 23025, 23995, 25158, 27535, 26127, 22764, 4701

Legend: 2000, 2001, 2002, 2003, 2004, 2005, 2006, 2007, 2008, 2009, 2010, 2011, 2012, 2013, 2014 First Quarter

Figure 1-4. Different types and levels of TBI in the U.S. Army from 2000 to May 2014 (Data based on [6]).

In the cases of direct impacts, as it happens during sports and motor vehicle crashes (MVCs) or because of fragmentation and ballistic impact, TBI is a stress dominated phenomenon which is resulted from direct contact loads and mainly depends on the intensity of the transferred load to the head. As an example, if the front of the head is hit, the brain contacts the skull at the frontal region and a positive pressure, known as the intracranial pressure (ICP), forms in the frontal area of the brain which is also known as coup site pressure. These compressive loads squeeze the brain tissue and can cause permanent damage to the brain. Because of the relative displacement of the brain to the skull, the pressure in the fluid that surrounds the brain, changes

and cavitation in occipital region of the brain can happen. The cavitation phenomenon is, indeed, due to negative pressure at the occipital region that is known as contrecoup site pressure. Tensile loads may stretch the brain tissue. Contrecoup site pressure may also happen because of the relative movements of the brain and skull and their contact in the form of compressive loads (Figure 1-5). Moreover, during an impact a portion of brain can slide over other portions leading to shear forces. Shear stresses result in Diffuse Axonal Injury (DAI) [7].

(A)   (B)
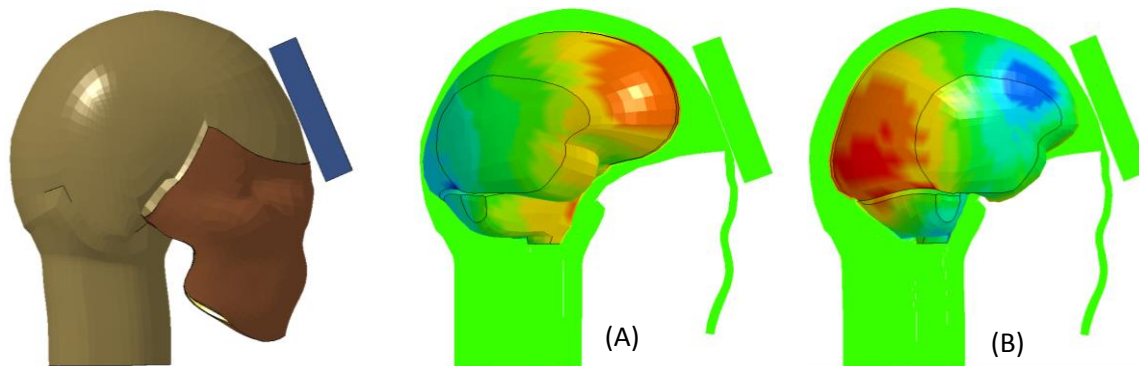
Figure 1-5. Pressure on the brain in (A) coup and (B) contrecoup sides due to direct impact.

In 1943, Holbourn [8] recognized that the angular acceleration of the head is the main cause of the relative displacement of the brain and skull. Holbourn stated that the angular acceleration of the skull causes the tensile and shear stress in the brain leading to the diffuse brain injuries. Ommaya et al. [9, 10] concluded that the rotational movement of the skull is more important than its linear movement. Since measuring the head angular acceleration is a difficult task, considering the linear acceleration of the head is still known as the main criterion to assess the level of the brain injury.

Several methods have been proposed to estimate the level of the TBI and various criteria have been established based on the mechanical and kinematical responses of the skull and brain. These criteria are used as safety limits in designing protective equipment such as helmets. Maximum translational acceleration with dwell times, severity index (SI), rotational acceleration

combined with variations of rotational velocity, generalized acceleration model of brain injury threshold (GAMBIT) and head injury criterion (HIC) have been developed based on the linear/angular accelerations and the duration of the acceleration. Various TBI's criteria and their application are presented in Table 1.1. Head injury criterion (HIC) is the most common head injury condition. HIC was introduced by Gurdijan et al. [11] as a human head tolerance limit indicator. HIC predicts head injury due to the impact with flat objects. HIC is measured as a relationship between an average translational anterior-posterior acceleration level and the duration of the acceleration pulse. In this criterion, the fracture tolerance of the skull is assumed equivalent to the tolerance of brain injury. HIC is often used in the diagnoses of TBIs which may occur as the result of many different types of accidents, including motor vehicle collisions, slips, falls, construction site injuries, and airplane or train accidents.

Table 1.1. Different TBI criteria and their typical applications.

Method	Threshold	Application
Maximum linear acceleration [12]and[13]	$A_{max} < N$	Helmet standards
Maximum linear acceleration and time[14]NHTSA Standard 218, 1997	$a_m < 400\ G$ time at 200G < 2 msec time at 150G < 4 msec	NHTSA for the US motorcycle helmet standard
Average acceleration and time duration[15]	$a^{-2.5}T < 1000$	
The Severity Index SI[16]	$\int_T a^{2.5} dt < N$	NOCSAE standard
The Head Injury Criterion [13]NHTSA, 1972	$[1/(t_2 - t_1) \int_{t_1}^{t_2} a(t)dt]^{2.5}(t_2 - t_1)] < 1000$	FMVSS 218, and is now the most widely referenced head injury assessment function
Angular acceleration combined with angular velocity change[17]	AIS Acceleration, rad/s2 Velocity Change, rad/s 0 <4500 <30 1 <1700 >30	
Angular and Linear acceleration GAMBIT[18]	$G_{max} = [(\frac{a_{res}(t)}{250})^2 + (\frac{\alpha_{res}(t)}{25000})^2]^{\frac{1}{2}}$	
Linear and rotational kinetic energy[19]	$HIP = Aa_x \int a_x\,dt + ba_y \int a_y\,dt + Ca_z \int a_z\,dt + \gamma\alpha_x \int \alpha_x\,dt + \beta\alpha_y \int \alpha_y\,dt + \delta\alpha_z \int \alpha_z\,dt$	

While actual brain damage happens at the cellular level as a result of strain and stresses in brain tissue, measuring the level of the injury based on global kinematic data is the biggest drawback of the HIC and other kinematic criteria to predict TBI. Moreover, under the high intensity impact loads such as exposure to blast waves, including extremely dynamic loads, a

complex mechanical and physical load will be introduced to the head. The head reactions, involving sudden acceleration or deceleration [20], volume changes of the intracranial contents, and even local skull flexure resulting in TBI due to the blast waves [21].

Several methodologies (experimental, mathematical, mechanical and computational) have been proposed to study the kinematical and mechanical responses of the head under different loading conditions to evaluate the level of brain injury and understand the mechanism of the TBI.

- Experimental tests which are investigating the level of brain injury on human volunteers, human cadavers, or animals are considered more reliable. However, these kinds of tests are difficult, expensive, and sometimes experimentally impossible. Human volunteer tests, for instance, cannot experience injury so the level of the impact load must be well below the critical level; cadaver tests are expensive; and scaling the animals' brain responses to humans is difficult.

- Theoretical models are considered as an alternative to experimental tests but they are limited to non-complex situations due to many simplifications required for modeling.

- Mechanical models or dummies are usually used in vehicle and safety device tests to model and record the head acceleration or deceleration, during motor vehicle crashes.

- Numerical or computational models are certainly excellent tools of determining the mechanical response of the head components such as stresses and strains under different types of higher level and more complex external loads. In comparison with experimental and/or mathematical methods, finite element (FE) human head models are widely used because variation and maximum amounts of stress, strain, and relative displacement of the FE head model components can be easily recorded under different initial or boundary

conditions as well as under various loading scenarios. Once the FE model is validated against experimental data, the model can become a reliable tool for understanding the injury's mechanisms which inform the design protective devices such as helmets. Stresses and strains recorded from FE solutions can be considered as the level of the injury compared against the proposed thresholds that are tabulated in Table 1.2.

Table 1.2. Proposed injury thresholds in the literature.

Parameter	Threshold
Intracranial pressure	235 KPa → injury [22] <173 KPa → minor or no injury
Strain	> 0.2 → cell injury [23] and [24] >0.25 →structural failure [25], [26], and [27] >0.20 → functional deficit <0.10 → reversible injury
Shear Stress	11-16.5 KPa → injury[28] 8-16 KPa → injury [29]
Von Mises Stress	15-20 KPa → concussion [30] and [31]

1.2. Research Objectives

Helmets are highly effective in reducing the level of the transferred load to the head, wearing a helmet increases the safety and reduces the possibility and severity of TBI. Using helmets can protect the skull from direct impact and lessen the level of the transferred load to the brain and consequently reduces the severity of the injury. However, TBI can still occur due to the severity of the impact load and the relative movement of the brain with respect to the skull, even in the absence of a skull fracture [32-34].

The objective of this research is to develop a three dimensional (3-D) helmeted head-neck FE model including all essential components of the human head and neck, to monitor the biomechanical responses of the brain under different ballistic and blast wave loads. The objectives of the research are divided into three sections.

1- Study the kinematical and mechanical responses of the brain under the ballistic impacts to examine the effects of

- the material properties of padding system;

- the angle of the ballistic impacts; and

- the location of the ballistic strikes.

2- Study the brain's responses for a helmeted human head model under the blast scenarios and examine the effects of

- the padded helmet on safeguarding the brain; and

- the rest of the body and wash-over phenomenon with respect to the blast orientations.

3- Conduct experimental works with a shock tube setup to

- simulate the blast scenarios.

These objectives are conducted under defined loading scenarios. A non-linear explicit dynamics FE solver is employed to numerically simulate the loading environment as well as the brain interactions.

To examine the impact of helmets and padding system on the level of the transferred loads to the human head and brain under ballistic and blast loads, in this research, Hyper mesh FE software (Altair Hyper work 11, Altair Engineering, Troy, Michigan) is used to build, modify and mesh the human head model, the helmet and the padding systems. The ballistic and blast load scenarios are applied and solved using explicit solver LS-DYNA 971 package (Livermore Software Technology Corp., Livermore, California). Figure 1-6 showed the procedure of the work schematically. Simulations were carried out on a personal computer (Intel Core i7 CPU with 8 GB RAM).
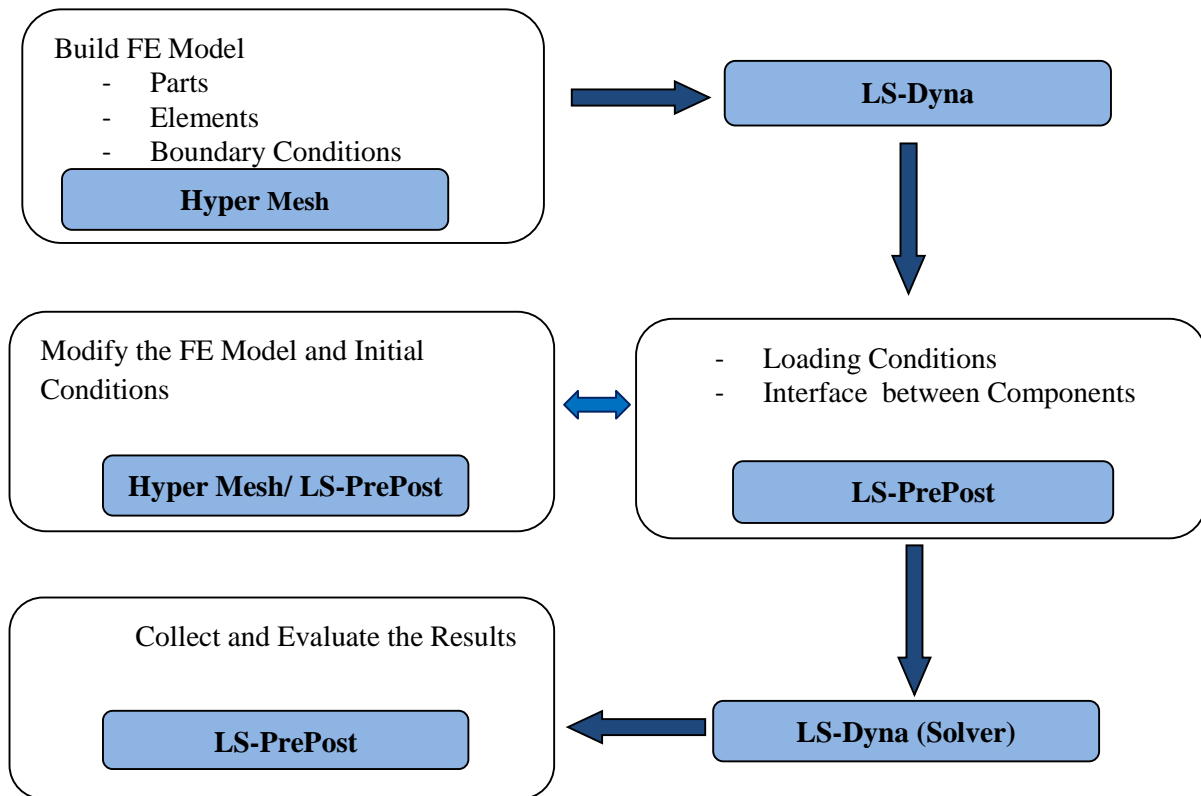
Figure 1-6. Modeling procedure in this research.

2. HUMAN HEAD FINITE ELEMENT MODEL

2.1. Anatomy of the Human Head and Neck

Head is sustained by the skull, which houses the brain. The brain controls movements and other actions of the body. The brain is immersed into the Cerebrospinal Fluid (CSF) and covered with dura and pia maters tissues, skull bone, and scalp (Figure 2-1) [35]. The scalp, the outermost component of the head, has a varying thickness of around 5 to 7 *mm*. As an absorber and distributer of energy over the skull thickness, insistence and stimulus of the scalp are major features that protect the skull against impact loads. The skull contains twenty two bones. Each skull bone, the stiffest protecting component of the head, is a sandwich structure with two inner and outer compact bone layers and a spongy bone between them as a core. The compact bone is stiffer than spongy bone and prevents penetration into the brain. Various shapes, thicknesses and arrangements of trabecula network build the spongy bone. The spongy bone damps the mechanical loads [36]. Brain is completely covered by pia mater and partly separated to the left and right hemispheres by falx. Tentorium, the lower separating membrane, separates the cerebrum from the cerebellum and brainstem. The gap between the pia mater and dura mater (skull) is filled with CSF which is a load damper that uniformly distributes the cranial pressure within the skull. It is a colorless liquid that contains water, protein, organic ingredients and gases. The brain, with its covering membranes and CSF, is connected to the spinal cord through the foramen magnum. The base of the skull is attached to the neck by articulation through occipital condyles, ligaments and muscles.
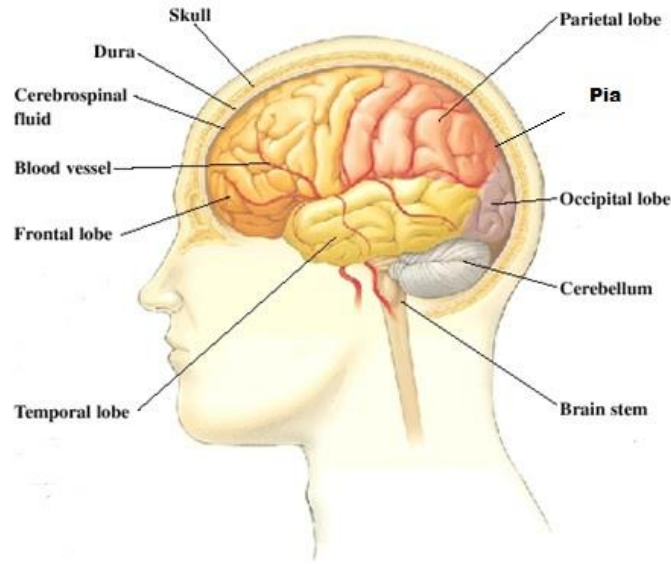
Figure 2-1. Anatomical structure of the head [35].

2.2. Finite Elements Modeling of the Head and Brain

2.2.1. Development of FE human head model

While finite element (FE) modeling has been extensively used in structural analysis areas from several years ago, the first finite element model of a human head was developed in the 1970s. With development of more advanced human head models, the complexity has gradually increased in terms of geometry and material properties of head components to address a close resemblance to the natural human head. Numerical simulations can present a good biofidelity. Once an FE model is validated the model can serve as a tool for assessment of the injury level. Modeling the head and studying the brain injury in biomechanical engineering analysis due to impact loads and blast waves have been the focus of much research work [37-42].

Anzelius [43] introduced the first mathematical model of the head. The model included a spherical fluid mass and the response of the liquid to a rapid velocity change were studied. He found that the positive pressure happened near to the impact area and negative pressure occurred at the contre coup position. He also found a node with zero pressure at the center of the mass.

15

Chan [44], Kenner and Goldsmith [45], and Khalil and Hubbard [46] modeled the first three dimensional models simply using a spherical, spheroidal or ellipsoidal shell for the skull. Hardy and Marcal [47],Hosey and Liu [48], Nickell and Marcal [49], Shugar [50], and Ward [51] used actual geometry of the human head to develop their model. However, their simplified human head model could only be used for the brain or the skull. In 1977, Nahum [52] developed a three dimensional FE head model to replicate the experimental impact tests carried out on cadaver heads. Their model was developed by using only 189 eight-node brick elements to create the skull and brain and 80 four-node shell elements to build the dura mater, falx and tentorium. To model the mechanical properties the skull and brain they applied linear elastic or linear viscoelastic equations, or considered brain as a fluid for their models. More details about the human head models can be found in Khalil and Viano [53] and Voo et al. [54].

In an effort to have a more realistic geometrical model, using more complex material properties, and meshing the model by a higher number of elements, modified FE models were introduced with the use of magnetic resonance imaging (MRI) and computer tomography (CT). Ruan et al. [55] introduced a head model including scalp, skull, cerebral spinal fluid (CSF), dura mater and brain with 7,351 elements. Zhou et al. [56] created a model with 22,995 elements to represent the scalp, skull, gray mater, white mater, brainstem, CSF, ventricles, venous sinuses, dura mater, falx, tentorium, and facial bones. Willinger et al. [57] created a finite element head model including the skull, brain, falx, and tentorium as well as a space filled with CSF simulated as a solid elastic layer. Five cadaver tests were simulated while skull was considered as a rigid structure. Velocity curves were applied to the skull and accelerations and intracranial pressures were compared with experimental data. There were some oscillations in their numerical outputs that were not detected in experimental data. However, acceleration responses showed a logical

agreement with the experimental data. The peak pressure values showed more discrepancies with the experimental values. And pressure curves showed similar trends. Kleiven and von Holst [58] built a parametric model to study the effects of different sizes of head geometry and various element meshes on head model impact response. They found that head model components are sensitive to mesh size and it is the meshing that defines the quality of the FE model. The geometry characteristics of the elements (e.g. aspect ratio's) are also important for accurate results. Moreover, type, order, and integration method of the elements all play major roles. In most FE head models mainly first order four-node shell elements and eight-node brick elements have been employed.

This research used a complex three directional (3D) FE head-neck model, including all major components of the human head (Figure 2-2). Magnetic resonance technology (MRT) has been used to capture the geometrical data of the head model. The model was created using 23,361 eight-node brick elements (solid elements) and 5,344 four-node shell elements (2D elements). The scalp has been modeled using two layers of solid elements. The facial bone and skull also were modeled using one layer and four layers of solid elements, respectively. The head membranes; dura mater, pia mater, falx and tentorium; were created by using 2D elements. Brain, neck, and CSF were also modeled using solid elements. Type and number of the elements of head components were tabulated in Table 2.1.
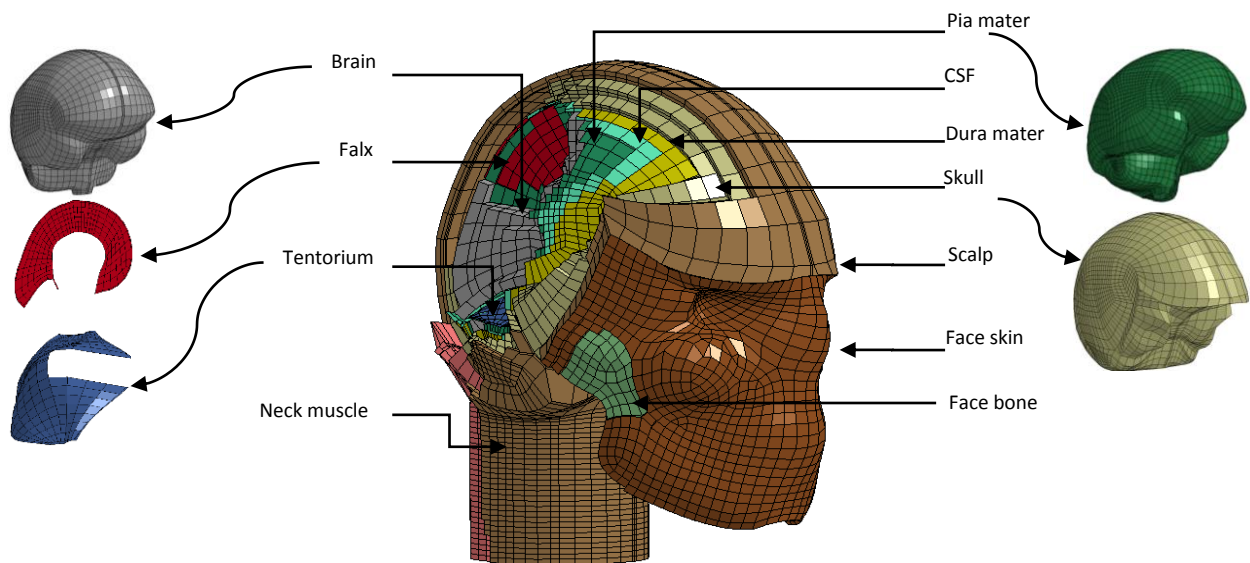
Figure 2-2. FE head-neck model components.

Table 2.1. Head-neck components FE Model.

Tissue	FE model	Number of Elements
Scalp	Solid element	8186
Skull	Solid element	8305
Falx	Shell element	2609
Tentorium	Shell element	2609
CSF	Solid element	3354
Brain	Solid element	7798
Facial bone and skin	Solid element	1124
Neck bone	Solid element	496
Neck muscle	Solid element	3772

2.2.2. Head component materials

Accurate characterization of the material properties of the head components has been

challenging for research on the biomechanics of the head. Different mechanical properties and

various constitutive equations can be found in literature, from simply linear elastic to complex

non-linear hyper-viscoelastic material.

18

Modeling the elastic material components: It is a widely accepted assumption for all solid components of the head, except CSF and brain, to have a linear elastic behavior. Dura mater, pia mater, tentorium, skull, scalp, and neck components are assumed as linear elastic materials in the present research. Accurate modeling of the linear elastic behavior needs three parameters to explain the physical response of a material, density of the material (ρ), and the Lamé parameters (λ) and (μ). The parameter λ describes the relationship between the Young's Modulus (modulus of elasticity), E, and Poisson's Ratio, ν.

To model the elastic material in LS-Dyna, only E, ν, and ρ are required. Studies have employed different values for head components' materials. For example, the elastic modulus and Poisson's ratio of scalp change from 16.7 to 34.5 *MPa* and 0.42 to 0.4 *MPa*, respectively. Mukherjee et al. [59] have summarized the variations of the mechanical properties of the human head components. In this work the average values of the mechanical properties for the elastic properties were used in the simulations (Table 2.2).

Table 2.2. Mechanical properties of the head components.

Tissue	Mechanical Properties		
	Density (*Kg/m³*)	Elastic Modulus (*MPa*)	Poisson's Ratio
Scalp and facial skin	1200	16.7	0.42
Skull	1800	15000	0.21
Dura, falx, tentorium	1130	31.5	0.45
Pia mater	1130	11.5	0.45
Neck and Facial bone	1300	1000	0.45
Neck muscle	1130	0.1	0.24

Modeling the CSF: CSF can be considered to behave as a Newtonian fluid. Various material properties have been used to model it. Characterization of the mechanical property of CSF in experiment is difficult and cannot be done on cadavers. Hardy et al. [60] used re-

pressurized cadaver heads during the impact tests to simulate the CSF but it may raise questions in terms of accuracy of the results. Due to important role of CSF under the impact and shock wave loads and its damping property against sudden relative displacement of the brain relative to the skull, CSF should be modeled as accurate as possible [61]. Some researchers modeled the CSF simply by using mechanical and physical properties of the water. Taylor and Ford [62] modeled the mechanical behavior of the CSF utilizing a nonlinear equation-of-state. Some other researchers, however, modeled the CSF as a linear elastic material having a high bulk modulus and low shear modulus [61, 63]. To model the mechanical behavior of the CSF with Lagrangian solid element, elastic fluid-type material was selected with no capability of bearing sheer stress but capable to carry the compressive hydrostatic stress [63-64]. In the research work presented here, elastic-fluid type material was used to model the mechanical behavior of the CSF. The constitutive equation for CSF is as follows [64]:

$$\dot{p} = -K\dot{\varepsilon}_{ii} \quad \text{and} \quad K = \frac{E}{3(1-2\nu)} \tag{2-1}$$

This equation relates the variations of the pressure ($\dot{p}$; the pressure rate) to the bulk modulus (K) which was obtained by Kleiven and Hardy [65], and the deviatoric strain rate ($\dot{\varepsilon}$). While the shear modulus is assumed to be zero, deviatoric stress at time step $n+1$ (S_{ij}^{n+1}) is determined as follows:

$$S_{ij}^{n+1} = V_c \Delta L a \rho \dot{\varepsilon}_{ij}' \tag{2-2}$$

Where V_c is the viscosity coefficient (generally between 0.1 and 0.5), ΔL is a characteristic element length, a is the fluid bulk sound speed, ρ is the fluid density and $\dot{\varepsilon}_{ij}'$ is deviatoric strain rate. The mechanical properties of the CSF were illustrated in Table 2.3.

Table 2.3. Mechanical properties of CSF.

Constitutive model	Mechanical Properties			
	Density (Kg/m^3)	Elastic Modulus (*MPa*)	Bulk Modulus (*MPa*)	Poisson's ratio
Fluid Type- elastic	1040	1.488	2190	0.4887

Modeling the brain; experimentally, brain tissue can be characterized as incompressible, non-linear and viscoelastic material. Accurate constitutive modeling of brain tissue is a major concern in human head FE modeling. In some earlier human head models, the brain was simply modeled as a linear elastic material while later models represented the brain with the viscoelastic constitutive laws [55, 56, 66]. In studies by Kleiven et al. [58, 65, 67], and Chafi et al. [68], rate-dependent Mooney-Rivlin hyperelastic constitutive law, based on the work of Mendis et al. [69], was used to model brain tissue under large nonlinear deformations. The use of a nonlinear material model, however, largely depends on the evaluation of constitutive properties from physical tests. In this research, the brain tissue was modeled as a homogenous and isotropic material. Linear viscoelastic material was implemented as follows [40, 70]:

$$G(t) = G_\infty + (G_0 - G_\infty)e^{-\beta t} \tag{2-3}$$

Where G_0 and G_∞ are the short-term and long-term shear modules, respectively, and β is the decay factor. Under the blast load scenarios, the mechanical properties of the brain were assumed as a viscoelastic material with the Mooney–Rivlin hyper-elastic behavior. The Mooney-Rivlin model explains the strain energy density (SED) function as follows:

$$W = \sum_{i+j=1}^{N} C_{ij}(J_1 - 3)^i (J_2 - 3)^j \tag{2-4}$$

In this equation W is the strain energy density; C_{ij} is material constant parameter; J_1 and J_2 are the first and second invariants of the deviatoric strains, respectively.

21

To consider the viscoelastic behavior, the SED must be related to the time. For this reason, the coefficients C_{ij} have been defined similarly to the stress relaxation function in linear viscoelastic theory. A possible form of the relaxation functions of the time dependent coefficients of the SED is a Prony series defined as:

$$C_{ij}(t) = C_{ij}^{\infty} + \sum_{k=1}^{M} C_{ij}^{*k} e^{-t/\tau_k} \tag{2-5}$$

C_{ij}^{∞} is the steady state of the coefficient that is determined from a quasi-static test. Substituting equation (2-5) into equation (2-4) and using a convolution integral leads to the time dependent or visco-Mooney-Rivlin SED:

$$W(t) = \int_0^t \left[\sum_{i+j=1}^{N} C_{ij}(t-\tau) \frac{d}{d\tau} \left\{ (J_1(t)-3)^i (J_2(t)-3)^j \right\} \right] d\tau \tag{2-6}$$

In 1995, Mendis et al. [69], model index N is equal to 1. SED function (*W*) is related to Green-Lagrange strain tensor (***E***), i.e.,

$$E = \frac{1}{2}\left(F^T.F - I\right) \tag{2-7}$$

Where ***F*** is deformation tensor as related to the material coordinate system. The 2nd-Piola-Kirchhoff strain tensor P is defined as:

$$P = \rho_0 \frac{dW(E)}{d(E)} \tag{2-8}$$

In terms of the right Cauchy-Green strain tensor $C = F^T.F$ the 2nd-Piola-Kirchhoff strain tensor can be rewritten as:

$$P = \rho_0 \frac{dW(E)}{d(E)} = \rho_0 \frac{dW(C)}{dC}.\frac{dC}{dE} = 2\rho_0 \left[\frac{dW}{dJ_1}\frac{dJ_1}{dC} + \frac{dW}{dJ_2}\frac{dJ_2}{dC} + \frac{dW}{dJ_3}\frac{dJ_3}{dC} \right] \tag{2-9}$$

And the Cauchy stress tensor now can be derived

$$\boldsymbol{\sigma} = det(\boldsymbol{F})^{-1}\boldsymbol{F}.\boldsymbol{P}.\boldsymbol{F}^T \qquad (2\text{-}10)$$

Material properties of the brain adapted from Mendis et al. [69] were presented in Table 2.4 and Table 2.5.

Table 2.4. Mechanical properties of viscoelastic brain material.

Density (Kg/m^3)	Bulk Modulus (*GPa*)	Short-term Shear Modulus (*kPa*)	Long-term Shear Modulus (*kPa*)	Decay Factor (ms^{-1})
1040	0.128	528	168	0.7

Table 2.5. Hyper-viscoelastic material properties of the brain.

Density (Kg/m^3)	k	τ_k (s)	C_{01}^{*k} (*Pa*)	C_{10}^{*k} (*Pa*)
1040	∞	∞	689.4	620.5

2.3. Modeling the Contacts between the Head Components

The interfaces between the head components affect the accuracy of the biomechanical responses of the brain. Defining appropriate contact conditions between several components allows Lagrangian elements to interact with each other without merging or penetration. There are many conditions in which two or more components come in contact during loading. Although in many engineering problems most contact processes are naturally dynamic, many of them can be simplified as quasi-static. Contact problems are essentially nonlinear and involve unknown boundary conditions. Compared to general engineering problems, contact analysis is extremely difficult to solve because of their complex nonlinearities. Dynamic contact which happens in a short period is called impact-contact. Ballistic impact is a good example for high velocity impact while body falling on the ground surface can be considered as an example of low velocity impact. It is difficult to accurately define specific points on different bodies come to contact with

23

each other during impact. Friction is always an important parameter for contact. However, the simplest contact model is frictionless, small-displacements, and elastic contact [71].

Much research has been conducted to determine formulations and find solution methods for a proper analysis of the contact problems. In general, the difficulty of contact problems is not only the governing equations belong to a space domain but also specifying an accurate time domain. Although research in contact analysis has a long history, numerical approaches have been applied recently and a number of formulations have been presented.

A large number of contact types are available in LS-Dyna. Tied contact are used to transfer both tension and compression loads from the master to the slave and vice versa. In this research tied node-to-surface contact has been employed for the interface between membrane components; falx, tentorium, and dura; and the brain. Tied surface-to-surface contact has been used between skull and scalp, dura and skull, pia and CSF as well as brain and pia.

2.4. FE Head Model Verification

Two methods are available to solve dynamic problems which are typically related to both space and time domains: explicit and implicit. In general, dynamic problems are solved using the following equation:

$$ma_n + cv_n + kd_n = f_n \tag{2-11}$$

In this equation *m, c, k,* and *f* are mass, damping stiffness matrices, and load vector respectively, and *n* is time step. To solve the equation, displacement (*d*) at time step *n+1* must be calculated. LS-Dyna is a non-linear transient dynamic finite element code developed by the Livermore Software Technology Corporation (LSTC) with the ability to solve both implicit and explicit problems. While the implicit part can solve both dynamic and static problems, explicit part is just used when there is acceleration or a dynamic problem. In Explicit (dynamic) solver

both internal and external forces are implemented at nodes. Dividing nodal force by nodal mass estimates the nodal acceleration. The nodal displacement is calculated by integrating the acceleration over the time. The solution is completely stable and since the solution is solved for displacements at nodal points, the time step must allow the calculation to progress across all nodes of the element. This means that the element size and the stiffness of the material determine the time step. Indeed, the smallest element in the mesh combined with the softest material control the time step for the entire solution. In an implicit (dynamic or static) solution, a global stiffness matrix is calculated, inverted, and then applied to the out-of-balance nodal force to obtain a displacement increment. Equilibrium iterations are then required to arrive at an acceptable force balance. The time step size can be selected by the user in implicit solution. However, a substantial computation is required to form, store, and factorize the stiffness matrix in this method. The key point of this discussion is that the stiffness matrix has to be decomposed or inverted at each time step whereas in the explicit method, it is a running analysis where the stiffness terms are re-computed at each time step but no inversion is required.

Computational works must be validated against experimentally obtained data. For example Kleiven and Hardy [65] validated their FE head model against the relative movement of the brain and the skull obtained from the experimental data of Hardy et al. [72]. Ruan et al. and Horgan et al. [55, 63] validated their FE models against the experimental test results of Nahum [52]. The human head-neck model used in this work with the assumed contact conditions and material properties described before has been validated against experimental cadaveric impact test data. For this reason, the frontal side of the FE head model is hit by an impact load similar to the Nahum [52] experimental work, obtained from Willinger et al. [57] (Figure 2-3). The variation of the pressure in coup and countercoup sites (ICP) have been monitored and compared

against Nahum's experimental data. The FE results showed a good agreement with experimental data, as shown in Figure 2-4.
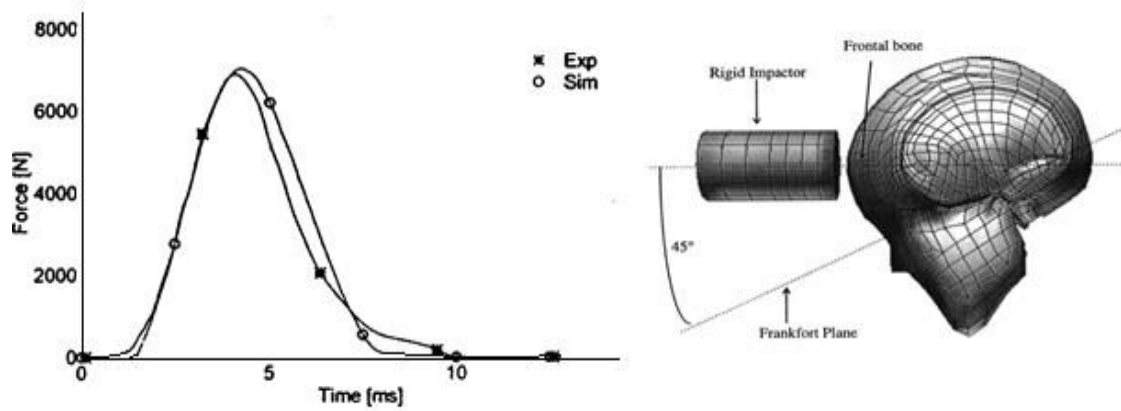
Figure 2-3. Nahum's experimental impact force.
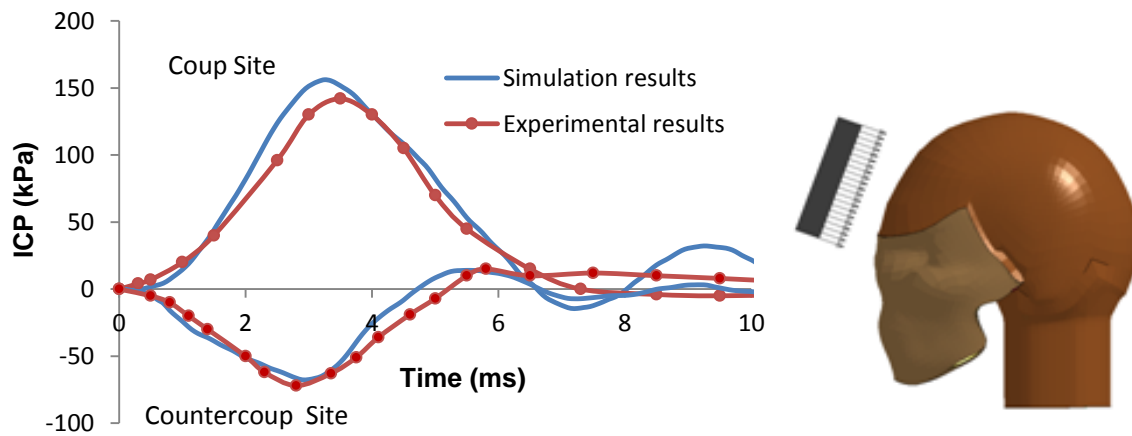
Figure 2-4. Comparison between the experimental data (from [52]) and predicted ones by simulation.

3. BALLISTIC HELMET AND HELMETED HEAD FE MODEL

The main purpose for wearing a ballistic helmet is to protect against direct hits such as ballistic impacts and flying objects. There is a long history in using helmets to protect the soldier's head in the war. It has been a common conclusion that the protection efficiency of ballistic helmet as well as ease of its employment for any particular application can be improved by tailoring its material and its shape according to the shape and geometry of the user's head. Since 1700, helmets made of materials such as leather, brass, bronze, and iron were widely used to protect soldiers from cutting blows with swords and flying arrows on the battlefield. The steel French Adrian introduced in 1915 is known as the first modern helmet. It was widely used during the Word War I [73]. The first US army helmet, called M1, was also made of steel. M1 helmets served the US soldiers not only during World War II but also kept in use for four decades afterwards [74]. In the mid of the 6th decade of last century ,concerning the material, ergonomic design, and protective aspects of the helmet, the M1 was finally replaced by the 29-layer Kevlar Personal Armor System of Ground Troops (PASGT) [75]. The introduction of composites in modern industry has definitely improved the overall character of the helmets. In 2003, PASGT helmet was replaced by a lighter Kevlar, called advanced combat helmet (ACH) [76]. Ballistic helmet made from composite material replaced conventional metal helmets because of reduced mass and improved the ballistic resistance (Figure 3-1).

Figure 3-1. Ballistic Helmets; (A) French Adrian [73], (B) M1[74], (C) PASGT [75], and (D) ACH helmets [76].

Ballistic woven fabrics are mainly used to make the PASGT and ACH helmets. Due to the orthotropic properties and various failure criteria and constitutive equations of composite material used for ballistic helmet, analysis of the helmet response under impact loads is difficult. Involving high ballistic velocity impact, boundary conditions, geometry of the helmet and bullet, material of the projectile make the problem more complex [77]. Typically, helmets are made from two major components: the shell and the pads. The shell prevents penetration by external objects to the head, and also distributes the impact load across a wider area of the padding system in order to improve the energy absorbing capability of the pads. Energy absorbing materials such as foams are used as padding materials inside the helmets to decrease the amount of transferred load to the head. Combat helmets are largely used to protect the head against ballistic impact loads and shrapnel. The efficiency of a ballistic helmet is defined based on the velocity of the bullet at that possible penetrates the helmet 50% of the time.

3.1. Geometry and Material of FE Ballistic Helmet

In this research, the geometry of out surface of an advanced combat helmet (ACH) was measured accurately using a coordinate measuring machine. It was discretized into FE modeling using 3,768 eight-node brick elements into four layers (Figure 3-2). The shell of the helmet is made of woven fabric reinforced aramid laminates and is considered as a transversely isotropic material.
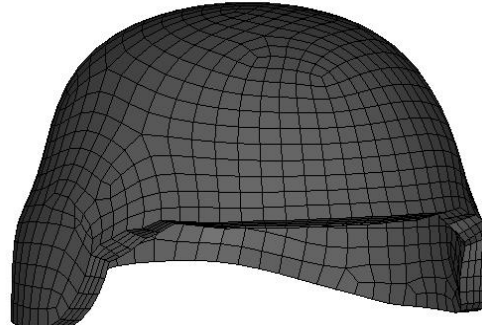
Figure 3-2. FE model of ACH ballistic helmet.

When the material properties are different in all directions and locations the material is considered as anisotropic and heterogeneous materials. However, using the Hook's law (linear relationship between stress and strain) is still acceptable to simplify the analyses. In a three dimensional orthogonal Cartesian coordinate system, the relation between stresses and strains is expressed as following:

$$[\sigma] = [C][\varepsilon]$$

$$
\begin{bmatrix} \sigma_1 \\ \sigma_2 \\ \sigma_3 \\ \sigma_4 \\ \sigma_5 \\ \sigma_6 \end{bmatrix} =
\begin{bmatrix}
C_{11} & C_{12} & C_{13} & C_{14} & C_{15} & C_{16} \\
C_{21} & C_{22} & C_{23} & C_{24} & C_{25} & C_{26} \\
C_{31} & C_{32} & C_{33} & C_{34} & C_{35} & C_{36} \\
C_{41} & C_{42} & C_{43} & C_{44} & C_{45} & C_{46} \\
C_{51} & C_{52} & C_{53} & C_{54} & C_{55} & C_{56} \\
C_{61} & C_{62} & C_{63} & C_{64} & C_{65} & C_{66}
\end{bmatrix}
\begin{bmatrix} \varepsilon_1 \\ \varepsilon_2 \\ \varepsilon_3 \\ \varepsilon_4 \\ \varepsilon_5 \\ \varepsilon_6 \end{bmatrix}
\tag{3-1}
$$

Because of symmetry of the stiffness matrix ([C]), it has 21 constants. In composite materials there are typically three perpendicular axes so that the material properties are different

along each axis. Therefore, composite materials are considered as orthotropic materials and only

nine constants are needed for their stiffness matrix. The orthotropic stiffness matrix is simplified

as follow:

$$[C] = \begin{bmatrix} C_{11} & C_{12} & C_{13} & 0 & 0 & 0 \\ C_{21} & C_{22} & C_{23} & 0 & 0 & 0 \\ C_{31} & C_{32} & C_{33} & 0 & 0 & 0 \\ 0 & 0 & 0 & C_{44} & 0 & 0 \\ 0 & 0 & 0 & 0 & C_{55} & 0 \\ 0 & 0 & 0 & 0 & 0 & C_{66} \end{bmatrix} \tag{3-2}$$

Replacing engineering constant in stiffness orthotropic stiffness matrix leads to:

$$[C] = \begin{bmatrix} \dfrac{1 - \nu_{23}\nu_{32}}{E_2 E_3 \Delta} & \dfrac{\nu_{21} + \nu_{31}\nu_{23}}{E_2 E_3 \Delta} & \dfrac{\nu_{31} + \nu_{21}\nu_{32}}{E_2 E_3 \Delta} & 0 & 0 & 0 \\ \dfrac{\nu_{12} + \nu_{13}\nu_{32}}{E_3 E_1 \Delta} & \dfrac{1 - \nu_{31}\nu_{13}}{E_3 E_1 \Delta} & \dfrac{\nu_{32} + \nu_{31}\nu_{12}}{E_3 E_1 \Delta} & 0 & 0 & 0 \\ \dfrac{\nu_{13} + \nu_{12}\nu_{23}}{E_1 E_2 \Delta} & \dfrac{\nu_{32} + \nu_{13}\nu_{23}}{E_1 E_2 \Delta} & \dfrac{1 - \nu_{12}\nu_{21}}{E_1 E_2 \Delta} & 0 & 0 & 0 \\ 0 & 0 & 0 & 2G_{23} & 0 & 0 \\ 0 & 0 & 0 & 0 & 2G_{31} & 0 \\ 0 & 0 & 0 & 0 & 0 & 2G_{12} \end{bmatrix} \tag{3-3}$$

$$\Delta = \frac{1 - \nu_{12}\nu_{21} - \nu_{23}\nu_{32} - \nu_{13}\nu_{31} - 2\nu_{12}\nu_{23}\nu_{13}}{E_1 E_2 E_3}$$

Transverse isotropic materials are special category of orthotropic materials. Transverse

isotropic materials exhibit same properties in one plane but different properties in normal

direction to the plane. Therefore the stiffness matrix can be described as below:

$$[C] = \begin{bmatrix} \dfrac{1 - \nu_{pt}\nu_{tp}}{E_p E_t \Delta} & \dfrac{\nu_p + \nu_{tp}\nu_{pt}}{E_p E_t \Delta} & \dfrac{\nu_{tp} + \nu_p \nu_{tp}}{E_p E_t \Delta} & 0 & 0 & 0 \\ \dfrac{\nu_p + \nu_{pt}\nu_{tp}}{E_t E_p \Delta} & \dfrac{1 - \nu_{tp}\nu_{pt}}{E_t E_p \Delta} & \dfrac{\nu_{tp} + \nu_{tp}\nu_p}{E_t E_p \Delta} & 0 & 0 & 0 \\ \dfrac{\nu_{pt} + \nu_p \nu_{pt}}{E_p{}^2 \Delta} & \dfrac{\nu_{tp} + \nu_{pt}\nu_{pt}}{E_p{}^2 \Delta} & \dfrac{1 - \nu_p{}^2}{E_p{}^2 \Delta} & 0 & 0 & 0 \\ 0 & 0 & 0 & 2G_{tp} & 0 & 0 \\ 0 & 0 & 0 & 0 & 2G_{tp} & 0 \\ 0 & 0 & 0 & 0 & 0 & \dfrac{E_p}{1 + \nu_p} \end{bmatrix} \tag{3-4}$$

$$\Delta = \frac{(1 + \nu_p)(1 - \nu_p - 2\nu_{pz}\nu_{zp})}{E_p{}^2 E_t}$$

In order to have a symmetric stiffness matrix following equations must be hold:

$$\begin{cases} \dfrac{\nu_p + \nu_{tp}\nu_{pt}}{E_p E_t \Delta} = \dfrac{\nu_p + \nu_{pt}\nu_{tp}}{E_t E_p \Delta} \\[2mm] \dfrac{\nu_{tp} + \nu_p\nu_{tp}}{E_p E_t \Delta} = \dfrac{\nu_{pt} + \nu_p\nu_{pt}}{E_p{}^2 \Delta} \\[2mm] \dfrac{\nu_{tp} + \nu_{tp}\nu_p}{E_t E_p \Delta} = \dfrac{\nu_{tp} + \nu_{pt}\nu_{pt}}{E_p{}^2 \Delta} \end{cases} \qquad (3\text{-}5)$$

Therefore, stiffness matrix of these kinds of material is described by just five independent engineering elastic constants ($E_{11} = E_{22} = E_p, E_{33} = E_t, \nu_p = \nu_{12}, \nu_{pt} = \nu_{tp} = \nu_{23}, and\ G_{tp} = G_{13}$). In this study material properties of the helmet adopted from van Hoof et al. [37] work and presented in Table 3.1.

Table 3.1. Mechanical properties of the helmet shell.

E_{11}=E_{22} (GPa)	E_{33} (GPa)	ν_{12}	ν_{23}= ν_{31}	G_{12} (GPa)	G_{13}= G_{23} (GPa)	Density (gr/cm^3)
18.5	6.0	0.25	0.33	0.77	2.715	1.23

E: Young's modulus, ν: Poisson's ratio; G shear modulus.

3.2. Padding System

One of the important components of any helmet is its padding system. Using the energy absorbing materials, pads in the helmets can considerably reduce the amount of transferred load. Foams are well known energy absorbing materials that are widely used in industry as well as in helmet pads. The padding efficiency, however, is widely dependent on its material, shape, geometry, and padding system layout. In this study pads are meshed with 8,663 brick elements filling the gap between the head and helmet's shell; as shown in Figure 3-3.
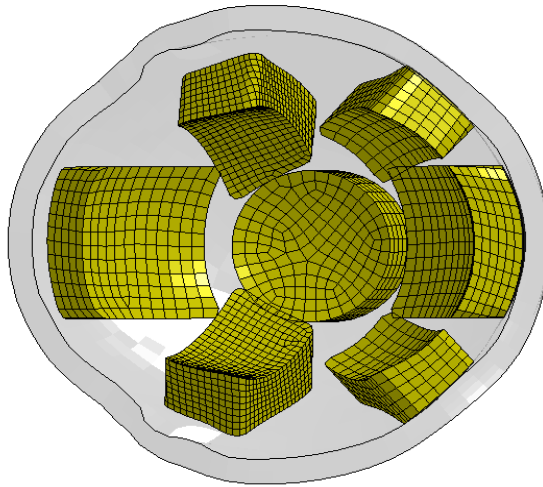
Figure 3-3. Meshed padding system layout.

Foam materials can undertake large compressive deformations and absorb great amounts of applied energy. The energy is damped by bending the cell, buckling or fracturing of the cell, and the stress is generally limited by the long and almost flat plateau of the stress-strain curve (Figure 3-4).
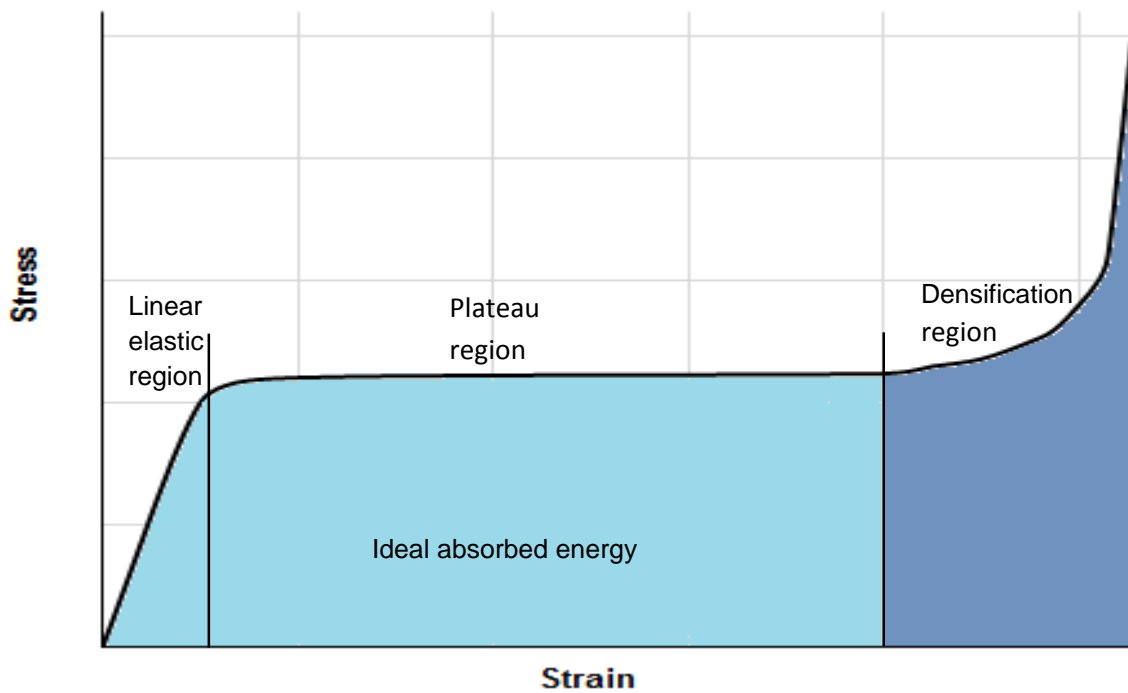
Figure 3-4. The engineering stress-strain behavior of foam material showing the initial linear, plateau and densification regions.

A typical engineering stress-strain curve of a foam material results from uniaxial compression of a specimen under a quasi-static loading. A typical stress-strain curve for foam materials can be divided to three specific regions known as: linear elasticity, plateau and densification as shown in Figure 3.4. The behavior of the foam is almost linear elastic at small strains, the slope of this part of the stress-strain curve is known as the Young's modulus of the foam [78]. Young's modulus of the foam highly depends on the density of the foam. The plastic behavior of the foams is characterized by the slope of the plateau region in the stress-strain curve. Although Gibson and Ashby [79] assumed that the stress remains constant in this region, dynamic and static compression tests on the foams show that the stress gradually increases in this region. The slope of the plastic plateau partly depends on the Young's modulus of the first part and, consequently, relates to the density of the foam. The collapse progresses at approximately a constant stress, until all cells and struts break, and densification causes the stress to increase sharply. The absorbed energy or the work done per unit volume to deform the foam is the area under the stress-strain curve. Because of the specific behavior of foam structure, it is the plateau region of the stress-strain curve that allows large energy absorption at approximately a constant load and just a small amount of energy is absorbed in the linear elastic region (ideal absorbed energy area in Figure 3.4).

Many experimental works have been carried out to characterize the impact properties of various types of cellular solid structure foam materials which are mainly employed for automotive applications [80-85] developed a generic FE model for an equestrian helmet made up of foam, and concluded that the acceleration of the head, due to impact in different loading conditions, is directly related to the contact area, the distribution of material stresses, and the dissipated plastic energy density.

The complete model of padding system and helmet were placed on the human head-neck FE model as shown in Figure 3-5. Automatic surface-to-surface contact algorithm was used to model the pads-scalp contact in absence of static friction coefficient, and tied surface-to-surface contact type was applied to attach the pads to the helmet.
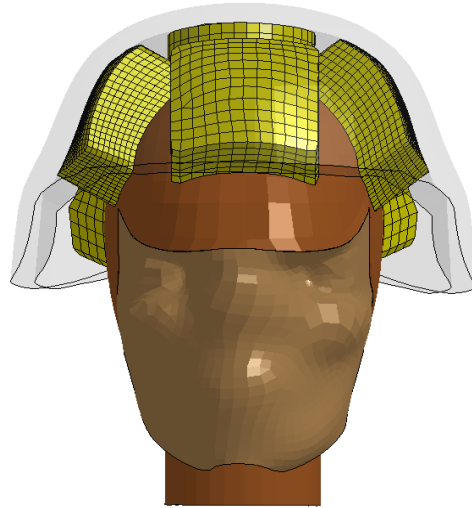
Figure 3-5. Helmeted human head-neck FE model.

4. BALLISTIC IMPACT

Ballistic impacts and exposure to the shock waves due to blasts are main causes of TBIs in the battlefields. In the last fifty years of research in the area of biomechanics, various computational modeling techniques have been used to determine the mechanical response of the head under different loading conditions. The biomechanical parameters determined from such simulations have been used to estimate the level of the brain injury [86]. Modeling the brain under high-velocity impact loads and shock wave loadings and diagnosis the brain injury have been a real challenge in computational biomechanics. Based on the velocity of the impacting material, impacts can be categorized into three different classes [87-89]:

- Low-velocity impact: It is considered as a low velocity impact if the contact time is more than the lowest vibrational mode's period. Under a low velocity impact, the boundary conditions of the impacted structural are important in order to examine the response of the structure to the impact accurately.

- High-velocity impact: In high velocity impacts (ballistic impact or blast wave loads) situation, the material behavior in the impacted region dominates the response of the structure to the impact load and the effect of the boundary conditions is not significant.

- Hyper-velocity impact: In a hyper-velocity impact situation, the material of the structure acts as a fluid in the impacted area and regions with very high stresses are created.

To reduce the severity of the brain injury wearing helmets have been recommended. Many researchers simulated the affectivity of the helmets on protection against brain injury for motor vehicles and motorcycle drivers and passengers [32-34, 90]. However, TBIs can still occur due to the size of the impact load and the sudden motions that are transferred to the brain.

Ballistic impacts can be classified as a high-velocity impact. When a projectile hits a helmet, a cone is formed on the inner face of the helmet's shell. The depth of this deformation must not exceed a critical value to protect the skull from the contact load. In another word, under heavy impact load energy, the shell of the helmet can deform and cause contact to the head from inside which can subsequently lead to head and brain injury known as rear effect [91, 92]. Baumgartner and Willinger [38] built a finite element model that included human head components and a helmet model made from aluminum subjected to impact by a steel bullet to study the rear effect. Qiu [93] studied the rear effect by considering the head response to the deformation that resulted by the ballistic impact to the KEVLAR helmet. Yang and Dai [94] used HIC to study the rear effect when the bullet strikes the composite helmets at different angels and at various locations. Their results showed that when the bullet hits the helmet perpendicularly, the level of the maximum pressure is the highest in the brain and the brain acceleration. [95] carried out experiments and simulations on the ballistic impact of a KEVLAR helmet. Their simulation results showed that a KEVLAR helmet can stop a 9 *mm* bullet traveling at 358 *m/s*. Othman [96] studied the ballistic resistance of four different composite materials when impacted by a bullet travelling at 360 m/s. He studied the effect of the mechanical properties of the composite materials such as shear modulus on the performance of the helmet. van Hoof et al. [37] carried out analysis on responses of woven composite helmet materials by experiments as well as by numerical modeling. They examined ballistic impact tests on flat panels made of identical material to that of the ballistic helmet. They also used the LS-Dyna finite elements to measure the penetration as well as the helmet backplane response. Aare and Kleiven [39] determined the effects of the shell stiffness on the level of the transferred load to the human head during impacts and also the effects of the impact angles on the load levels in the human head.

As mention before, the main role of pads is to absorb impact energy. Foam materials are widely used in packaging the fragile products and in protective applications such as helmets and knee pads. Because of their low density and high ability to absorb the energy, foams are also used as a core material for sandwich composite structures in navy, aircraft, and automotive applications [97]. In this research, a computational study of a helmeted human head was conducted to study the effect of the material properties of a helmet padding system on the level of stress in the brain due to a ballistic impact. Four different types of foam materials, made of expanded polystyrene (EPS) and expanded polypropylene (EPP) were examined. The effect of the padding system against different angles and directions of ballistic impacts as well as the location of the strike on the head for the pad material were examined.

4.1. Effect of Padding Materials

Many experimental works have been carried out to characterize the impact properties of various types of cellular solid structure foam materials which are mainly employed for automotive applications [80-83]. For instance, Rueda et al. [84] developed a generic FE model for an equestrian helmet made of foam, and concluded that the acceleration of the head, due to impact in different loading conditions is directly related to the contact area, the distribution of material stresses, and the dissipated plastic energy density.

Although some studies show the sensitivity of the foam to the strain rate [97], the effect of the strain rate was not taken into account in the study presented here in an effort to simplify the simulation. The selected foams in the work presented here were designated as A, B, C, and D with the respective densities of 31, 50, 70 and 100 kg/m^3. The mechanical properties of the selected foams were listed in Table 4.1 [84] and their stress-strain loading curves were plotted in

Figure 4-1. Low-density foam material models were selected to simulate the pads mechanical behavior.

Table 4.1. Mechanical properties of padding system material.

Foam	Type of the Foam	Density (kg/m^3)	Yield Strength (kPa)	Plateau Strength (kPa)
A	EPP*	31	100	100-250
B	EPS**	50	350	350-760
C	EPP	70	300	300-600
D	EPS	100	720	720-1510

*expanded polypropylene (EPP), **expanded polystyrene (EPS).
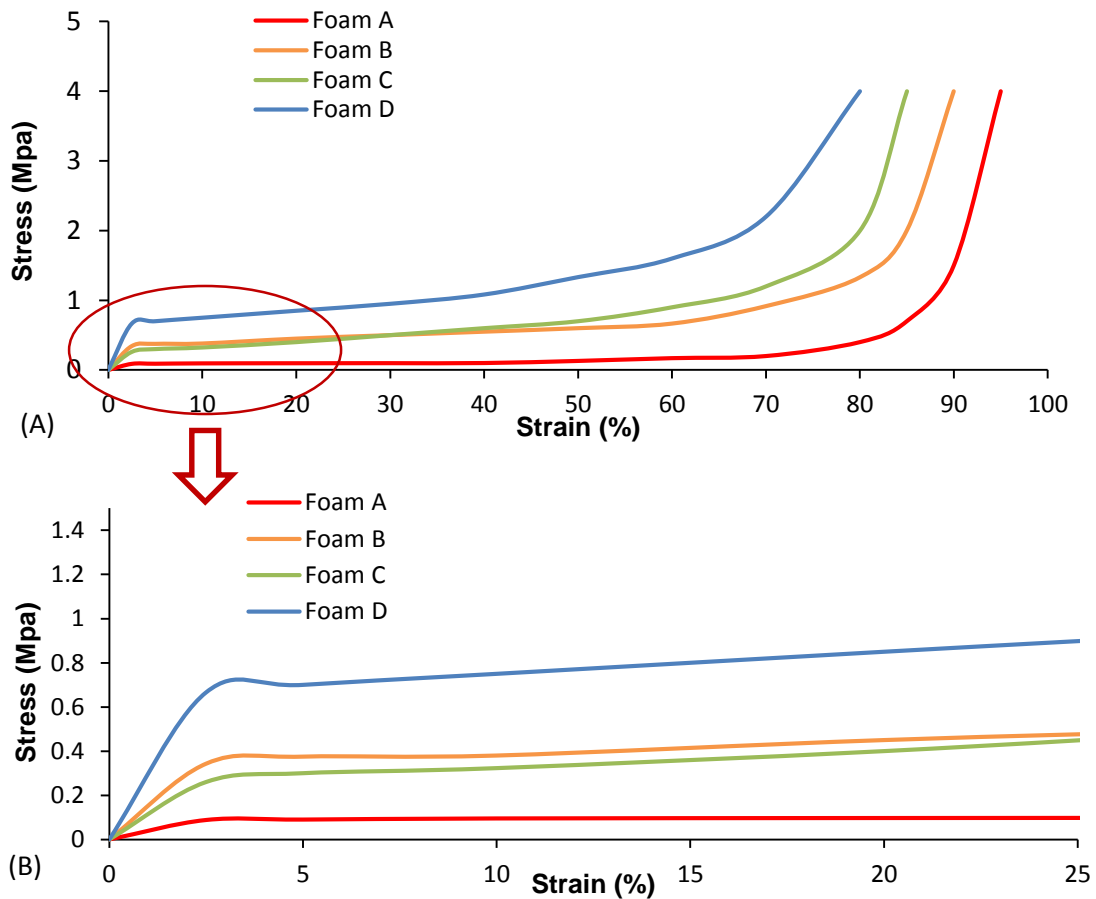
Figure 4-1. (A) Stress-strain behavior of the selected foams, (B) Magnified part of the stress-strain curve designated in (A).

To examine the effect of the material properties of the pads on the biomechanical responses of the brain, the human head covered with the helmet (Figure 4-2) was considered to be perpendicularly struck with a cylindrical bullet weighting about 8 grams. The velocity of bullet at the time of the impact was set 360 *m/s* for all of the foams.
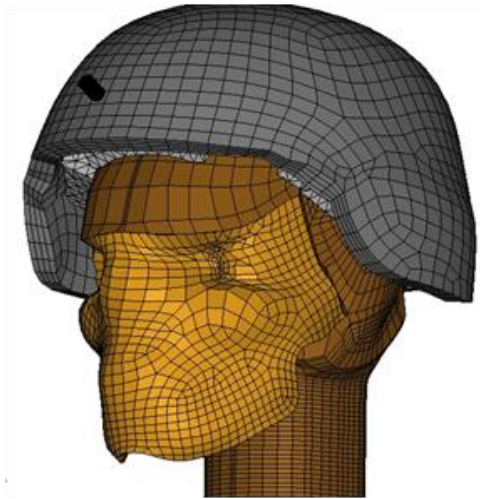
Figure 4-2. Helmeted head-neck FE model with the bullet just before the strike.

A portion of the kinetic energy of the penetrated bullet will be exhausted during fracture of the helmet in a ballistic impacts. In our analysis, the penetration was ignored, and a major part of the impact energy was dissipated through the large deformations of pads. The roles of pads were thus highlighted in non-penetration impacts. The response of the pads to the impact loading was evaluated based on the maximum volume change in the selected pad.

The percentage volume change of the frontal pad which was marked, was presented in Figure 4-3 (A). The reduction in the thickness of the frontal pad in the very neighborhood of the impact region was shown in Figure 4-3 (B). The pad in frontal region bore the maximum displacement because of its location to the striking point of the impact. The volume as well as the thickness reduction followed the same trend. As expected, the foam which had the lowest stiffness (Foam A) experienced the most volume and thickness reduction during the impact. The stiffest one had the lowest level of volume reduction and low thickness change. The percentage

of maximum volume reduction of the foams were 24%, 5%, 7%, and 2.4% in foams A, B, C, and D, respectively.
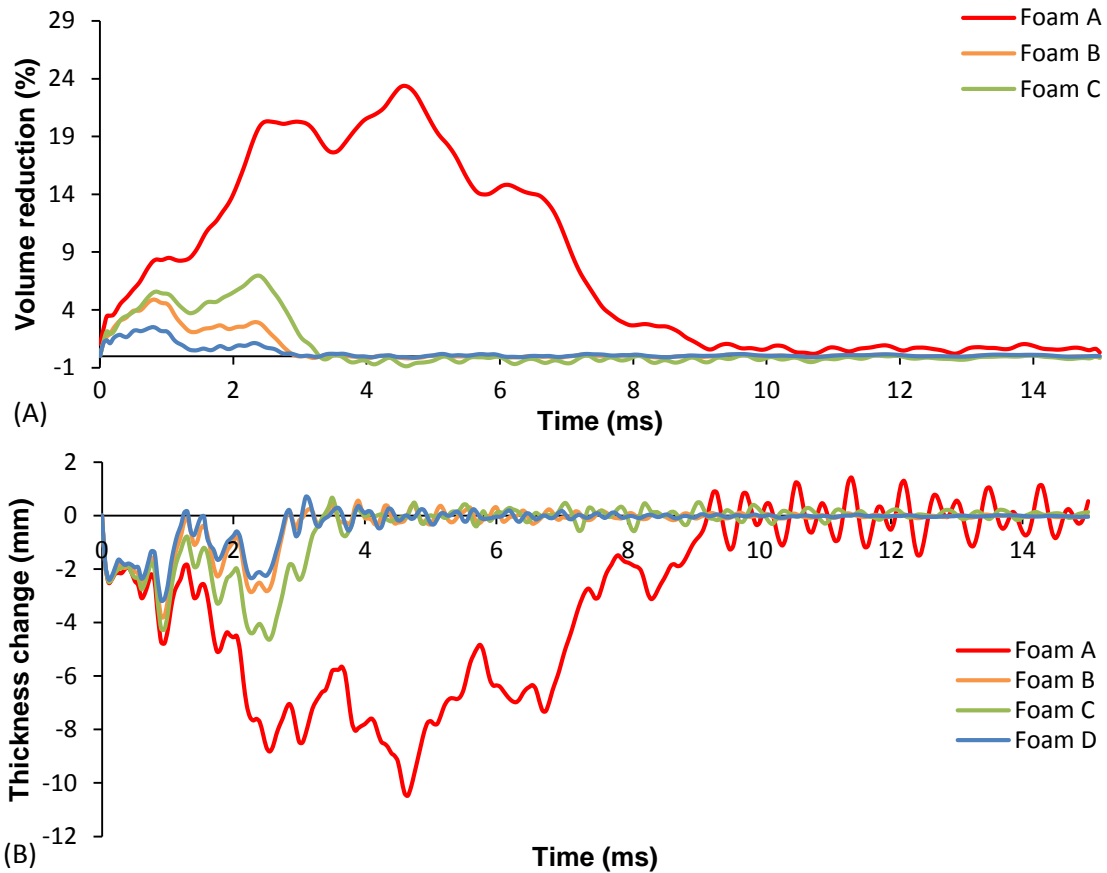
Figure 4-3. (A) The percentage in volume reduction of the front pad (as indicated) due to the bullet impact, (B) the variation in the thickness of the front pad.

The displacement on the backside region of the helmet shell due to the bullet impact was also calculated and plotted in Figure 4-4. The displacement of a particular small region on the backside of the helmet under the ballistic impact respect to time was shown in this figure. This region was opposed to the striking point on the front of the helmet. This plot was, in fact, the dynamic motion of the region which had the rigid motion of the entire body inherited, therefore, to find the relative backside displacement the rigid body motion should be deducted. Due to the inclusion of the rigid body motion, this displacement did not become zero with time. For the first few milliseconds, the response of the helmet for all types of pad materials were similar, but the

model with foam A experienced a larger displacement as time increased. Again as seen, the motion for foam A was the highest compared to other types of foams used for the padding system. The results of the analyses indicated that foam A experienced maximum volume and thickness reduction. This foam also experienced the highest level of the strain while foam D experienced the least amount of strain. Considering the stress-strain curves of the foams showed that the stress in foam A was less than others and the stresses in foams B and C were almost equal because they experienced strains lower than the tertiary region strains of the constitutive materials of the foam (Figure 4-1).
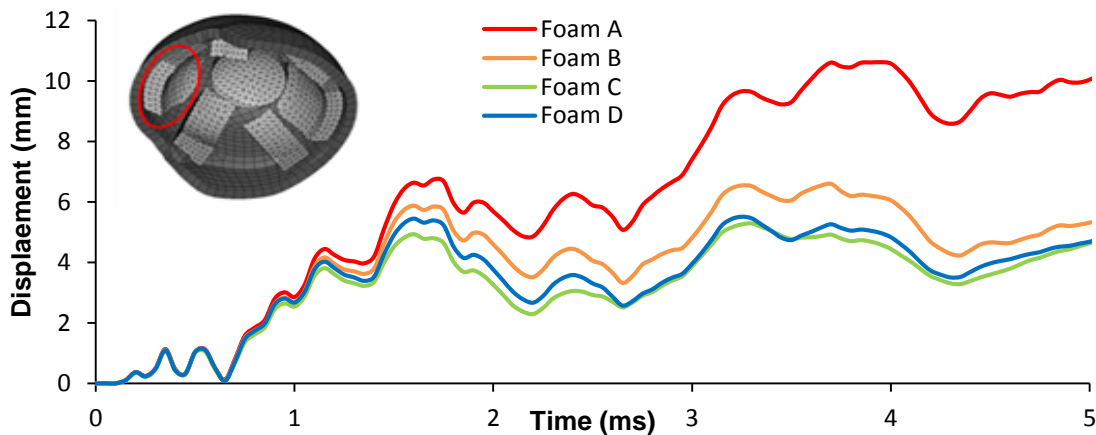
Figure 4-4. The displacement of the region on the backside of the helmet under ballistic impact with time.

Foam D only underwent elastic deformation and experienced the lowest volume change and very small strain during the impact. Since, it was assumed that the contact area between the pads and head were identical in all cases, the level of transferred load to the head, by using foam A, was the lowest because the stress experienced by this foam was the lowest. Figure 4-5 showed the plots of pressurized area at the striking point of the bullet on the helmet from the time of the impact up to several milliseconds after the strike. The peak pressures in elements were calculated in all the regions of helmet during impact. The average of the maximum pressures in this region

41

was around 390 *MPa* in all cases under a bullet velocity of 360 *m/s*. As expected, the average

pressure suddenly droped to a lower value, with time, and was finally tends to become zero.
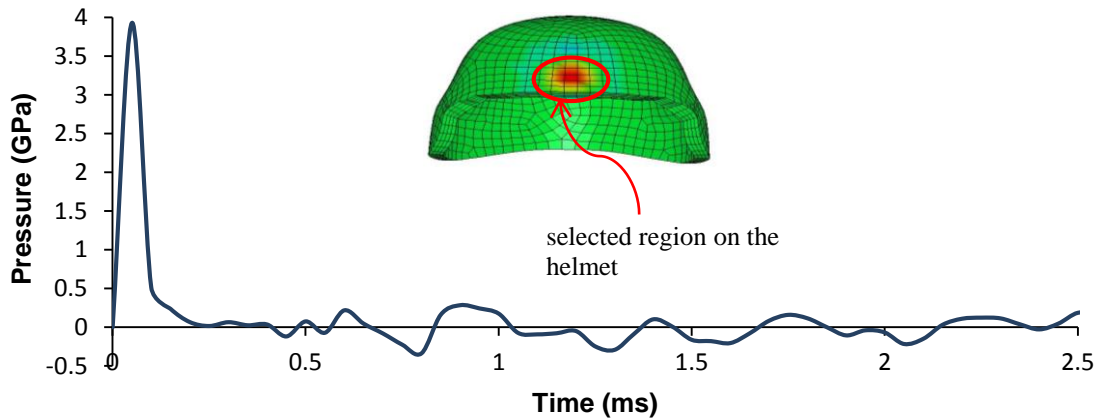
Figure 4-5. The pressure in the selected region of the helmet under the velocity of 360 *m/s*.

Few results can be found in literature for the ballistic experimental impact tests on the

head. The head acceleration and the maximum ICP in the brain were compared with Yang et al.

[98] results . They have studied rear effect of ballistic helmet impact using HIC in different

bullet impact angles. Presented results showed differences on the level of maximum ICP and

head acceleration from their results. This was expected as the geometry, size and materials were

different and no padding had been used in their simulation. The trend of the change in ICP and

acceleration however were close and reasonable agreements can be observed.

To better understand the effect of padding material on the brain's response under impact

loading, some parameters such as built-up pressure on the skull, center mass acceleration of the

brain, ICP, and maximum shear stress on the brain were selected for further evaluation. These

parameters played major roles in determining the level of brain injury. ICP is calculated from the

hydrostatic stress components at any desired point. ICP is responsible for any volume changes

and causes damage to the cellular elements of the brain. Maximum shear stress associated with

the deviatoric stresses, on the other hand, develops localized shear and tearing of the cellular

membranes of brain neurons [99]. The transferred pressures to the skull were also measured from this strike and presented in Figure 4-6. As the results showed, the amount of pressure was around 0.4, 1.18, 1.4, and 2.2 *MPa* for foams A, B, C, and D, respectively. The amount of maximum stress is usually bigger than the pressure (ICP), but usually remains within the same figure. This pressure can be simply tolorated by the skull having the compressive strenght of about 96 *MPa* [100]. Moreover, the time duration of impact load on the skull, for the case of less stiff foam, was the longest amongst the four different foams. Comparing Figure 4-5 and Figure 4-6 illustrated that in all cases, the level of the pressure decreased considerably as it transfered from the helmet to the skull.
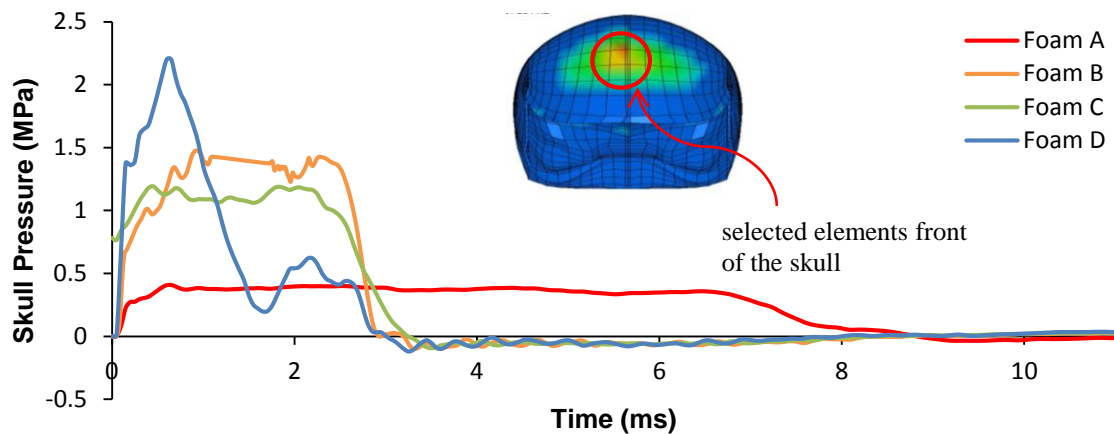
Figure 4-6. The transformed pressure to the skull with time in the selected region of the skull.

The impact load transferred to the head was the lowest in the case of foam A, since the center mass acceleration of the brain had the lowest value compared to the other foams. Figure 4-7 showed the center mass acceleration of the brain after the bullet struck the helmet. In all cases, brain experienced a rapid acceleration and then deceleration almost in the same time duration after the impact, but the level of the maximum acceleration in case A was considerably less than the other cases; it was about $20g$ versus $90g$, $70g$, and $117g$ for cases B, C, and D, respectively. In case A, the foam experienced a maximum volume reduction, and it took longer

time than other cases to reach the minimum volume and to recover to the original shape (Figure 4-3). Therefore, after experiencing the maximum acceleration, there was a gradually deceleration until the foam has returned to its original volume (around 8 millisecond). Other foams recovered faster than foam A in a noticeably shorter period of time, so, in these cases deceleration occurred much faster than case A (Figure 4-7).
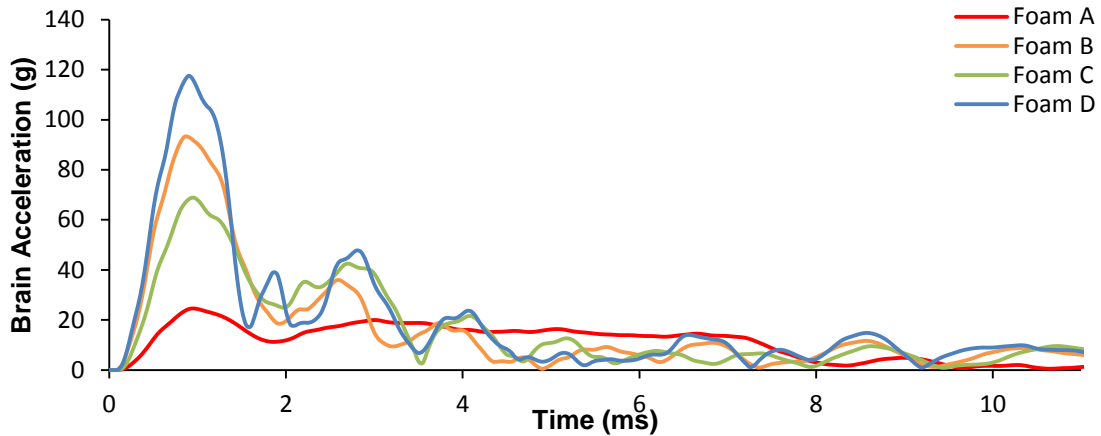
Figure 4-7. The acceleration of the center mass of the brain with time for the four different types of helmet pads (g=9.81 m/s^2).

Figure 4-8 showed the contour of the pressure at four different times; 0.15, 0.30, 0.65 and 8.30 milliseconds after the impact when foam A was used. As shown, the ICP wave was initiated at the corresponding area where the bullet hit the helmet and propagated around and inside the brain. Figure 4-9 and Figure 4-10. Selected elements were designated in Figure 4-8. These figures showed that the ICP and maximum shear stress increased as the center mass acceleration of the brain increased. The results contributed to the fact that foam A had a better performance in reducing the level of transferred load to the brain with less oscillation compared to other ones. Although no exact brain injury thresholds have been set with respect to maximum stresses, however, the examined ICPs tolerated by the brain in all models were less than the thresholds brain injury pressure of 235 *kPa* as proposed for low velocity impacts by Ward et al. [22].

t= 0.15 ms	
10.6	🟥
6.63	🟧
2.57	🟩
-1.17	🟦
-2.48	🟦

t= 0.30 *ms*	
11.5	🟥
7.06	🟧
2..6	🟩
-1.7	🟦
-3.23	🟦

t= 0.65 *ms*	
13.4	🟥
4.25	🟧
-4.55	🟩
-10.9	🟦
-17.1	🟦

t= 8.3 *ms*	
7.46	🟥
4.09	🟧
0.723	🟩
-1.52	🟦
-3.76	🟦
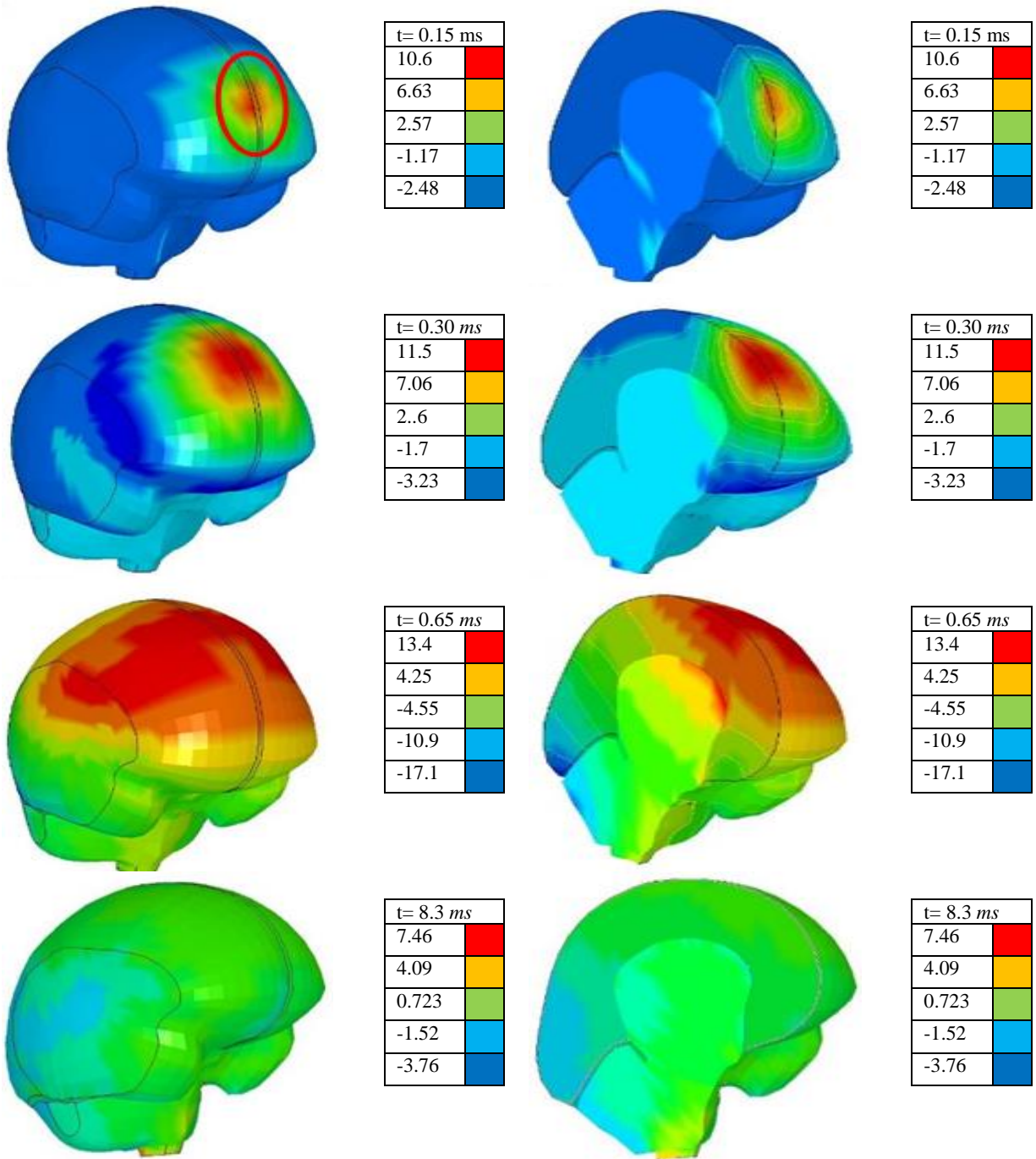
Figure 4-8. Contours of the pressure at: 0.15, 0.30, 0.65, and 8.3 milliseconds after the strike and the selected region located in frontal area of the brain to study ICP and maximum shear stress.
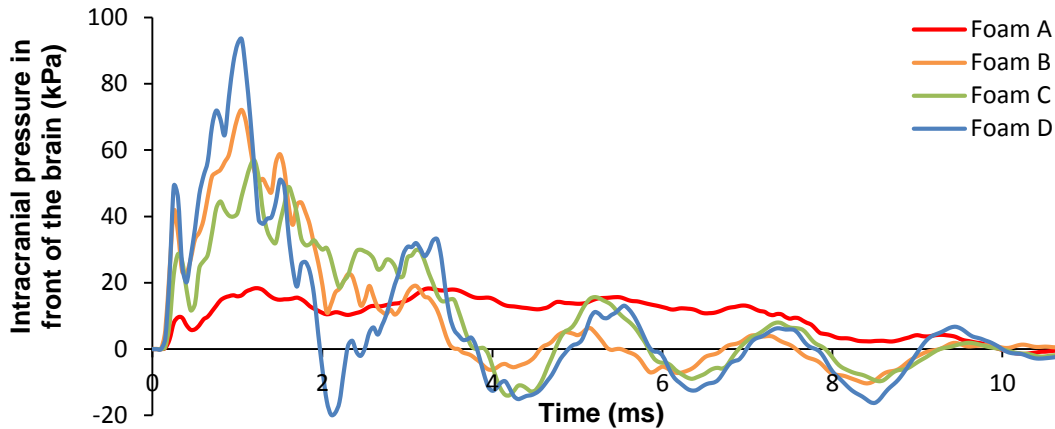
Figure 4-9. ICP generated due to bullet strike in the region on the front of the brain with time for the four different types of helmet pads.
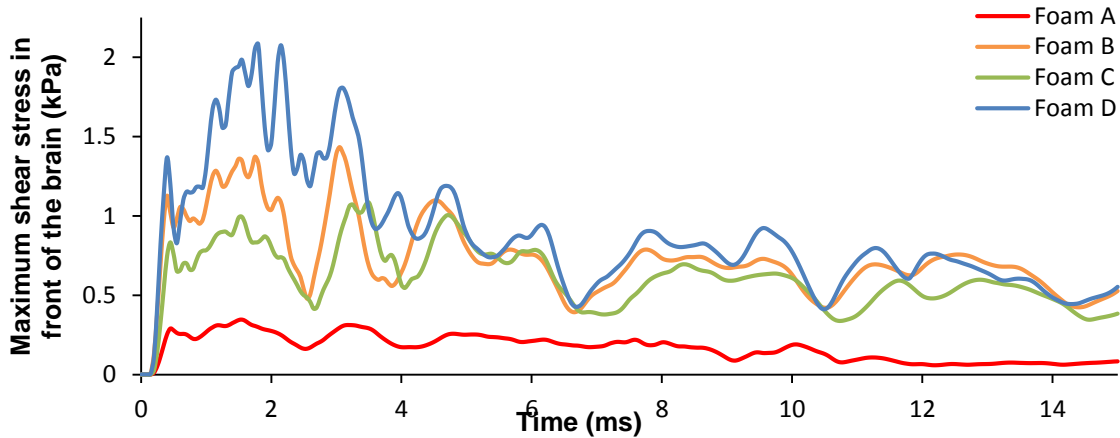
Figure 4-10. Maximum shear stress in a region in front of the brain with time for the four different types of helmet pads.

The variation of ICP on backside the brain with time was also recorded and illustrated in Figure 4-11. The ICP, in countercoup site, in case A, predictably, was the lowest compared to other cases. In considering the foams B and C, although, the density of foam B was less than foam C (50 versus 70 kg/m^3), foam C had a better response than foam B because of its mechanical behavior which was characterized by its stress-strain curve. Figure 4-12 showed the maximum shear stress in the selected region on backside of the brain. Foam A again had a better response and the best efficiency because of its lowest stiffness. The threshold for the brain injury

46

according to Anderson et al. [29] is 8-16 *kPa*. The shear stress created due to a bullet of velocity

360 *m/s* with the helmet and the current padding system was below such a threshold.
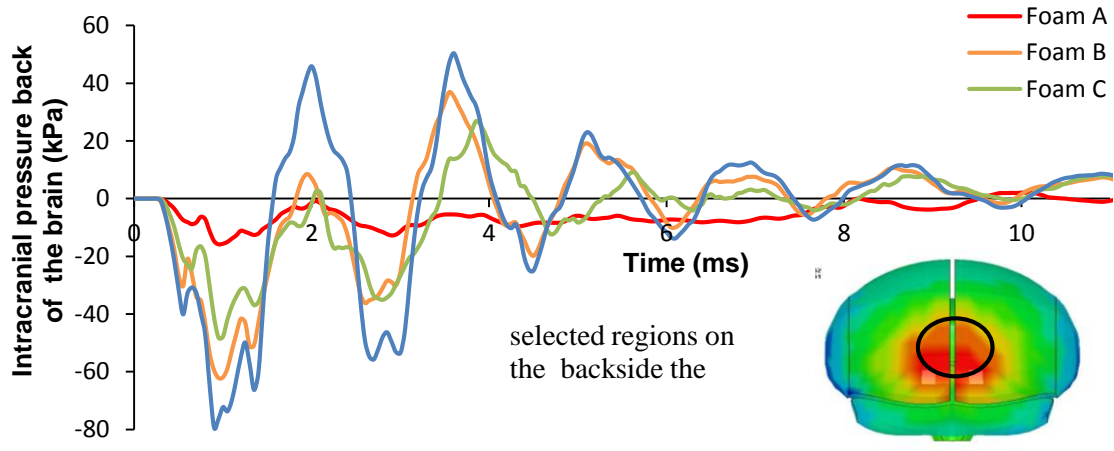
Figure 4-11. ICP on the selected region on the backside of the brain with time for the four different types of helmet pads.
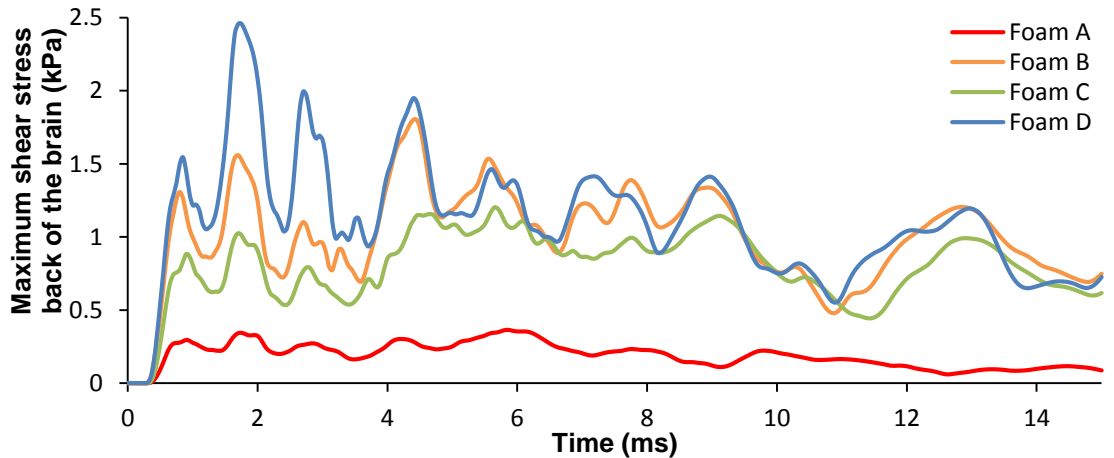
Figure 4-12. Maximum shear stress on the selected region on the backside of the brain with time for the four different types of helmet pads.

ICPs' contours at the time that the brain experienced the highest level of pressure in all cases were shown in Figure 4-13. As the results showed, the same areas of the brain tolerated the highest level of the pressure but at different values. Comparing Figure 4-7, Figure 4-9 and Figure 4-11, the maximum ICP and the center mass acceleration of the brain for various scenarios happened at almost the same time. Based on the data, foam A experienced the least acceleration

($24g$) and pressure ($21\ kPa$) at around 1 to 1.2 ms after the impact, while foam D experienced the highest levels of acceleration ($117g$) and pressure ($112\ kPa$) at about 0.9 to 1.2 ms.

Foam A	
21.7	
10	
5	
-6	
-18	

Foam B	
87	
51	
16	
-36	
-89	

Foam C	
61	
37	
2.7	
-20	
-55	

Foam D	
123	
56	
-22	
-92	
-115	
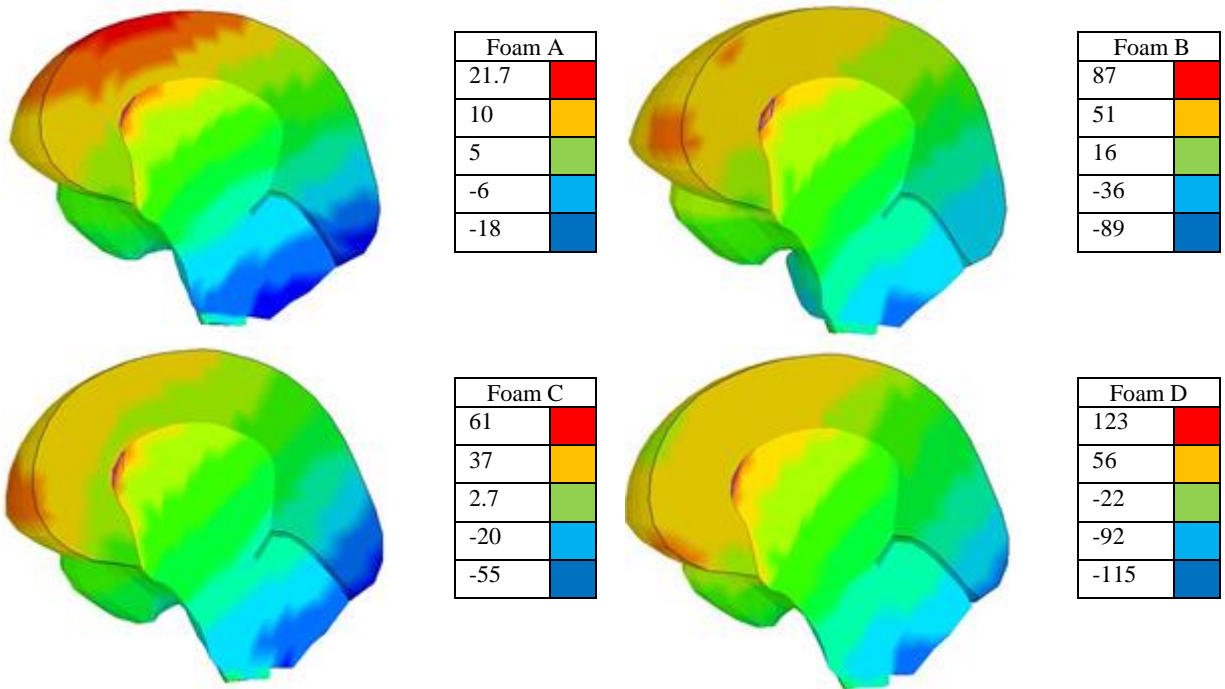
Figure 4-13. Highest level of ICP (kPa) using different foam materials.

4.2. The Analysis of Frontal Ballistic Impact

Since frontal impacts are more representative of real-life strikes in battlefields and, more importantly, the results demonstrate that this direction is utmost critical; all assumed scenarios of velocities (250, 350, 550 and 750 m/s) were considered for frontal impact to better understand the roles of materials of the padding system. Figure 4-14 showed the velocities of the helmet and brain explicitly at the different velocities of the striking bullets. As the speed of the bullets increased, higher kinetic energy was transferred to the helmet. In all examined scenarios; the helmet velocity was initiated at the instant of the strike to a sudden jump and decreased from its peak with time. The buildup of the brain velocity lagged the helmet velocity as the motion transferred from the helmet to the brain. Although the helmet and brain velocities were different, initially, they eventually became closer to one another. At a specific velocity higher than 550

48

m/s, the front pad experienced densification, becoming a rigid solid, and loosed its foam like characteristic due to the high momentum of the bullet impact. The foam material stress-strain behavior was at the tertiary region as explained in section 3.2 (Figure 4-3). Hence, at the striking speed of 750 *m/s*, the impacted load was too high for the frontal pad to be absorbed, a sudden increase in biomechanical response of the brain was observed and there was a complete separation of these data from the response of the brain at lower velocities. In fact, at this level of impact energy, most of the momentum was transferred to the head resulting in a rapid increase in the velocity of the brain.
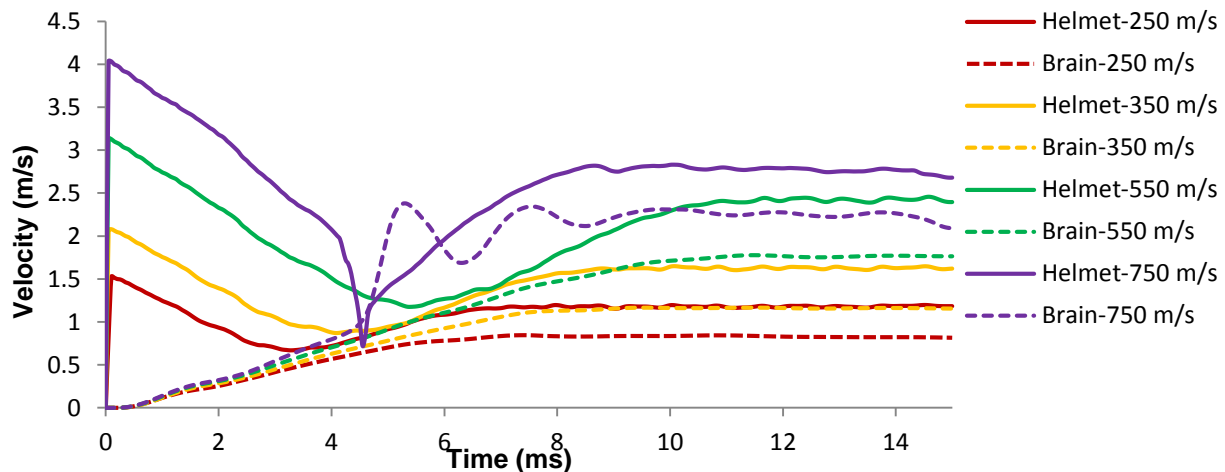
Figure 4-14. Helmet and brain velocity distribution with time after the bullet strike to the forehead of the model at different bullet striking velocities.

The volume changes of the frontal pad with time were demonstrated in Figure 4-15. It was due to the strike to the forehead with various impact velocities. Expectedly, the frontal pad absorbed most of the impact energy. As shown in this figure, the increase in the speed of the striking bullet caused higher reductions in its volume. As it typically expected from foam materials (as previously shown in Figure 4-3); as long as the pad experiences a strain level in the plateau region, its stress level remains almost constant. At the bullet's striking velocity of 750 *m/s*, the average volume reduction reached around 70%, explaining the complete densification of

the foam. After densification a sudden increase in the amount of transferred loading pressure and

stresses was realized in the skull and brain. Also a sudden increase in the center mass

acceleration of the brain was detected as shown in Figure 4-16. For a bullet velocity of up to 550

m/s, the change in the acceleration (44*g*) was tolerable compared to its equivalent value (280*g*)

when the bullet is 750 *m/s*.
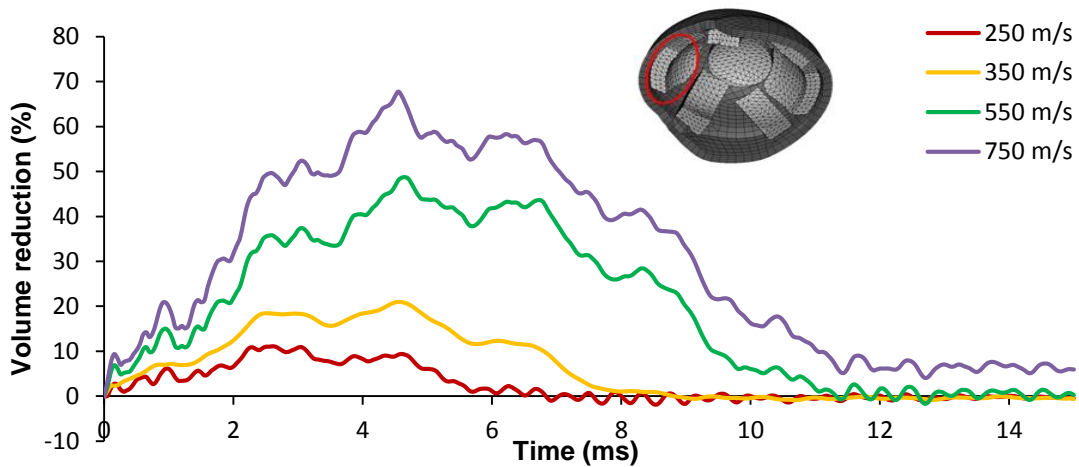
Figure 4-15. Percentage volume reduction of the frontal pad (shown by red circle) with time at different bullet striking velocities.
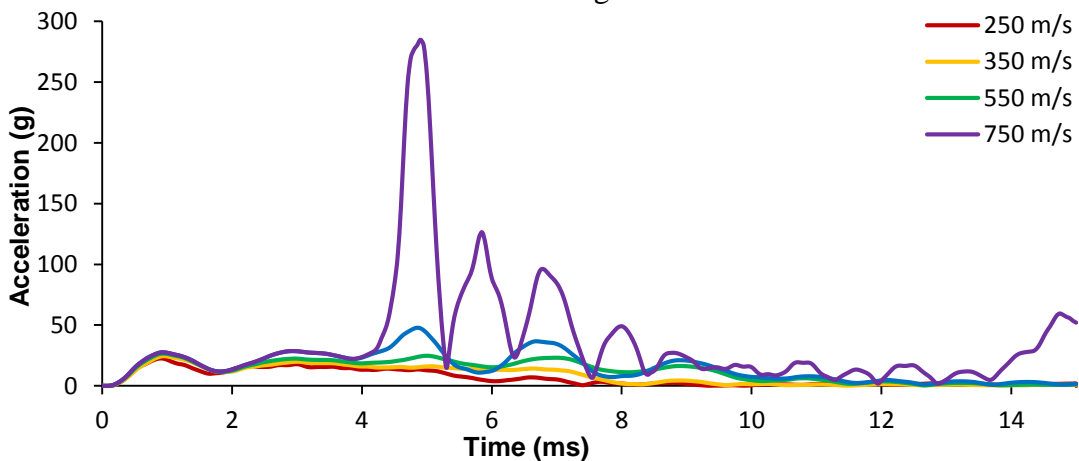
Figure 4-16. The acceleration of the center of mass for the brain, with time, at different bullet striking velocities (g=9.81 *m/s²*).

The built up pressure on the skull due to bullet strike with different velocities were

presented in Figure 4-17. The pressure for velocities up to 550 m/s increased modestly with an

increase in bullet velocity (up to about 0.7 *MPa*) and a sudden increase was realized for

velocities higher than 550 *m/s* (around 4 *MPa* when the bullet speed was 750 *m/s*). The duration

of the loading also increased, as the speed of the bullet increased till the threshold speed (550

m/s).
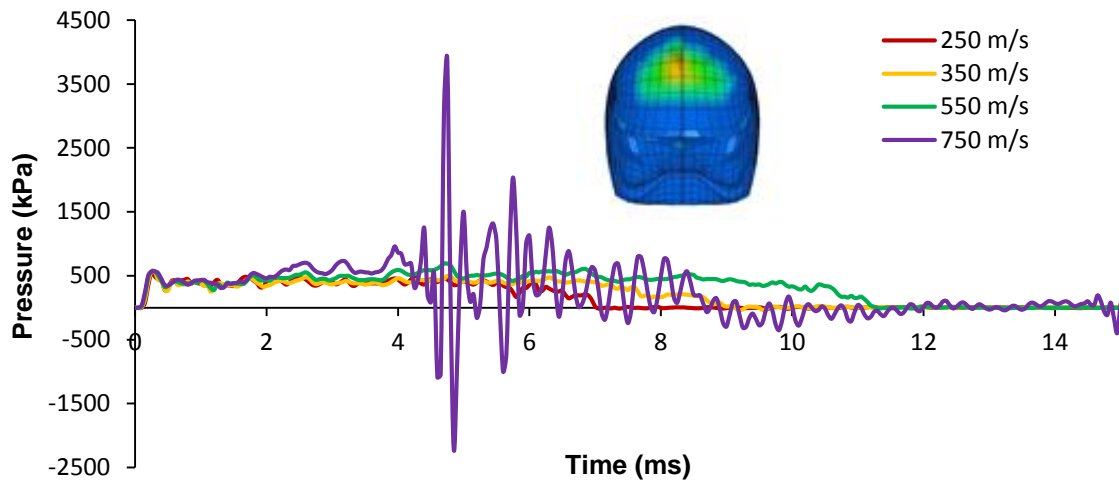
Figure 4-17. The pressure on a selected frontal area of the skull, with time, at different bullet striking velocities.

Variations of ICPs in the frontal region of the brain with respect to time were illustrated

in Figure 4-18. As expected, the variation of the ICP was positive as the brain moved inside the

skull. Again, the change in ICP was smoothed up to the speed of 550 *m/s*. At the 750 *m/s* bullet

striking velocity, the change in pressure was abrupt and regions of positive and negative were

created due to much higher momentum of the impact which caused the brain to move back and

forth, inside the skull, more frequently. This negative pressure can be considered as the source of

cavitation in the brain injury analysis.
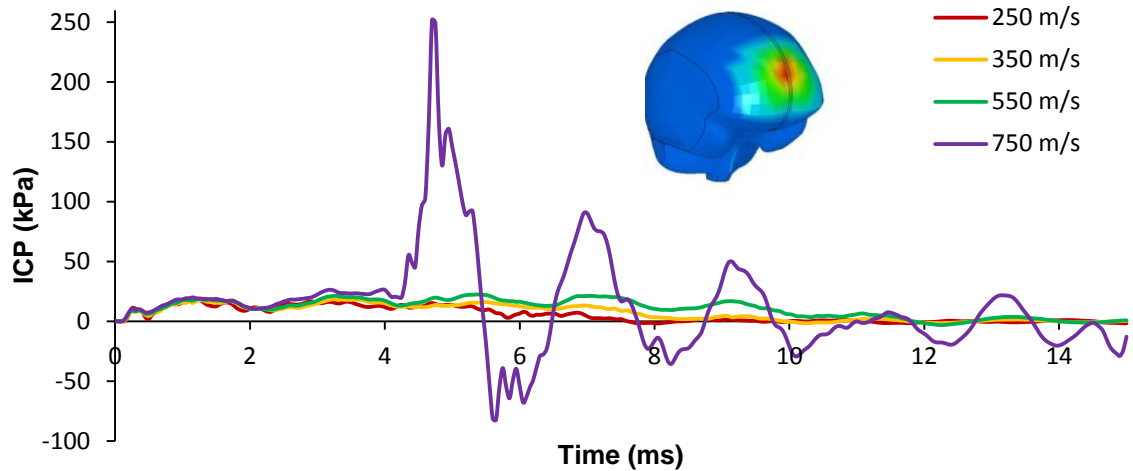
Figure 4-18. The ICP in the brain, with time, in a selected region, in front of the brain at different striking bullet velocities.

4.3. Ballistic Impact at Different Directions

The brain response depends on the direction of the striking bodies due to complicated geometry and variation of constituents of the head. For this reason, the human head model was subjected to strikes by bullets in the frontal (forehead), sagittal, and occipital positions. The ballistic impact positions deformation of the helmet and bullet after the impact were illustrated in Figure 4-19. The bullet was assumed to have a mass of 8 *gr* and stroke the head in a perpendicular direction. The biomechanical data of the head and brain was measured and monitored for each incident for the bullet's initial velocity of 550 *m/s*. The results were compared regarding various ballistic impact positions.
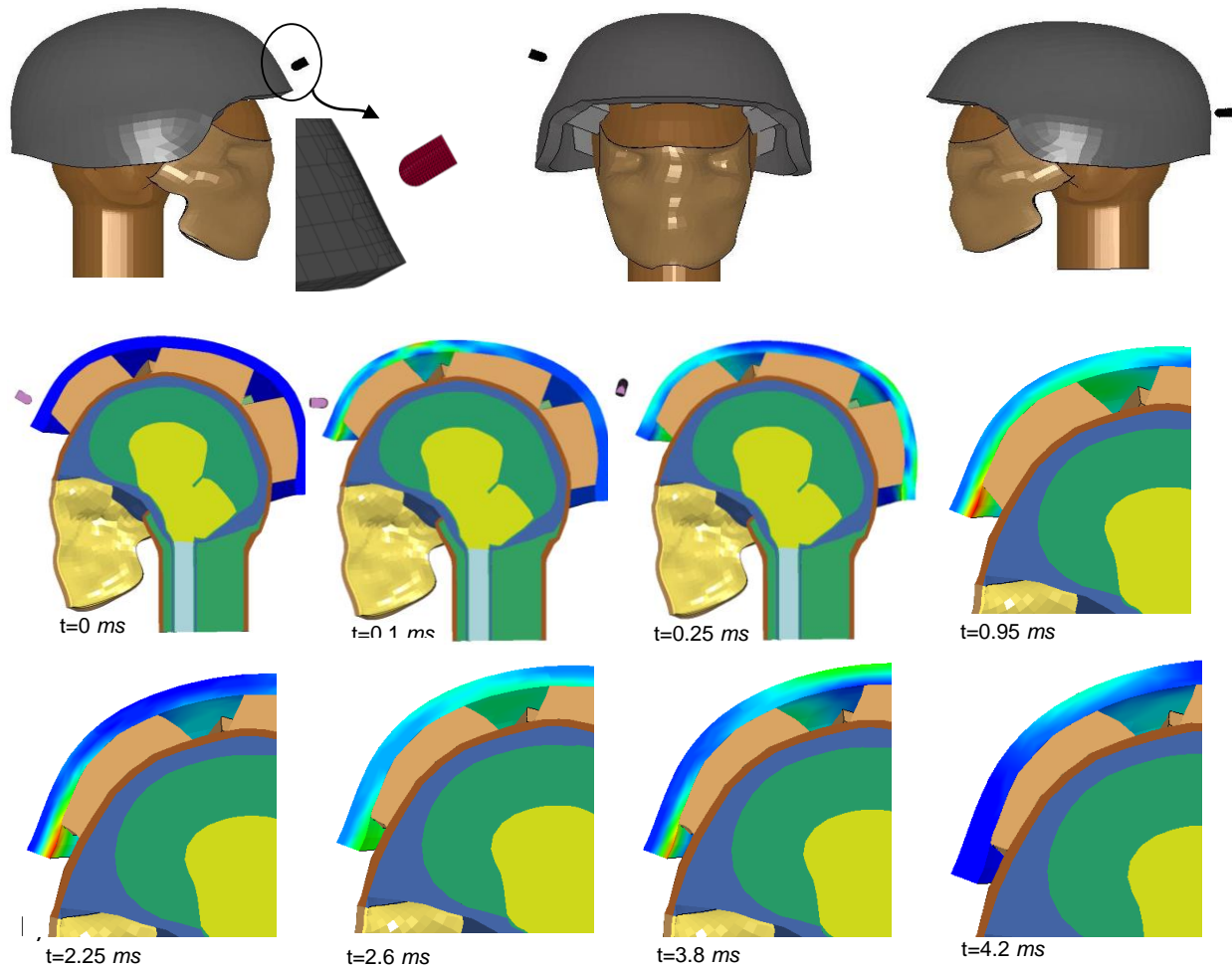
Figure 4-19. The ballistic bullets strike the head model in the frontal, sagittal and occipital planes, and image sequence showing the bullet and impacted area in front of the helmet at different times at the speed of 550 *m/s*.

The results obtained from striking at velocity of 550 *m/s* were considered and compared for the three positions of the strike for the purposes of brevity. In Figure 4-20, the kinematical motion of the helmet and the brain, in terms of their velocity size, were compared for the all three incidents. As shown in this figure, the helmet moved initially at a sudden speed due to the strike in the sagittal plane and the speed starts to decay with time. The brain, on the other hand moved initially at zero speed, due to presence of padding system that absorbed impact energy, and the speed increased gradually until the brain and the helmet velocity became identical.
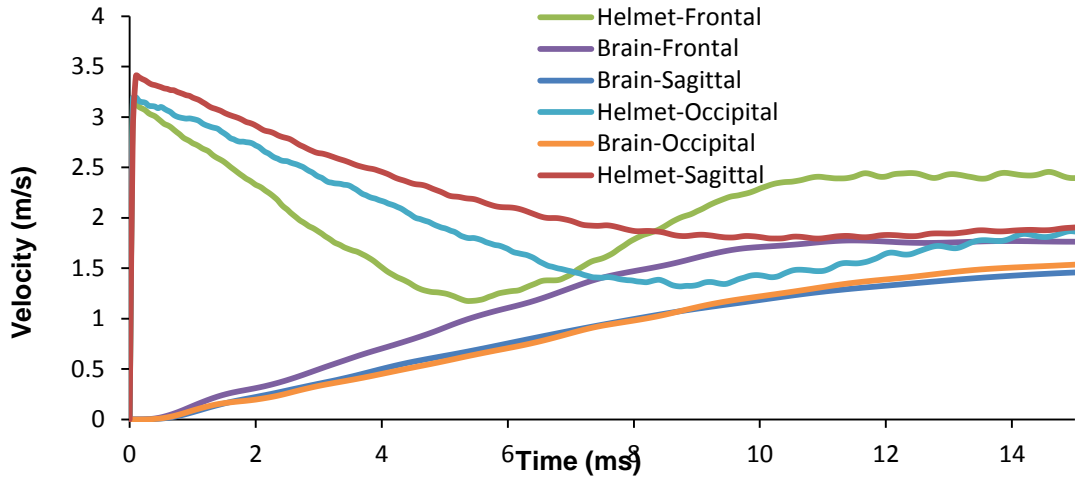
Figure 4-20. Helmet and brain velocities after the strike at different impact positions at the speed of 550 *m/s*.

The changes in accelerations of the center of mass of the brain were compared for the three incidents of the strike (Figure 4-21). Maximum experienced accelerations by the brain were around 26*g*, 18*g*, and 19.5*g* in frontal, sagittal, and occipital impact positions, respectively. Similar to the changes occurred in the brain velocity due to the frontal impact, the center mass acceleration was higher than it was for the other two cases. Therefore, it concluded that the frontal strike created the harshest situation.
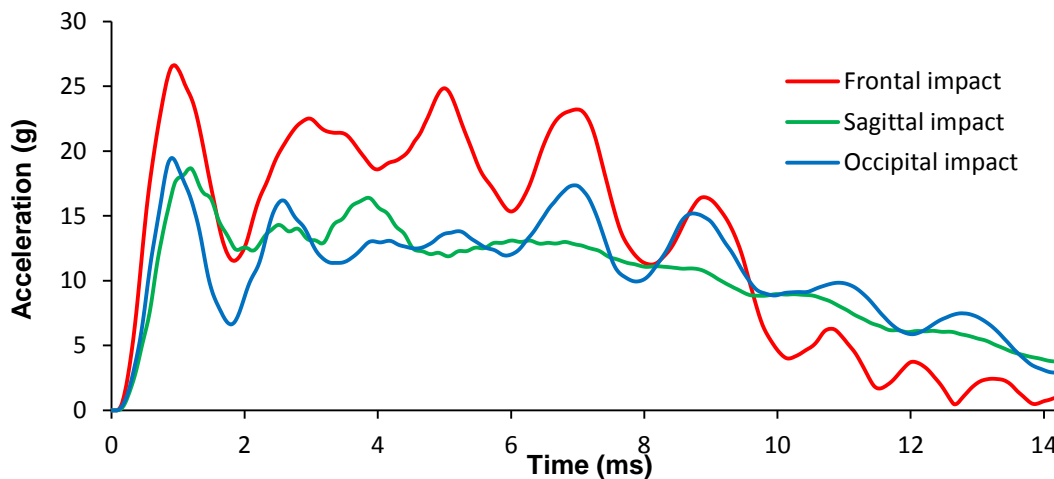
Figure 4-21. Center of mass acceleration of the brain for the three different impact positions at the speed of 550 *m/s*.

54

The average ICP in the coup sites of the brain, for each case of strike, was also plotted and compared in Figure 4-22. The variation of the ICP agreed with the center of mass acceleration and the velocity changes as shown in Figure 4-20 and Figure 4-21. The pressure remained on the brain for about 10ms and then vanishes. Several fluctuations could be observed for the case of frontal strike which have not been seen in the results obtained for two other impact positions.
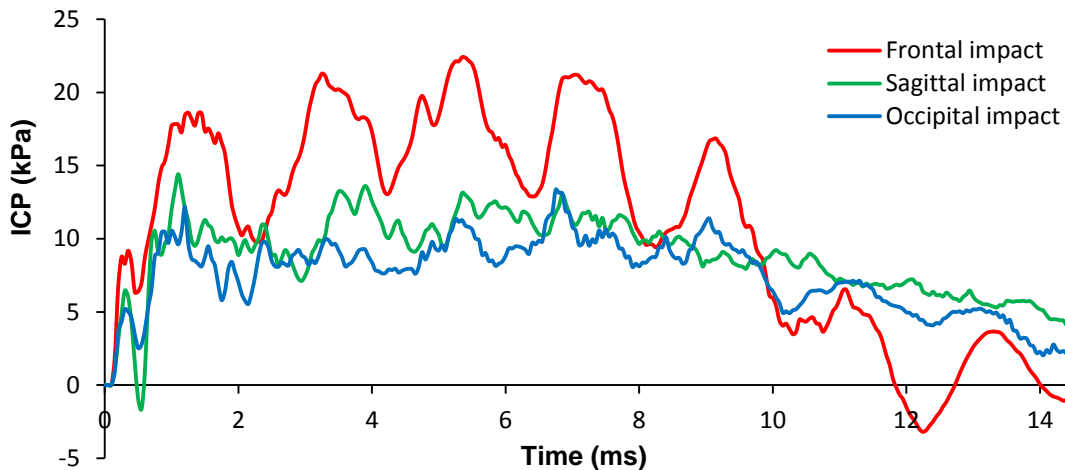
Figure 4-22. The intracranial pressure due to bullet strike in three different cope regions of the brain corresponding to the strike positions at the speed of 550 *m/s*.

To better understand the application of the padding system and to explain how they react upon a sudden impact, the changes in the thickness, with time, of the corresponding pad, close to the strike positions were shown in Figure 4-23 for all three scenarios. As illustrated, the pads suffered a negative thickness change due to the impact load. The thickness decreased with time initially and returned almost to its original value once the pressure wave passed through and moved to the skull and brain from the helmet shell.
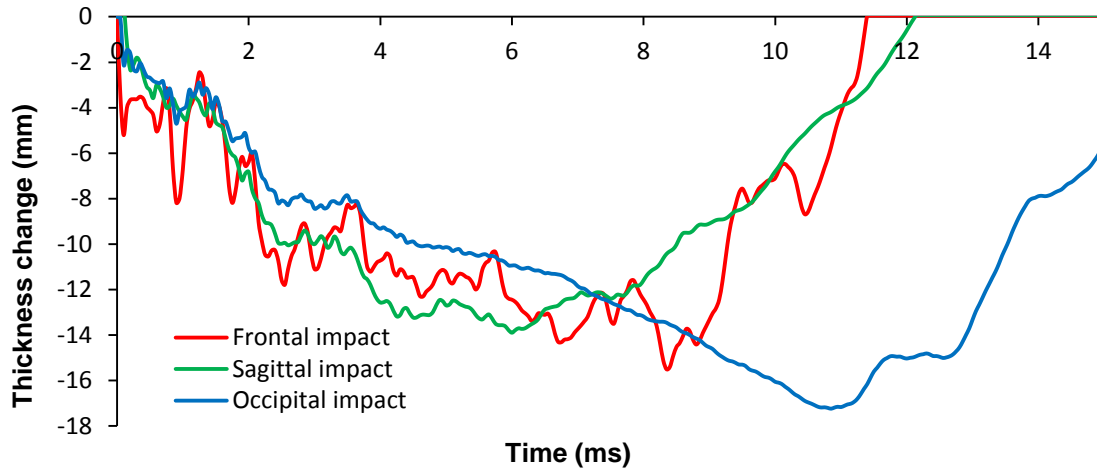
Figure 4-23. The thickness change of the corresponding pad close to the striking position in various scenarios at the speed of 550 *m/s*.

Distribution of ICP at 0.15, 0.3, 3, 6, 10.2, and 14.2 *ms* after bullet stroke to the forehead of the model were presented in Figure 4-24. Initially, a high pressure area was created in the forehead while a region of positive pressure was developed on the backside of the head (the coup and contrecoup processes in the brain). This distribution changed very quickly through the brain at short intervals (Figure 4-24). The size of ICP was decreased with time quickly after the effect of the strike was disappeared. This figure clearly demonstrated how the pressure waves spread through and inside the brain after the impact.
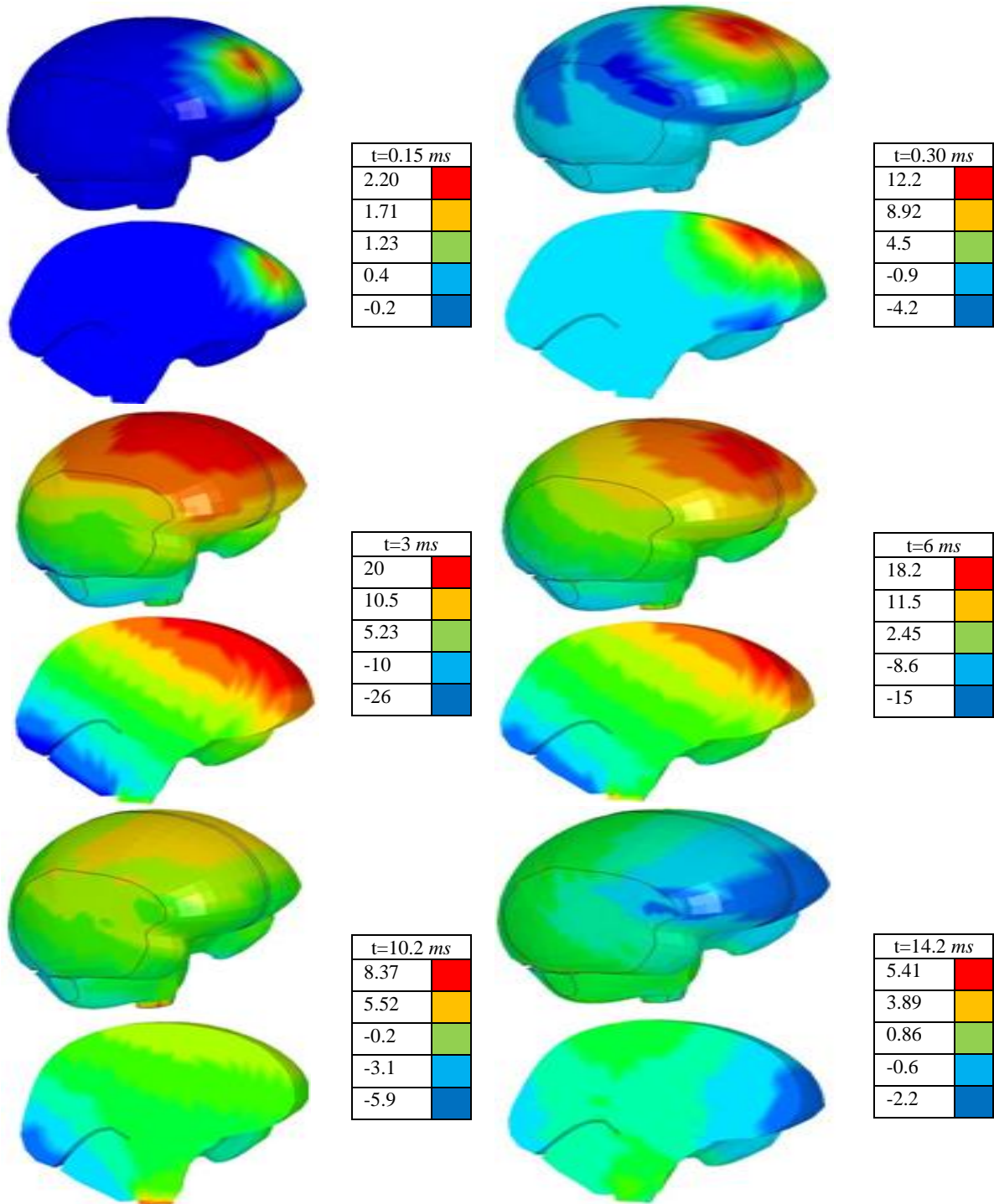
Figure 4-24. The contours of ICP (*kPa*) at different times after the bullet struck the forehead at the speed of 550 *m/s*.

Contours of ICP waves in the brain respect to time, when the bullet stroke the head in the directions of sagittal and occipital planes were illustrated in Figure 4.25 and Figure 4-26. The coup and contrecoup phenomena were visible on the brain the instant the bullet strikes.
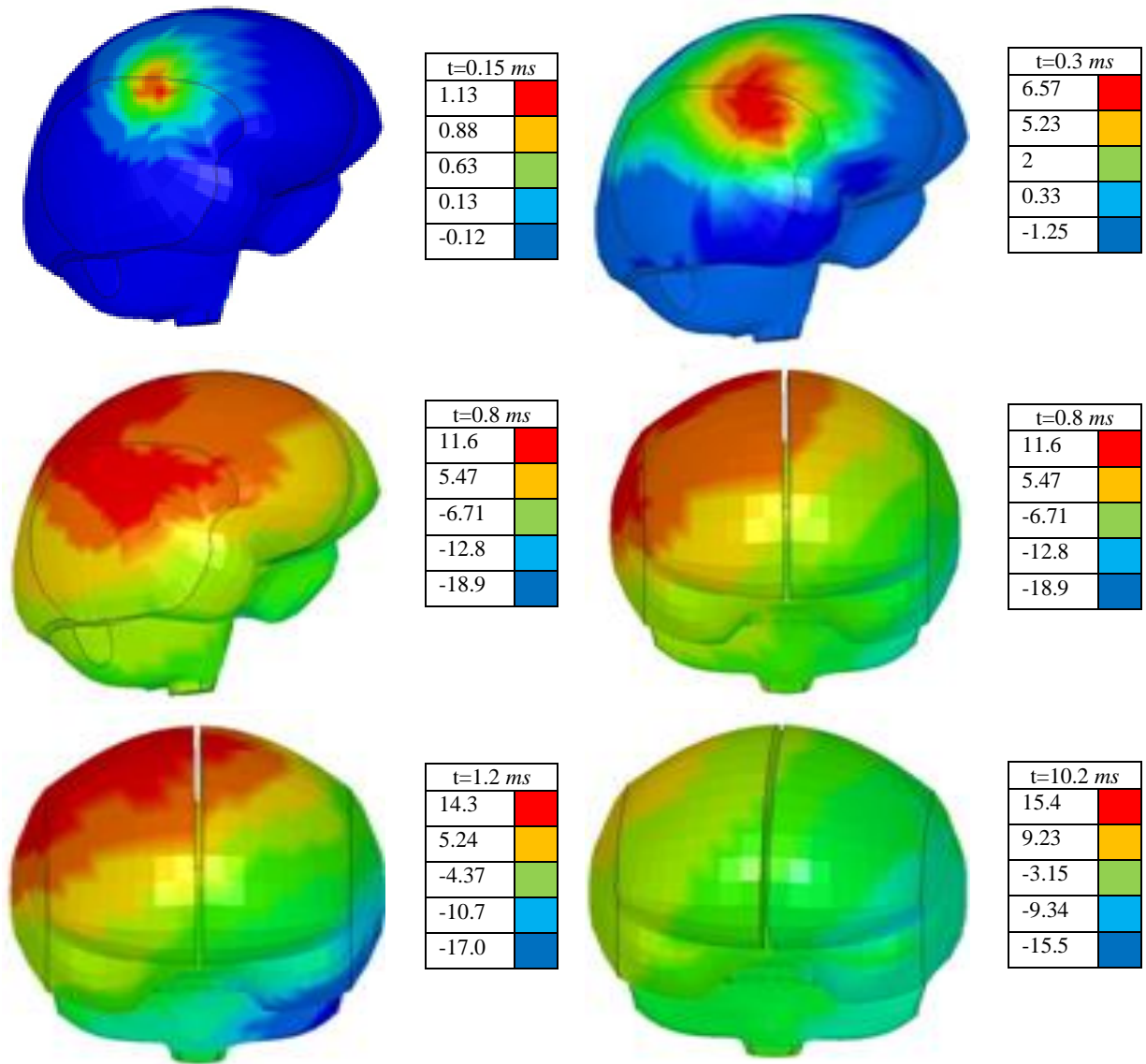
Figure 4-25. The contours of ICP (*kPa*) at different times after the bullet strikes the head in the sagittal plane at the speed of 550 *m/s*.
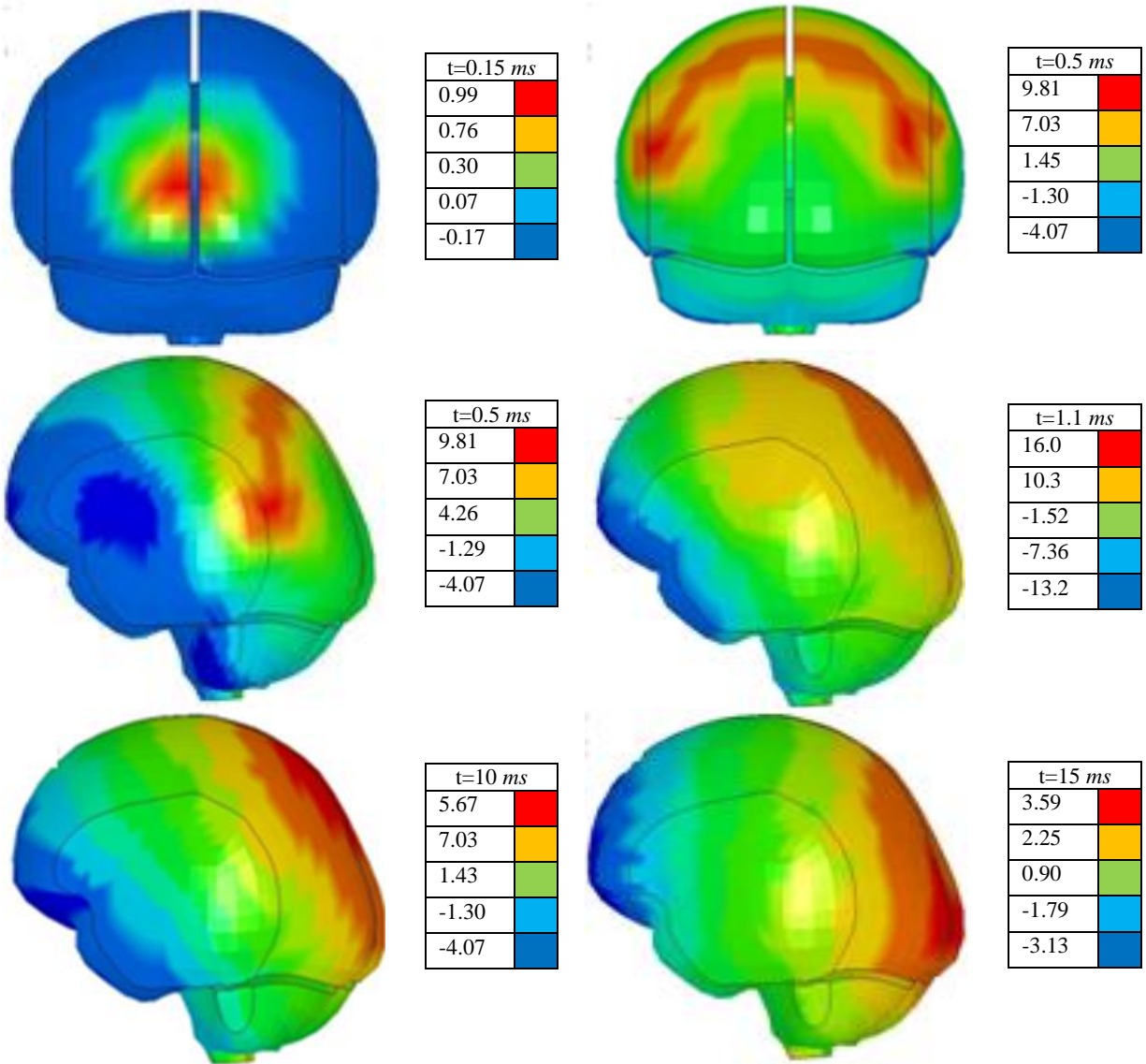
Figure 4-26. The contours of ICP (*kPa*) at different times after the bullet struck the back of the head in occipital plane at the speed of 550 *m/s*.

To understand how the pressure on the brain changed with time, the maximum levels of ICPs at different time span were recorded for each case. Recorded data indicated that in the frontal impact the brain experienced the highest level in the coup site (Figure 4-27).
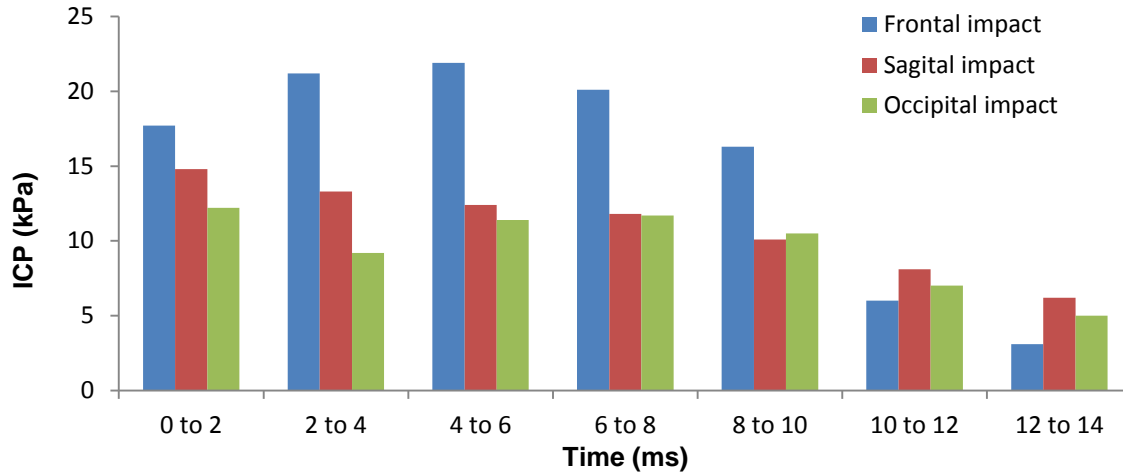
Figure 4-27. Maximum level of the ICPs at different times in the coup site.

4.3. Ballistic Impact at Different Angles

The angle of impact of the bullet with the helmet has an influence on the amount of the transferred momentum, and the resilience efficiency of the helmet and padding system material. Using the pads with the least stiff material (Foam A), the helmeted-head model was exposed to three ballistic impacts from three different directions or angles in sagittal plane (as shown in Figure 4-28), one in horizontal direction, one perpendicular to the helmet shell, and one at 60˚ from the horizontal direction.
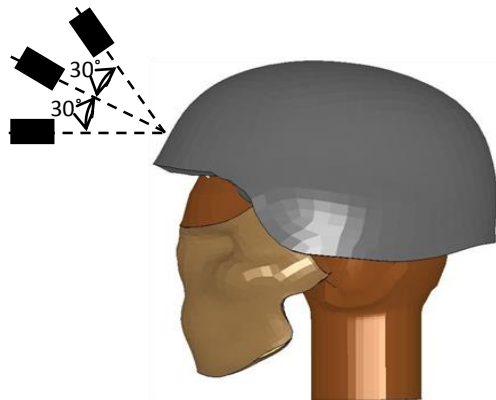
Figure 4-28. Various angles of bullet impacting the forefront of helmeted head model.

The variation of the ICP in the coup site corresponding to the impact area and the variation of the maximum shear stress in the brainstem were presented in Figure 4-29. As shown,

60

the coup site ICP was smaller for the case that the bullet stroke the helmet in horizontal direction

(i.e. at 0o angle) than the other two cases. When the bullet run perpendicular into the helmet shell

(i.e. at 30o angle), the transferred load and also the contact time duration were maximum and the

highest amount of linear momentum were transferred to the helmet. Therefore the highest ICP

are expected for this angle. Variation of shear stress in brainstem which was the area that

experienced the maximum shear deformation was plotted in Figure 4-29 (B). Similar explanation

as ICP could be discussed on the amount of shear stress in the brainstem.
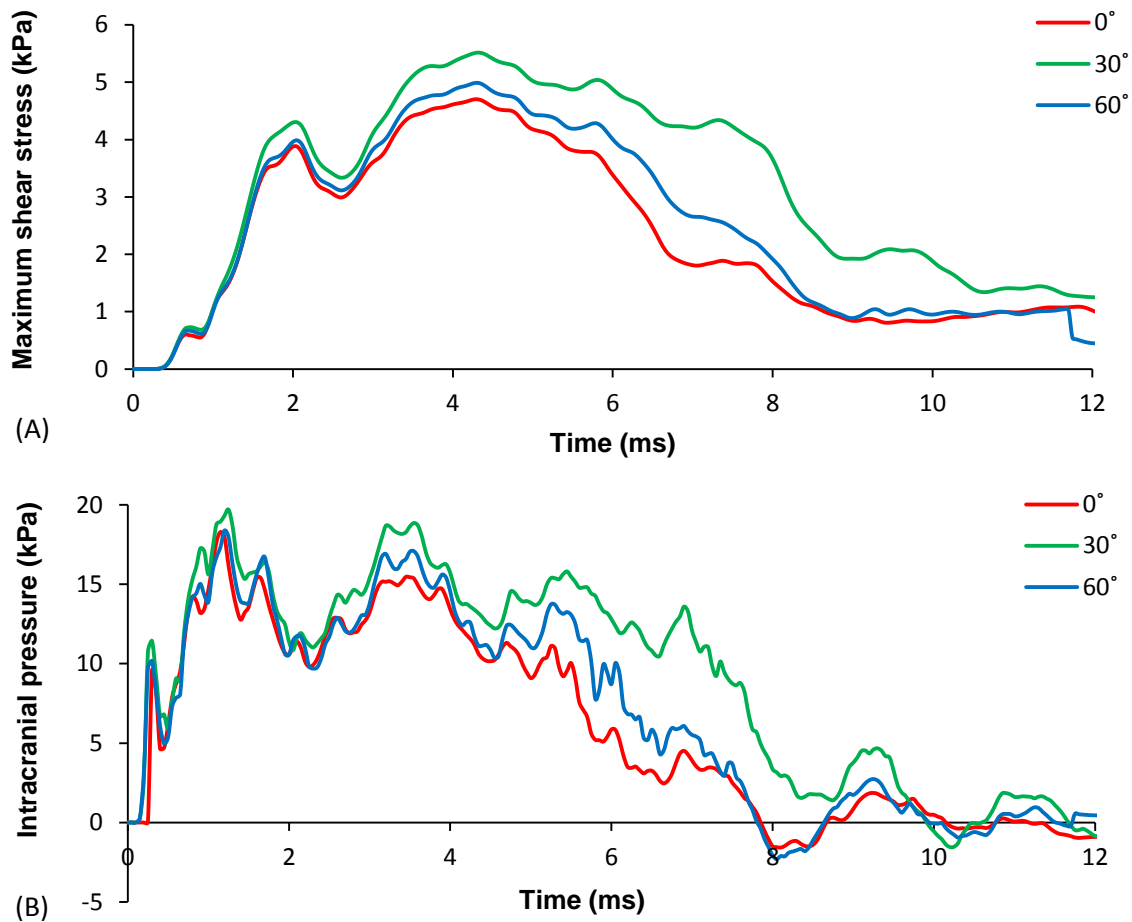
Figure 4-29. (A) ICP in the coup site region, and (B) maximum shear stress in the brainstem region change with time due to the bullet strike in the localized region on the front of the brain for three different angles of impact.

4.4. Conclusions

In this part of the research, a simulation of a helmeted human head was presented under a striking bullet ballistic impact. The strikes created pressure and motion in the helmet, skull and brain. The focus of the research was to study the influence of the padding material of the helmet on the transformed load to the brain. Four different types of foams, with different stiffness and density were modeled. Acceleration, ICP in coup and countercoup sites, and maximum shear stress in the front and backside of the brain were computed and compared. It was concluded that stress-strain curve of foam, representing mechanical behavior of the foam, played an indispensable role in transferring the load to the head; the less the stiffness of the foam, the less the level of the load on the head. In addition, with all of the foams, the brain tolerated the maximum ICP when it reached the maximum acceleration. As far as the angle of striking impact is concerned, when the bullet hits the helmet perpendicular in the forefront, the brain experienced the maximum amount of ICP and shear stress. The position of the ballistic impact strike was studied as an important parameter due to the geometry of the head, brain and helmet. The forefront impact was the most severe situation due to the minimum contact area of the pad and the helmet. The conclusions here apply to this special type of loading, and they are correct as long as the foams do not pass their plateau region of stress-strain curve. The impacts of the velocity of the strike (from 250 to 750 *m/s*) as well as the position of the strike (frontal, sagittal and occipital positions) were examined. The motion and the pressure stress in the helmet, skull, and brain were calculated. The size of these parameters was compared for the range of bullet velocity. The results show that as long as the foam behaves in its plateau region, the maximum transferred load to the head does not increase even when the bullet struck the helmet at a higher bullet speed (up to 550 m/s for this specific case study). For the helmeted human head model

under consideration, it was realized that in an attack, and at speeds higher than 550 m/s, the frontal pad of the helmet is densified and the momentum of the striking bullet is transferred rigidly to the skull and brain. This causes sudden changes in the biomechanical data of the brain. Thus, the constitutive behavior of the pad plays an indispensable role in transferring the load to the head. While the pad materials, under an impact load, reaches to its third (densification) region, the situation seems to be that there is no pad between the shell and head, transferring a greater amount of loads to the brain. The position of the strike also affects the level of transferred load to the head. Because the geometry of the head, helmet, as well as the effective contact area of the pads with the helmet and head, are different and make the situation complicated.

5. BIOMECHANICAL PARAMETERS OF THE BRAIN UNDER BLAST LOADS

Exposure to the high velocity impact resulted from blast is another cause of TBI.

Recently, using high strength explosive materials have dramatically increased the number of

blast Traumatic Brain Injuries (bTBI) among military service members and civilians. The

mechanism of TBI is more complex when the head is exposed to high velocity impact loads such

as blast waves [101]. In ballistic impacts TBI is because of the head acceleration and

deceleration and the relative movements of the brain inside the skull [102]. In the blast scenarios

the head reactions not only involve sudden acceleration or deceleration but also local skull

flexure and volume changes of the intracranial contents are happened and TBI is resulted.

Information about the mechanisms of blast waves and their interactions with head can certainly

help in the development of materials and design of the helmets and padding systems to decrease

the level of the brain injury due to the blast loads. Various parameters such as standoff distance

from the detonation, blast wave peak overpressure, and positive overpressure duration affect the

level of primary blast injury.

In general, injuries resulting from the blast waves are classified into four groups:

primary, secondary, tertiary, and quaternary. Primary or pure blast injury results from direct

exposure to the blast waves. Secondary blast injury happens when the head is hit by other objects

that have been given motion by the blast. People striking a solid object may experience tertiary

blast injury due to motion caused by the blast wind. Quaternary blast injury comes from toxic

gases produced during the explosions [102-106]. The role of pure blast exposure in TBI

development is not, however, completely clear. Primary blast may cause linear and rotational

accelerations, but the quick blast overpressure, transferred to the brain via the skull, causes

complex stress wave motions. Indeed, when the blast waves impact the head, part of the waves

are reflected and part of them can pass through the skull to the brain. Consequently, stress waves are generated which can damage the brain tissues. Primary blast injuries resulting from blast waves can be better diagnosed based on the level of inflicted stresses on the brain [62, 103].

Ballistic helmets are highly recommended to reduce the severity of brain injuries in combat zone. The main purpose for wearing a helmet is to protect the head against flying objects and ballistic impacts. Helmets, however, are not tested under blast loading conditions [101, 107, 108] and there is no available standard that govern the use of helmet for this purpose. In fact, the efficiency of helmets against the blast loadings is not explicitly clear. In the case of protected head, only a few researchers have studied the efficiency of the helmet under the blast loadings. Some have concluded that helmets can even amplify local overpressure which is known as underwash phenomena, particularly when considering the hard shell alone in the absence of padding system [106, 109-111]; some other researchers have shown that a helmet and suitable padding system can reduce severity of bTBIs [112]. Orientation of the head with respect to the blast wave propagation and environmental factors may also impact the level of the stresses on the brain. Level of damage due to the blast waves also depends on the loading conditions and the ability of the target to resist against the blast waves, which depend on mechanical properties and boundary conditions (fixation of the head model in this study).

Numerical models are certainly an excellent tool for determination of the mechanical response of the head to the different intensity of blast loads. There have been some efforts to simulate the explosion situations related to bTBIs. Chafi et al. [68] simulated the blast propagation by using an Arbitrary Lagrangian-Eulerian (ALE) multi-material FE modeling procedure. They examined ICP on the brain, the maximum principal strain, and maximum shear stress to predict the level of the brain injury. Taylor and Ford [62] examined the exposure of the

head to an overpressure explosive blast of 1.3 *MPa* to study TBIs. They also measured the ICP, shear stress, and the volumetric tension in anterior, posterior, and lateral directions of the brain and concluded that the stress localization, due to early-time intracranial wave, can cause axonal injury.

In this part of the research, an open air blast scenario was simulated in LS-Dyna FE software package by using the coupling method of an empirical explosive blast shock generation in conjunction with the multi-material ALE formulation. The Lagrangian head-neck model was immersed into the Eulerian domain to measure the kinematical and mechanical responses of the head and brain under the blast scenarios. The efficiency of the helmet and padding materials were examined under the blast load of 200 *gr* with the standoff position of one meter from the top of the head. The level of transferred load to the head in terms of different biomechanical parameters was determined for the unprotected and protected head models.To study the effect of the helmet on the response of the head in various blast orientations, three different positions of the explosive material were simulated; front of the head, above the head, and in back side of the head.

To date, the majority of available studies have ignored to include the body in the brain injury modeling analysis, since the blast waves can pass through the head very quickly in a matter of a few milliseconds. Therefore the free-floating head FE models have been considered mainly to reduce the time and cost of the simulations [40, 68, 113-115]. To only cite an instance, Gu et al. [115] used the free boundary condition for their head model since they assumed that the effect of stress wave is significantly more that the effect of the head motion. Some researchers, on the other hand, have simply fixed the base of the FE head model to study the biomechanical responses of the head under the blast loads [62, 105]. For instance, Ganpule et al. [105] fixed the

bottom of the neck in all six degrees of freedom to avoid rigid body motion. While including the entire body is analysis is computationally expensive, neglecting the effect of the body under all circumstances is questionable. Last part of this chapter was carried out to numerically examine the effect of the body on the biomechanical responses of the head under the free space blast situation.

In this chapter, scalp was considered as a linear elastic material. Linear elastic behavior has also been used for the skull and membrane components; the dura mater, tentorium, and falx. FE and mechanical properties of the parts of the head with linear elastic behavior assumption were listed in Table 2.2. One layer of a solid element with elastic behavior was used to model the CSF. Table 2.3 presented the element type and material properties of the CSF used in this simulation. Since, under the high level of the impact loads as it happens during the blast condition, biological tissues experience complex viscoelastic behavior as well as large deformations, brain tissue becomes a non-linear material with shear strains more than 1%, linear constitutive equations is inaccurate. The mechanical properties of the brain were assumed as homogenous and isotropic viscoelastic with the Mooney–Rivlin hyper-elastic type material model. Material properties of the brain adapted from Mendis et al. [69] were presented in Table 2.5.

5.1. Physics of the Blast Wave

If an explosion occurs in an open air condition, a spherical shock wave is created moving away from the detonation center while losing its velocity. The pressure in front of the shock is known as the peak incident pressure. Blast wind is formed by reduction in the air pressure when the shock front passes through the air and air particles following the shock front with lower

velocity. Expanding the blast waves increases the volume of pressurized air and based on thermodynamic laws, the shock front pressure must, therefore, be decreased.

A typical change of pressure with time at a point in the vicinity of a blast is shown in Figure 5-1. p_0 represents the atmospheric pressure; p_{max} is the maximum over pressure which depends on the distance of the point from the explosion site and mass of the detonation and slightly the shape of the detonation; t_a is the arrival time of the frontal shock wave; and t_d is the positive duration time of the blast wave which is the time for backing to the ambient pressure. After this time, the pressure drops below the reference pressure and reaches the maximum negative pressure p_{min}. The duration of the negative phase is indicated as t_n. The overpressure impulse is the integral of the overpressure curve over the positive phase t_d.
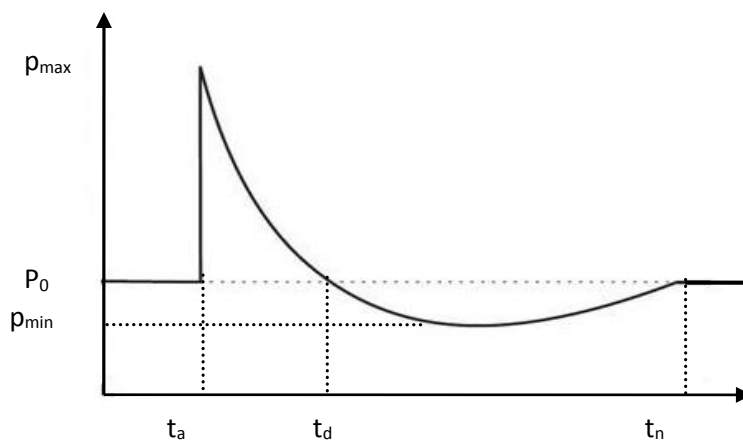
Figure 5-1. Typical variation of the pressure wit time at a point in the vicinity of the explosion due to the blast (p_0: normal pressure, p_{max}: the maximum over pressure, ta: arrival time, t_d: positive duration and t_n: duration of the negative phase).

Several empirical equations have been suggested to mathematically measure the pressure–time history of an air blast and they are in good agreement with experiments. Friedlander considered the air to be an ideal gas and characterized the waveform to show the pressure–time history of an open-air blast [116]. The Friedlander waveform equation is as follows [117]:

$$p(t) = p_0 + p_{max}\left(1 - \frac{t}{t_d}\right)e^{-\frac{bt}{t_d}}$$

(5-1)

In this equation b is decay constant and other parameters are described in Figure 5.1. All

parameters for the pressure-time curve can be taken from different diagrams and equations.

Kingery and Bulmash [118] employed lots of experimental data to develop diagrams and to

evaluate the air blast parameters. The parameters are presented in logarithmic scales diagrams, or

in a form of polynomial equations. These diagrams and equations are widely used by researchers

and are applied in different computer programs to calculate the air blast wave values [119].

5.2. Blast Wave Modeling

FE simulation of blast situations is a widely accepted method for studying the response of

the structures. In simulating the blast loads in LS-Dyna, three different methods are considered

that were briefly explained in the followings (LS-Dyna Theory Manual, 2007 [64]).

5.2.1. Purely Lagrangian method

In this method; the mass of the explosive material is specified as well as its position

relative to the structure. The blast pressure on the structure is calculated by empirical equations;

CONWEP blast loads algorithm. This method does not consider the blast wave propagations and

their reflections because no propagation medium is considered.

5.2.2. Multi material ALE formulation method

This method is based on explicit modeling of the air and detonation with multi-material

ALE formulation to simulate the blast wave propagation. The model in this method includes both

detonation and air as the medium. The pressure due to the explosion is calculated using Jones-

Wilkins-Lee (JWL) equation.

$$P = A\left(1 - \frac{\omega}{R_1 V}\right)\exp\left(-R_1 V\right) + B\left(1 - \frac{\omega}{R_2 V}\right)\exp\left(-R_2 V\right) + \frac{\omega}{V}E$$

(5-2)

Equation (5-2) relates the pressure to the relative volume, *V*, and initial energy per initial volume, *E*, known as equation of state (EOS). In this equation *A*, *B*, R_1, and R_2 are constant parameters. A linear polynomial EOS is also needed for the air (medium) to relate the pressure, temperature, and specific volume of the air.

$$P = C_0 + C_1\mu + C_2\mu^2 + C_3\mu^3 + \left(C_4 + C_5\mu + C_6\mu^2\right)E \tag{5-3}$$

Where C_i is constant, $\mu = \dfrac{1}{V} - 1$ and *V* is the relative volume. For an ideal gas all these constants coefficients are zero, except C_4 and C_5.

A continuous and uniform front shock wave can be captured in this method if fine elements were used for discretization of both detonation and ALE. Solving Eulerian equations (Navier-Stokes equations) is computationally expensive, especially in the case of a long standoff distance that requires a large number of elements between detonation and the structure. This is the main disadvantage of the second method.

5.2.3. Coupling method

This method as a combination of the two previous methods is more advantageous compared to the others. In this method, the wave propagations and blast reflections is simulated only in the vicinity of the structure. To model the blast wave propagation in the media around the head, the positive phase of the blast load is calculated at the ambient layer (Figure 5-2). The pressure on the ambient layer is measured similar to the first method using empirical equations. The loading is then enforced into the ALE medium. Inside the air ALE domain, the formulations in the second method are employed to calculate the pressure wave variations to model the blast wave propagation. The same EOS equation (5-3) for the air is used as ideal gas ($C_4=C_5=0.4$ and $E=0.25$ *MPa*) in the second method. Compared with the second method, a main advantage of this

method is to remove the detonation which means JWL equation is not solved to model the behavior of the explosion. Additionally, a large number of elements can be eliminated from the domain. Selection of finer elements increases the uniformity of the elements around the head which leads to more accuracy and less computational cost.
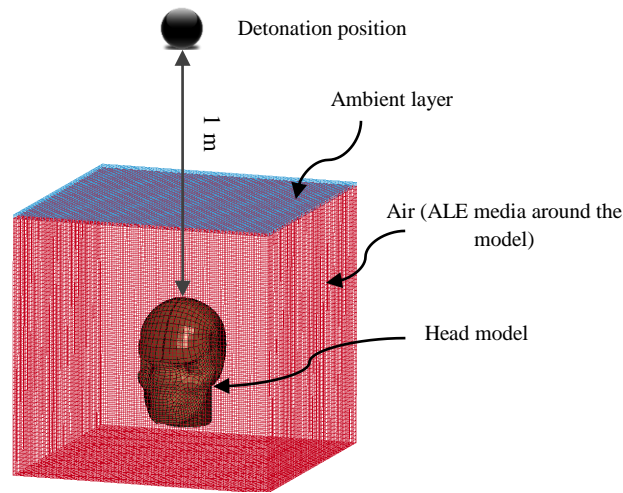
Figure 5-2. The blast, the exposing head and the spacing: 50×50×50 *cm³* ALE media around the head is discretized by finite elements.

5.3. Verify the Blast Wave Simulation

The blast waveform propagation in the air using coupled method (used in this work) was verified against an experimental result and MM-ALE numerical method. The result showed a very close agreement with the experimental data while the MM-ALE deviated from the actual waveform in the positive phase (Figure 5-3). In fact, since the Eulerian domain around the head discretized by using finer mesh size the results are in accurate in this simulation compared to the one from MM-ALE method.
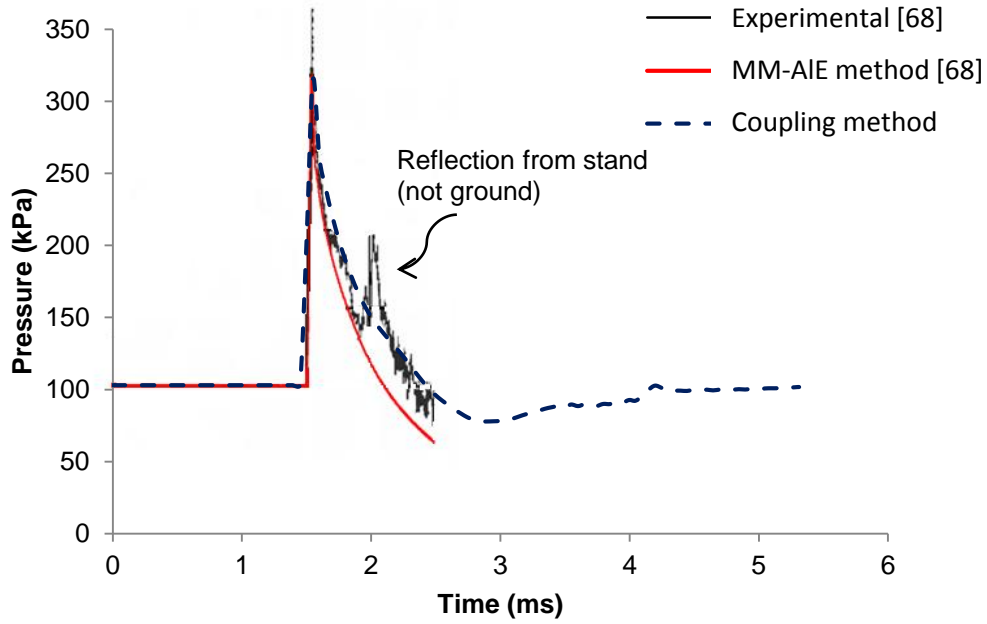
Figure 5-3. Variation of the pressure in the media with time in two different blast load simulation methods and experimental data.

Moreover, Figures 5.4 and 5.5 presented the results of modeling an elastic plate ($30\times30\times1$ (cm^3)) that was exposed to 200 gr of standard TNT by one meter standoff distance using the purely Lagrangian method and the coupling method. Center mass velocity and acceleration of the plate have been recorded and compared.
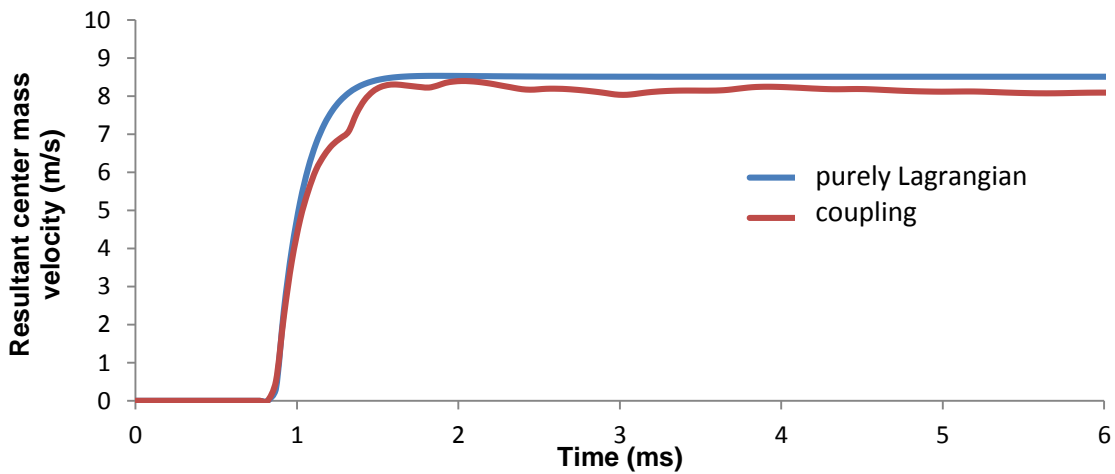
Figure 5-4. Variation of the resultant center mass velocity of the free solid structure under the same blast scenario modeled with two different methods.
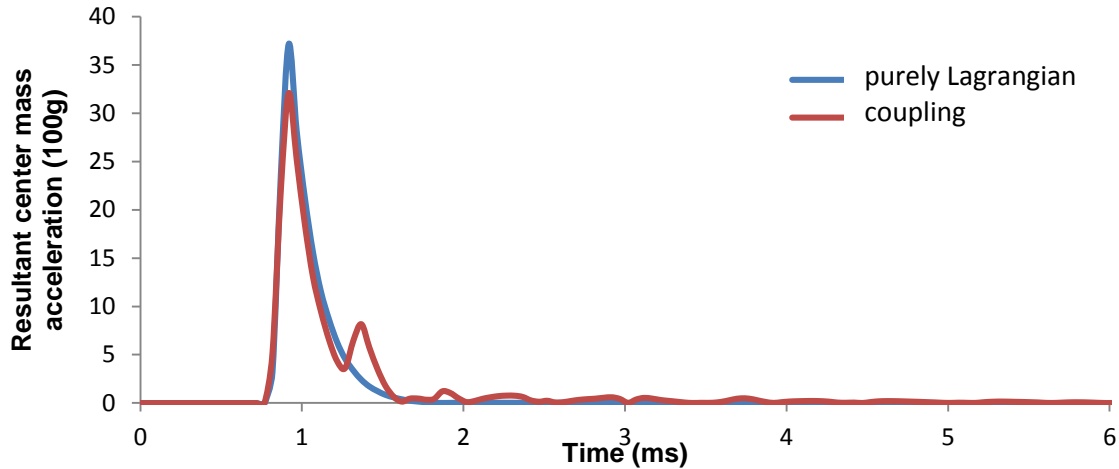
Figure 5-5. Variation of the resultant center mass acceleration of the free solid structure under the same blast scenario modeled with two different methods.

5.4. Fluid and Structure Interactions

Modeling a head model which is exposed to a blast wave is a difficult challenge. Air (fluid) domain experiences a large deformation while deformations in the structural (solid) domain is small. Therefore, a dissimilarity is happened between two different domains and two different formulation is used, Eulerian and Lagrangian formulations for fluid and solid, respectively.

To determine the complex interaction between the dynamic responses of a Lagrangian structure and the Eulerian fluid it is required to use a fluid-structure interaction (FSI) system. A typical FSI problem is solved using a specific contact between the interacting bodies; air media elements and head elements. In this model, a penalty coupling factor is used in the Lagrangian-Eulerian interface. The penalty coupling algorithm searches the relative displacement between a Lagrangian node and the Eulerian fluid material at each time step and calculates the coupling forces on the node of the structure (slave node) and those of the fluid (master nodes). The calculated force is considered as an external nodal force on the Lagrangian structure. At the same time, flow through the Lagrangian mesh must be controlled by the algorithm to keep the physics

73

of the problem [120]. The procedure of defining proper contacts, implementing ALE and FSI and, most importantly, the mesh size make it inevitable to give assurance of the results accuracy. Parametric studies on the mesh size of the air should be performed to make certain that the actual load of the Eulerian air blast is transferred to the Lagrangian head structure through FSI penalty method. To do this, several different element sizes of the air domain were considered to find the optimum mesh size while the head model was exposed to the same blast scenario and the biomechanical parameters of the brain were compared. The element size of less than 7 *mm* demonstrated an acceptable dimension as the response of the brain converges to similar waveforms. If the mesh size was greater than 7 *mm*, the biomechanical parameters increased which resulted in overestimation of the actual response of the brain. The effect of the Eulerian elements size on the resultant center mass acceleration of the brain was presented in Figure 5-6.
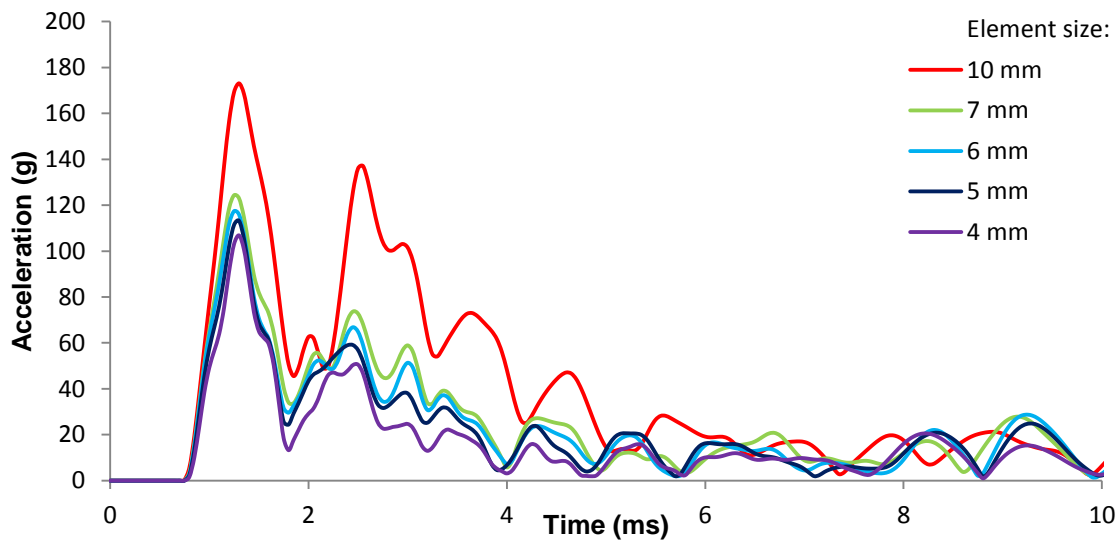
Figure 5-6. Parametric study to find the appropriate element size for the media.

5.5. Effect of the Helmet on the Responses of Human Brain under Blast Loads

5.5.1. Effect of the head on the blast propagation with and without a helmet

The variations of the pressure with time in the ambient layer were presented in Figure 5-7 for different mass of TNT. The results indicated that an increase in the mass of the explosive

material caused a higher pressure at an earlier arrival time to the ambient layer. The kinematical

responses of the head; such as the center mass displacements and accelerations of the brain and

the skull; as well as the mechanical response of the brain such as ICP and the maximum shear

stress in the brainstem; were monitored when the head was exposed to the blast loads with and

without a helmet. Figure 5-8 showed the center mass displacements of the brain due to different

blast loads in both cases; with and without the helmet and under the different mass of TNT.

Identical patterns were followed as shown for all TNT masses. In general, the effect of the

explosion mass on other kinematical and mechanical responses of the head-neck components

was similar.
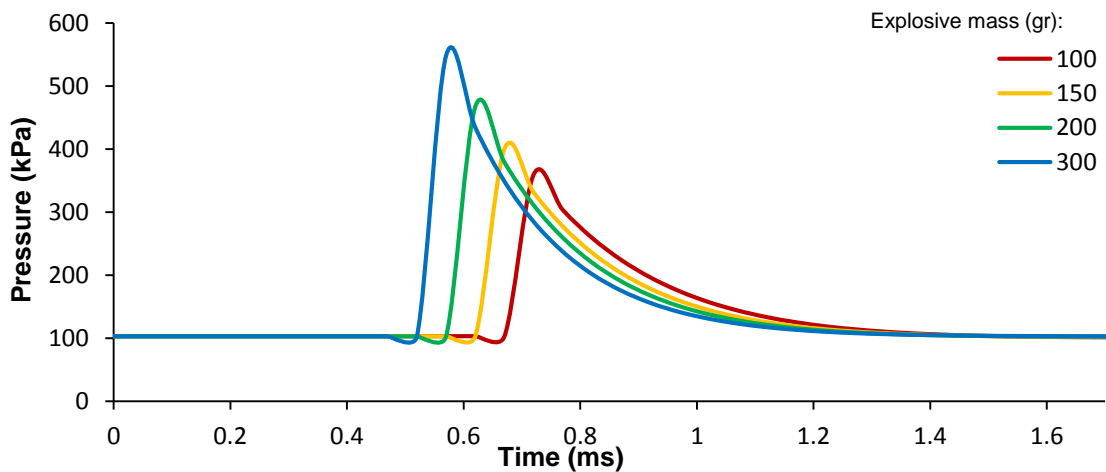
Figure 5-7. The variations of the pressure with time in the ambient layer.
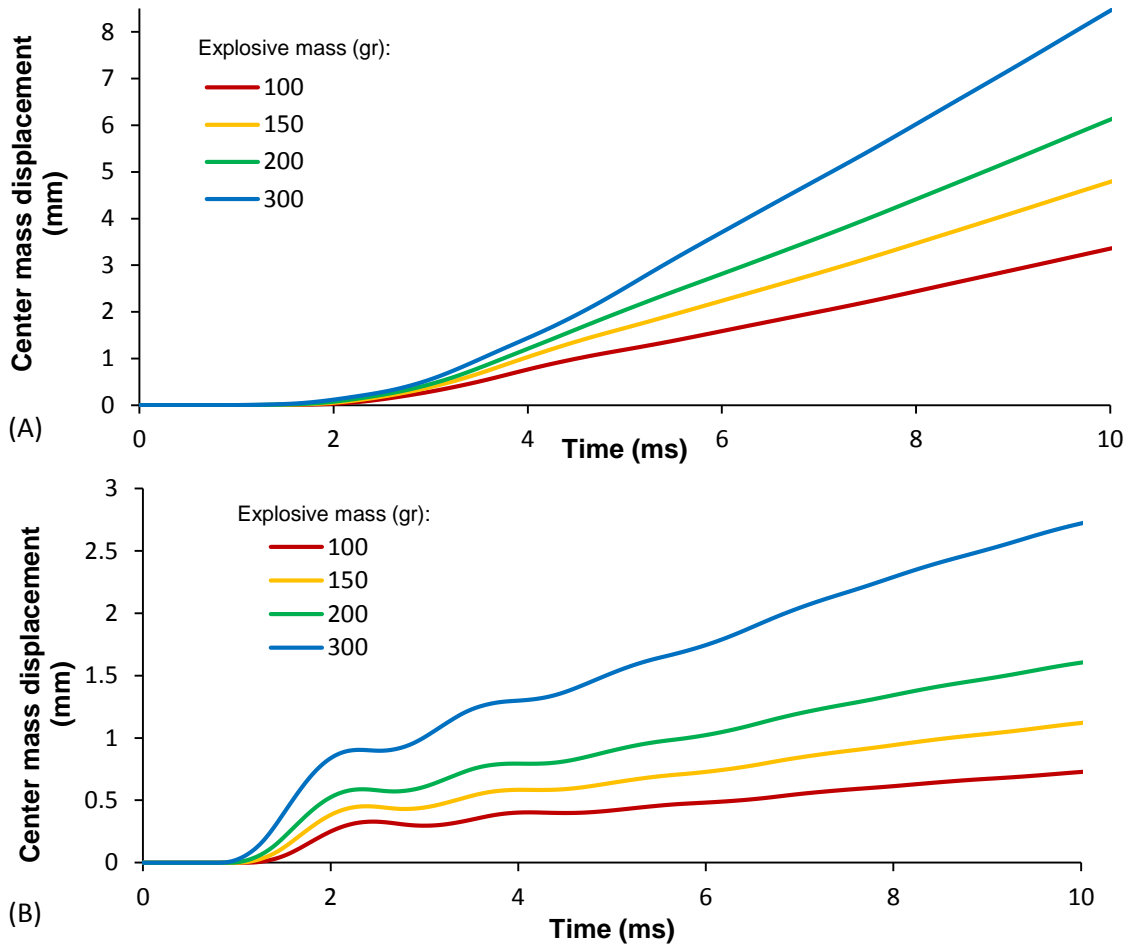
Figure 5-8. Center mass resultant displacements of the brain: (A) with helmet and (B) without a helmet due to different detonation mass.

The contours of propagation and the interaction of the blast waves on the head resulted

from explosion of 200 *gr* TNT, with and without the helmet, at different times were presented in

Figure 5-9. The scale of the response can change due to variations in the head and helmet size

and geometry. In this example, as shown in Figure 5-9, the concentration of the pressure waves

moved across the head with time. Helmet had an influence on the level of pressure and its

concentration area. Figure 5-9(A) and (B) showed the shock wave interactions and variation of

pressure level on the head with and without the helmet. When the head was protected with,

helmet 13% reduction in the overpressure can be seen as shown in Figure 5-9 (A)-(b) and (B)-

(b). Furthermore, comparing the blast wave propagation of the two scenarios indicated that

utilizing the helmet makes a barrier over the head and protects it from the shock front Figure 5-9 ((A)-(b), (A)-(c), (B)-(b), and (B)-(c)).

The change of pressure with time at several locations around the head-neck model was presented in Figure 5-10. The overpressure peaks at identical locations from the explosion site before reaching the head or helmet were equal in both scenarios (locations 1 and 2). The overpressure reflections, however, were different (R_1 and R_2 against $R_1^{'}$ and $R_2^{'}$) as illustrated in the figures. The reflected peak pressures were higher when the helmet is used. Different values can be seen in locations 3 and 4 as the waves approached the head or the helmeted head. This was due to the reflections as well as the geometrical pattern that the waves find through. The pressure surged to around 0.8 MPa (location 3 in Figure 5-10 (A)) just before the waves reached the helmet. However, the recorded pressure was much lower in the corresponding location for the head without a helmet (location 3, Figure 5-10 (B)). The maximum overpressure reached 0.7 MPa at location 4 (Figure 5-10 (B)), when the head was not protected, at a distance further from the explosion and closer to the head in comparison with the protected head. This was the result of the profile of the helmet that impacted the development of the pressure distribution. Considering locations 5, a delay in the peak overpressure was seen for the helmeted head due to the profile and geometry of the helmet.
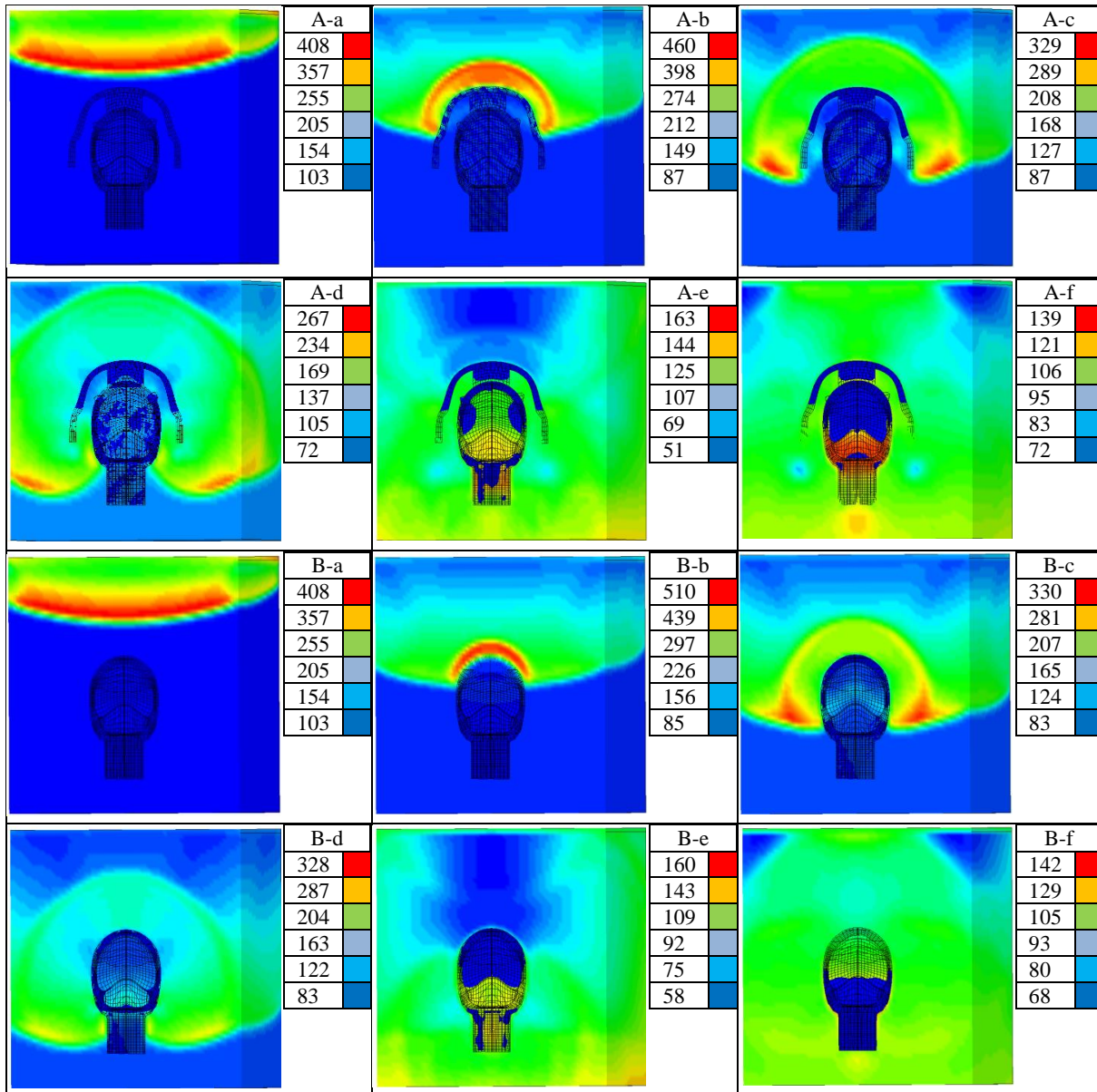
Figure 5-9. The shock wave interactions with the human head and the variation of the pressure (*kPa*) in the media at: (a) 0.72, (b) 0.92, (c) 1.1, (d) 1.22, (e) 1.82, and (f) 2.6 milliseconds after the explosion for both cases: with helmet (A) and without helmet (B) due to 200 *gr* of TNT.
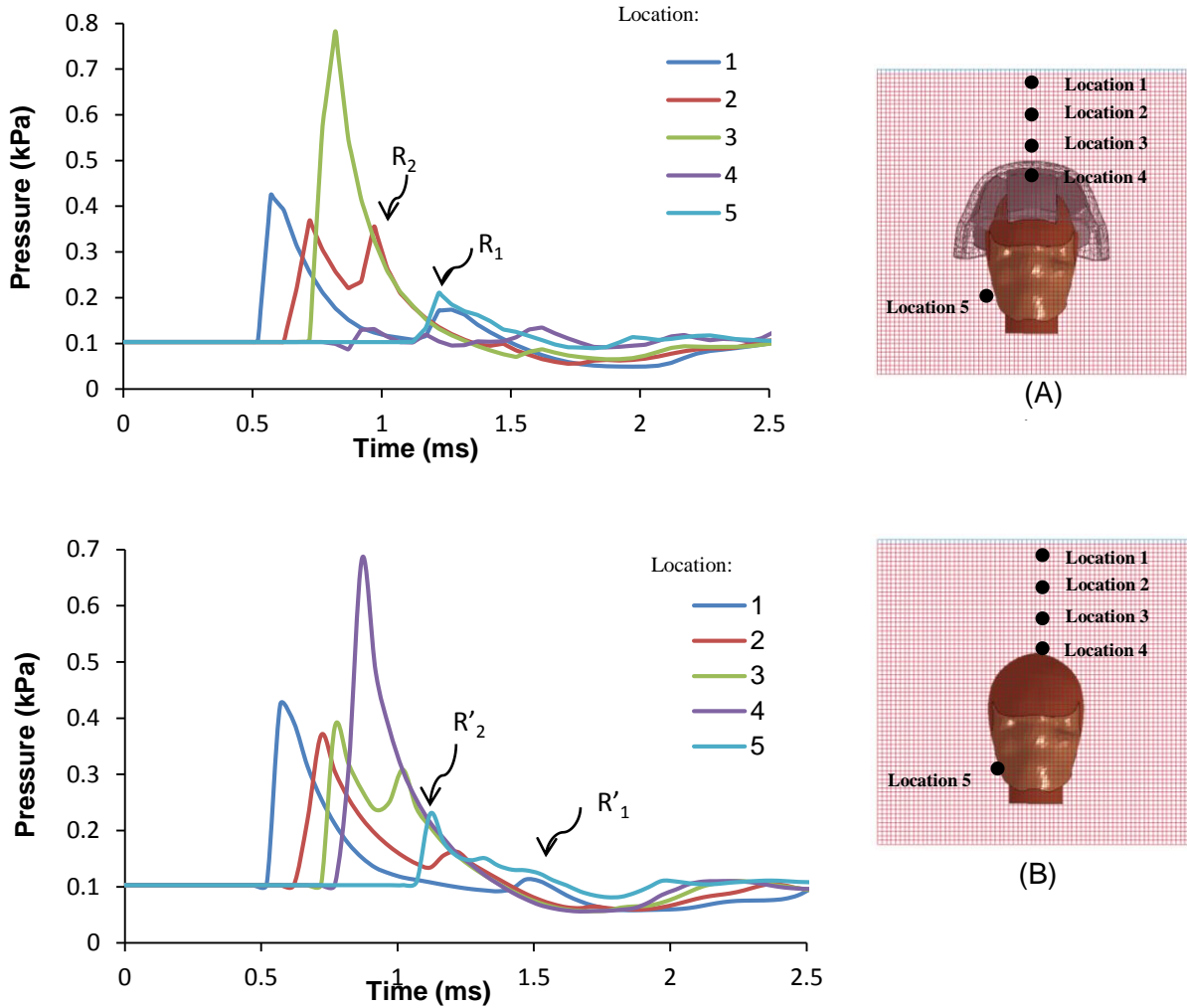
Figure 5-10. The blast wave reflections and the pressure variations with time at selected locations in the media: (A) with helmet and (B) without helmet due to 200 *gr* of TNT.

5.5.2. Brain motion and displacement

The brain and skull are of different stiffness and weight, and hence different displacements are expected, due to overpressure. External impacts on the skull may cause brain injury due to incompatibility of the motions of the skull and brain, even in the absence of a skull fracture. This type of injury may happen in the frontal and temporal lobes regardless of the direction of impact [121]. Accelerations of higher than $80g$ can create negative pressure on the contrecoup site of the brain resulting in cavitation, particularly in the absence of a helmet. This may cause collapse of the vapor bubbles producing pressures in excess of even 1,000

atmospheres, which can cause considerable damage [122]. Studying the displacements and accelerations of the brain and skull can, therefore, be helpful in predicting the severity of the brain injury.

In Figure 5-11, the center mass displacements of the skull and brain were plotted. The helmet padding foams usually used in the helmeted-head model allowed the blast load to go to the head smoothly from the helmet and caused a much smoother motion of the brain and skull together. In the absence of the helmet, the incoming shock waves directly hit the skull resulting in sudden movements of head. The shock loads was transferred to the brain after a few milliseconds. Figure 5-11, demonstrated the center mass displacements of the brain and skull for both protected and unprotected head. The size of the displacements for the helmeted head was larger as the mass of the helmet had an influence on the overall motion size, but the differences between the motion of the skull and the brain was much smaller for the helmeted head.
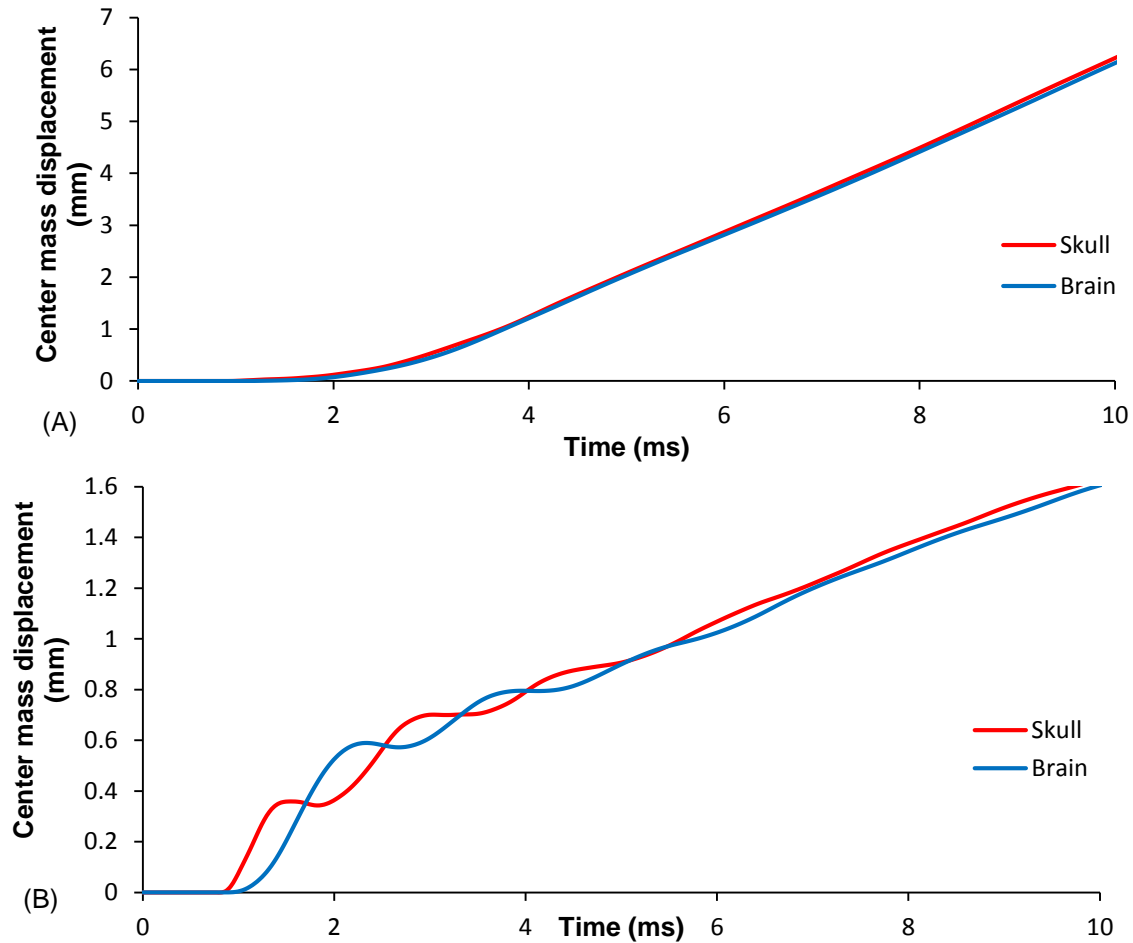
Figure 5-11. Center mass resultant displacements of skull and brain: (A) with helmet and (B) without helmet due to 200 *gr* of TNT.

As it previously discussed, the blast wave propagation distributions around the head were different for the head model with and without the helmet. These overpressures caused rapid movement of the head. Figure 5-12 illustrated the resultant center mass velocities of the skull and brain for both cases. In the absence of the helmet, the oscillation of the skull and brain displacement was finally settled on a simultaneous velocity, while for the helmeted head, the brain and skull displacements were very much identical from the start of the incident.
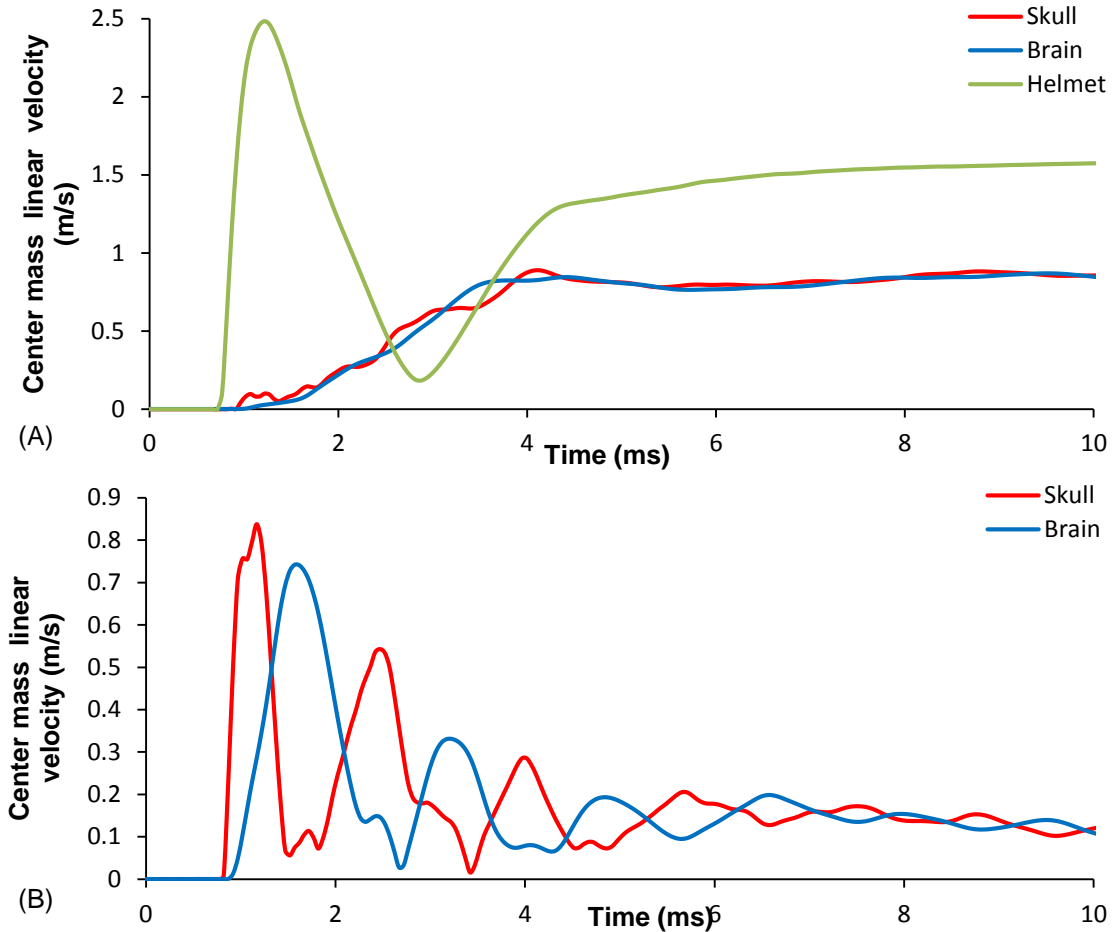
Figure 5-12. Center mass resultant velocities of skull and brain: (A) with helmet and (B) without helmet due to 200 *gr* of TNT.

Direct or indirect external impact to the head and neck causes an acceleration or deceleration of the head which might result in injury [123]. The size of linear acceleration has been used to estimate injury criteria in vehicle crash testing [124]. In the helmeted head analysis, due to presence of pads in the helmet, a major part of the impacted energy will be absorbed before reaching the skull. As a result the size of the shock has been diminished, and thus there is a considerable decrease in the head components accelerations (Figure 5-13). Comparison of Figure 5-11 and Figure 5-13 indicated that the head components were loaded by the blast before having a significant motion in the head. The maximum center mass accelerations of the brain for the head, with and without helmet, were around 50*g* and 150*g*, respectively, for 200 *gr* TNT.

82

Figure 5-13 demonstrated the variation of the center mass accelerations of the brain with time due to different blast wave intensities. As expected for both cases, by increasing the mass of the explosive material, the brain acceleration started earlier and at the higher level. For the reason of clarification, the maximum values of brain accelerations with and without the helmets were experienced under the different amount of explosive materials that were presented and compared in Figure 5-14 and Figure 5-15.
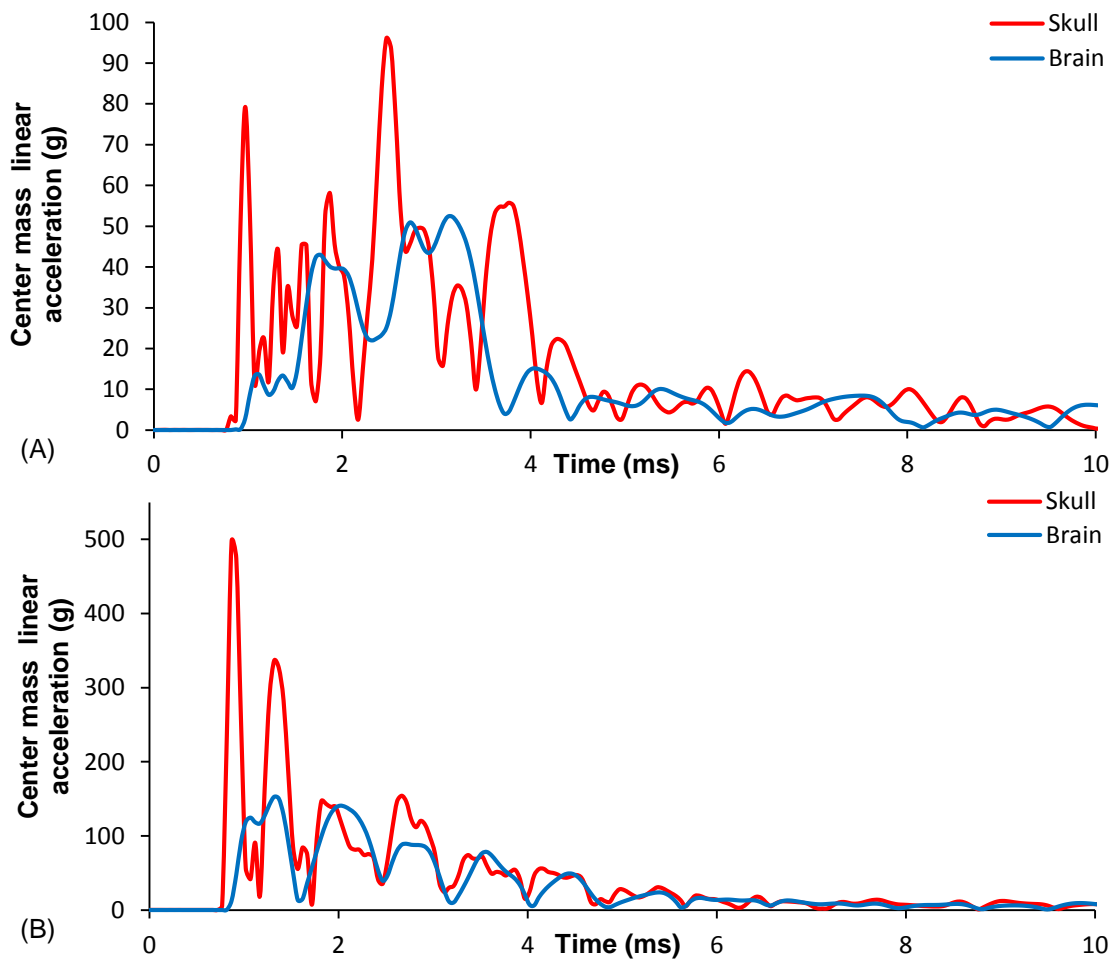
Figure 5-13. Center mass linear resultant accelerations of skull and brain: (A) with helmet and (B) without helmet due to 200 *gr* of TNT.
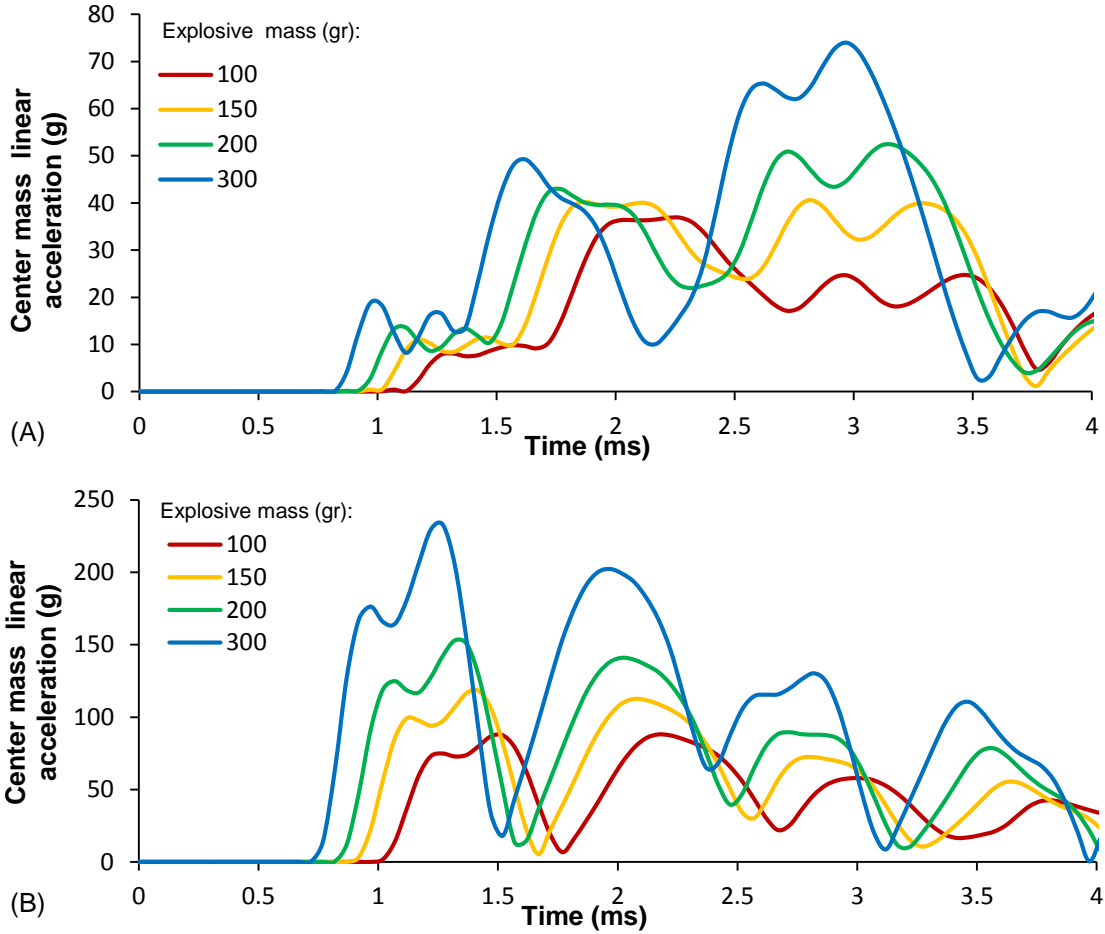
Figure 5-14. Center mass linear resultant accelerations of brain: (A) with helmet and (B) without helmet due to 200 *gr* of TNT.

	100 grams	150 grams	200 grams	300 grams
Max acceleration without helmet	83.04	118.08	152.97	232.84
Max accelerationwith helmet	36.8893	40.5948	52.3313	74.0205
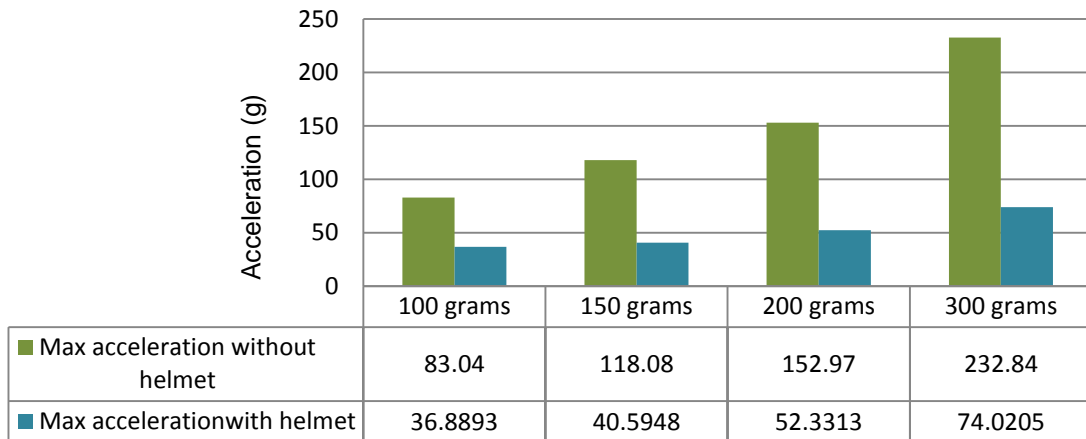
Figure 5-15. Comparison of maximum linear resultant accelerations of brain, regarding different amounts of explosive material mass.

5.5.3. Intracranial pressure distributions

It has been proven that the duration of overpressure and the number of waves play major roles in the severity of the brain injury due to the blast [125]. It is also mentioned that in a short duration blast event peak pressure and duration are affected the harshness of brain injury while at longer durations (more than 20 milliseconds) the level of brain injury only depends on the overpressure [126]. In Figure 5-15, contours of ICPs at different times after the blast were presented for both the protected and unprotected heads. When the blast waves hit the head or helmet, a pressure concentration appeared on the coup site of the brain. However, a region of negative pressure (tension) was created at the countercoup site. At the initial time of the incident, coup and countercoup sites were similar to the classic coup and countercoup response to direct impact [66]. The coup and countercoup regions (positive and negative ICP), however, changed with the progression of the pressure waves across the brain.
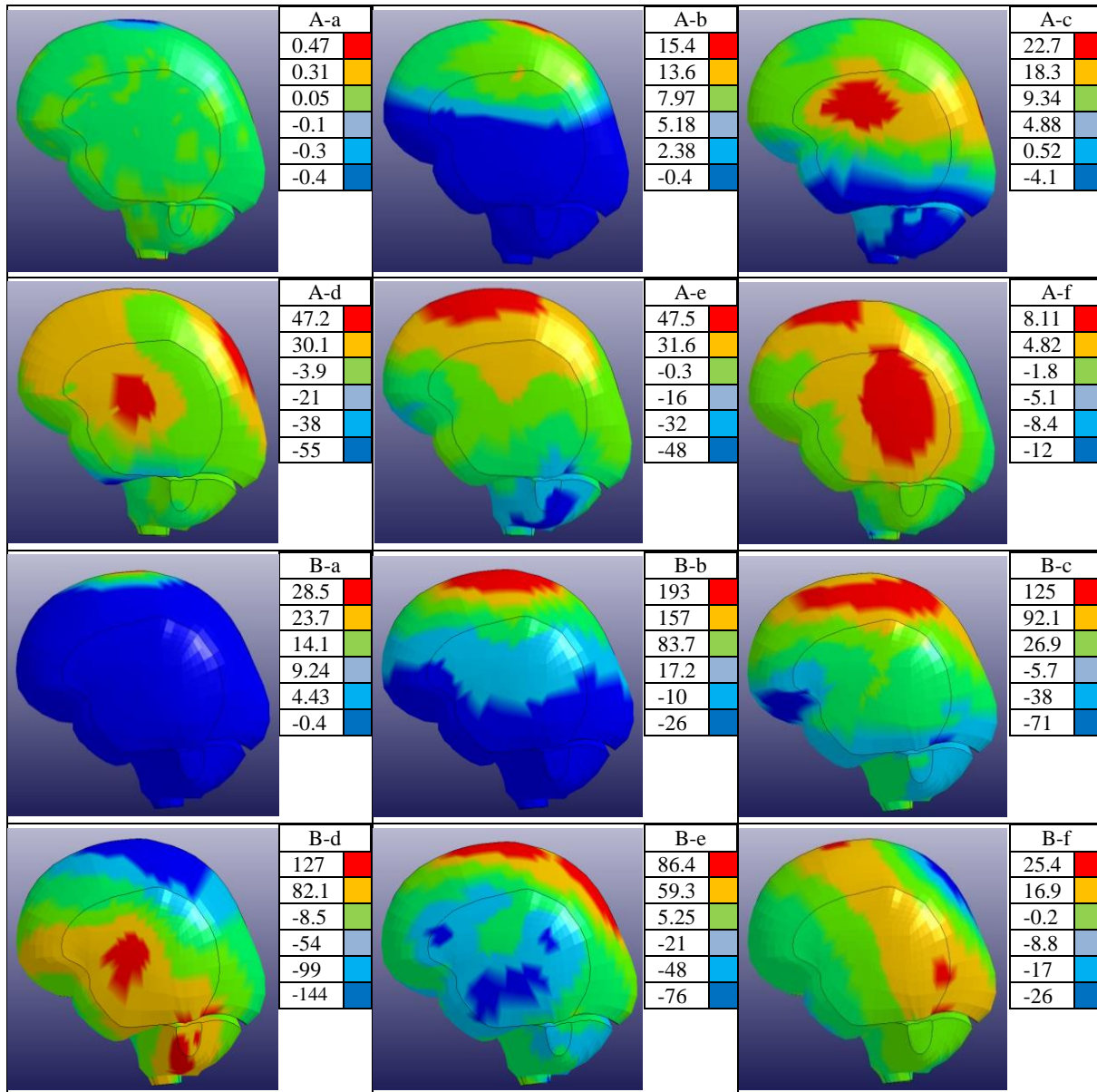
Figure 5-16. Contours of ICP at (a) 0.87, (b) 1.02, (c) 1.12, (d) 1.92, (e) 3.02, and (f) 10 milliseconds after detonation; (A)with and (B)without helmet due to 200 *gr* of TNT.

The changes of pressure with time on the uppermost part of skull, experiencing the maximum pressure, were also presented in Figure 5-17. The ICP changes with time in the coup site of the brain was shown in Figure 5-18 with and without helmet. The results indicated that maximum pressure on the skull with the helmet was noticeably less than the case of without the helmet (1.6 *MPa* versus 0.3 *MPa*, respectively). This pressure, however, can be simply tolerated by the skull having the compressive strength of about 96 *MPa* [127]. The maximum experienced

ICPs when the head was with and without a helmet were around 60 and 190 kPa, respectively.

As mentioned earlier, relative displacements of the brain with respect to the skull were different

for the two scenarios. When the brain movement was less than the skull movement, the brain

withstand compression stress and the ICP was positive and vice versa. The results can be

validated by comparing Figure 5-11 and Figure 5-18. The center mass displacements of the brain

and skull were shown in Figure 5-11, when the blast wave hit the unprotected head. The skull

moved quickly while the brain did not and the ICP in the coup site was thus positive at this stage.

It took about 1.5 milliseconds after the blast initiation that the displacement of brain became

higher than that of the skull, and the coup site elements withstood tension load so the ICP

became negative. Sudden pressure variation on the brain from compression (positive) to tension

(negative) and vise-versa causes sudden change to the volume and density of the cells with a

subsequent damage in tissue.
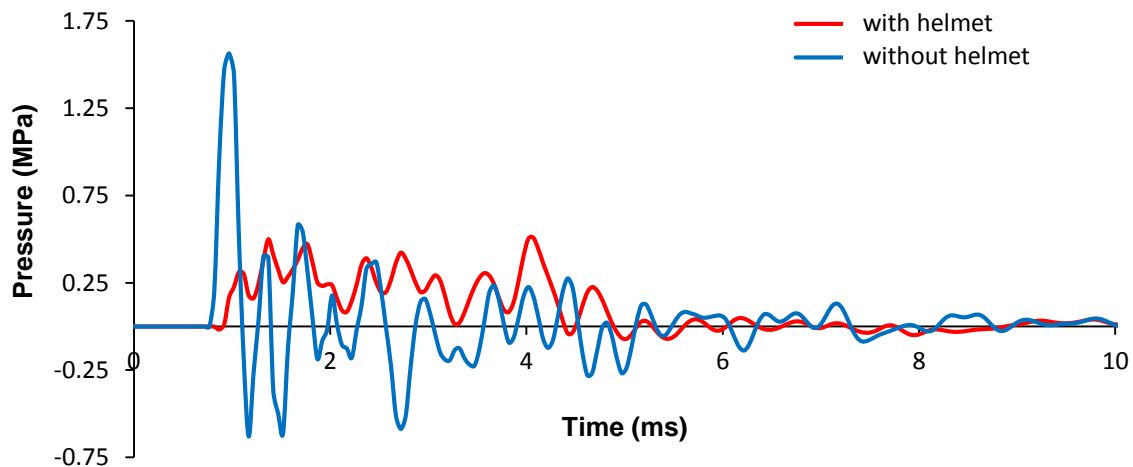
Figure 5-17. Variation of the pressure versus the time on the corresponding hit area of the skull: with helmet and without helmet due to 200 gr of TNT.
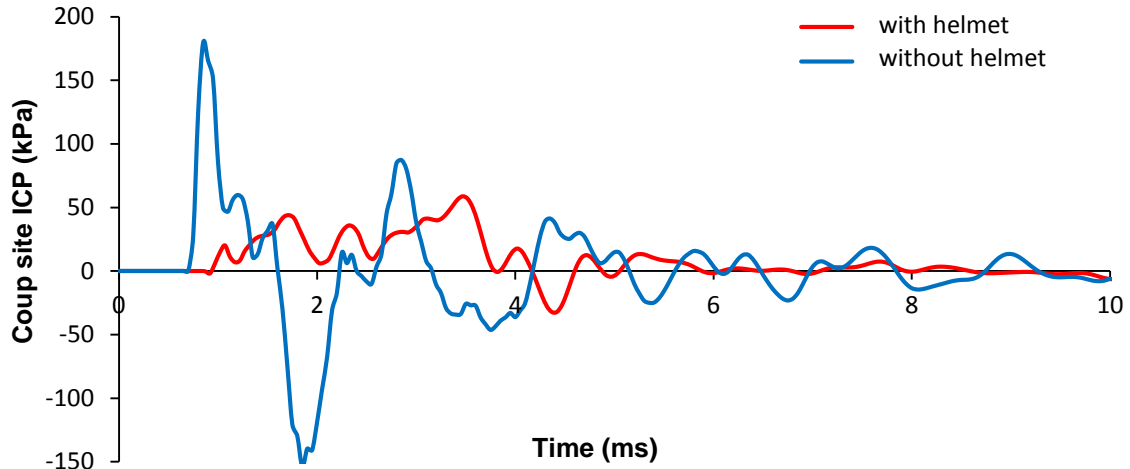
Figure 5-18. Time variation of the ICP in the coup site: with helmet and without helmet due to 200 *gr* of TNT.

The variations in the ICP values and its maximum in the coup site with the change in the amount of explosive are presented in Figure 5-19 and Figure 5-20. The results indicated that the both maximum ICP in the coup site and center mass acceleration of the brain increased by increasing the explosive mass. In the absence of the helmet, increasing the ICP and acceleration is quite significant.
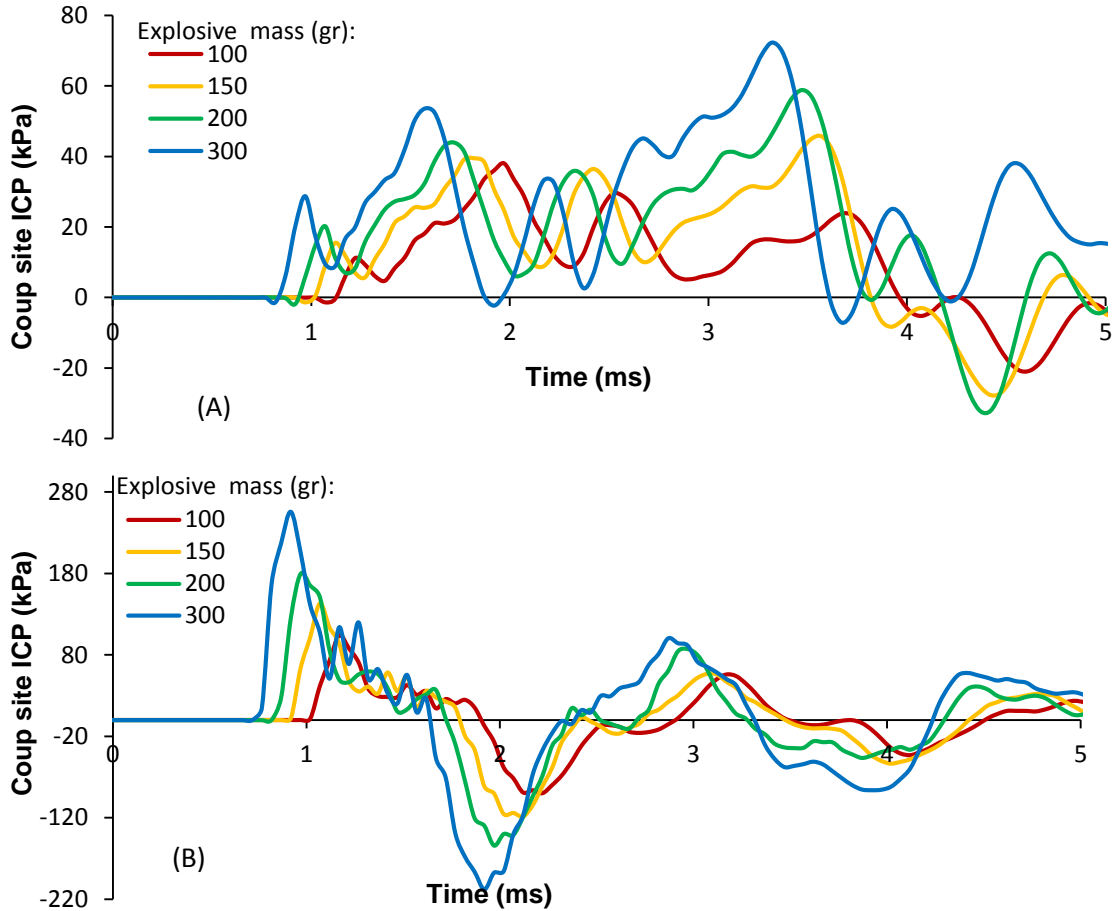
Figure 5-19. Time variation of the ICP in the coup site of the brain versus different explosive material mass: (A) with helmet and (B) without helmet due to 200 *gr* of TNT.

	100 grams	150 grams	200 grams	300 grams
Max pressure in the ambient layer (kPa)	359.4	400.7	467.3	548.6
Max ICP without helmet (kPa)	103.943	143.257	179.46	255.913
Max ICP with helmet (kPa)	38.0601	45.7329	58.8621	72.3181
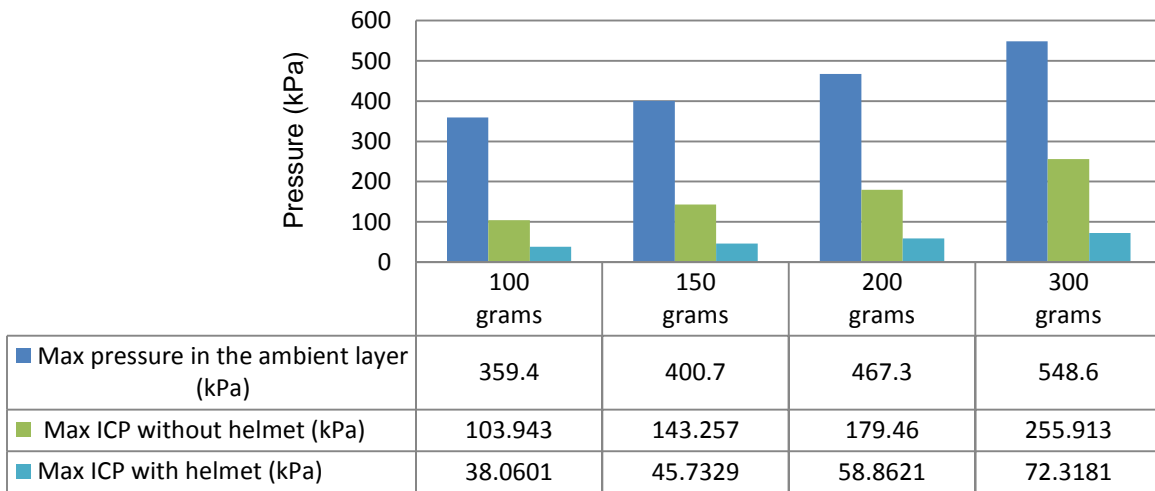
Figure 5-20. Comparison of maximum ICPs in coup site versus different amounts of explosive material mass.

5.5.4. Brain average shear stress distribution

As a result of the development of high shear stresses/strains, Diffuse Axonal Injury (DAI) may occur when the brain comes under a mechanical impact force [128]. The brain is of low shear modulus in bulk and cannot tolerate high level of shear stresses. The brain stem is the area that maximum shear stress is usually expected under blast waves and kinematical motions. Average variation of the maximum shear stress versus time in the brain stem was presented in Figure 5-21. Tracing the amount of shear stress showed that the brain stem experienced the maximum shear stress in both cases. In the absence of the helmet, the peak of the shear stress occurred a few milliseconds earlier with a larger value compared to the helmeted head.
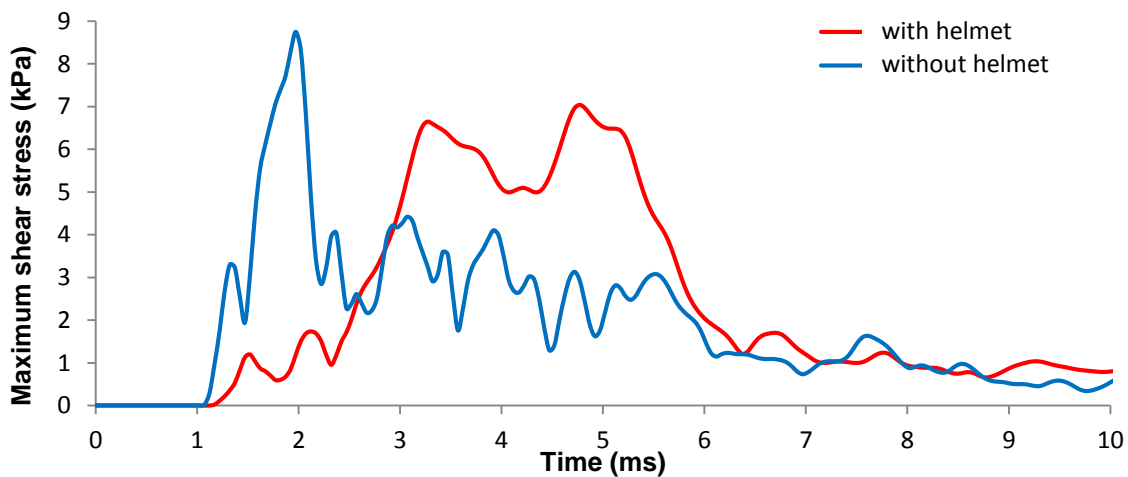
Figure 5-21. Variation of the maximum shear stress versus the time in the brainstem: with helmet and without helmet due to 200 gr of TNT.

5.6. Different Blast Wave Orientations

In this part of the work, the efficiency of the helmet in reducing the level of injury under three different blast orientations was studied using a helmeted human head-neck model. The blast scenarios are simulated when the blast waves hit the head component: (A) top of the head, (B) front of the head and (C) back of the head. The standoff distance in all cases was one meter from the explosion point with the mass of HE is 200 gr. Center mass accelerations of the brain as

well as intracranial pressure (ICP) in the coup site were monitored and compared when the head

is protected and unprotected. Figure 5-22 compared kinematic response of the brain. As the

results showed, in all situations brain experienced a sudden acceleration due to exposure to blast

wave and the maximum acceleration was experienced in the first few milliseconds. The amount

of the peak acceleration, however, was related to the blast orientation. Moreover, when the head

was unprotected, maximum acceleration was generally at higher level.
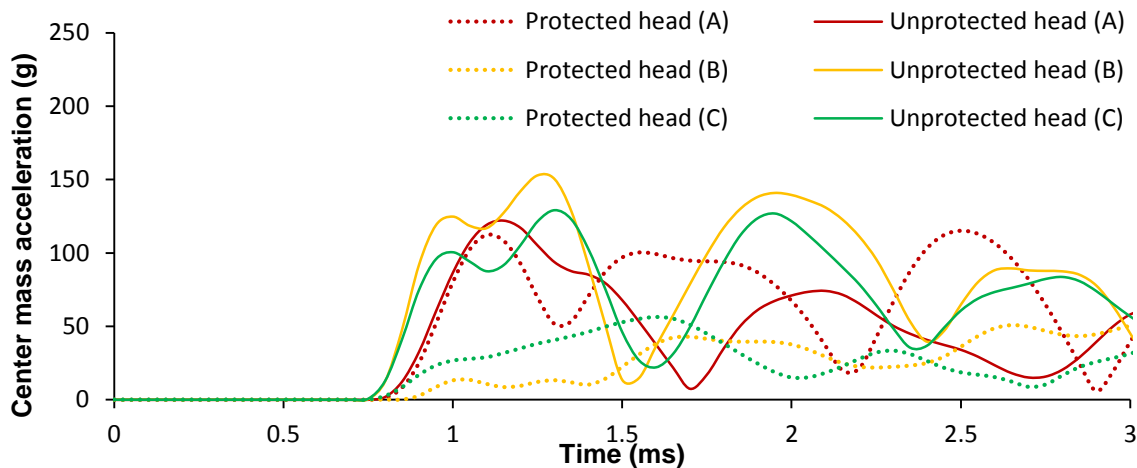
Figure 5-22. Center mass linear resultant accelerations of brain when detonation was; (A) in front, (B) above and (C) back of the head.

The helmet played an important role in reducing the level of the ICP. Figure 5-23 showed

the variation of the ICPs under different situations; with and without helmet. As far as the

efficiency of the helmet was concerned, in frontal blast orientation the head was minimally

protected. Therefore, the efficiency of the helmet was the least during frontal blast. For the case

of detonation from the top, on the other hand, the effect of helmet was the highest, due to the

maximum coverage of the helmet in this situation. The highest and the lowest level of

experienced ICPs due to several blast wave orientations when the head was protected and

unprotected were compared in Figure 5-24.
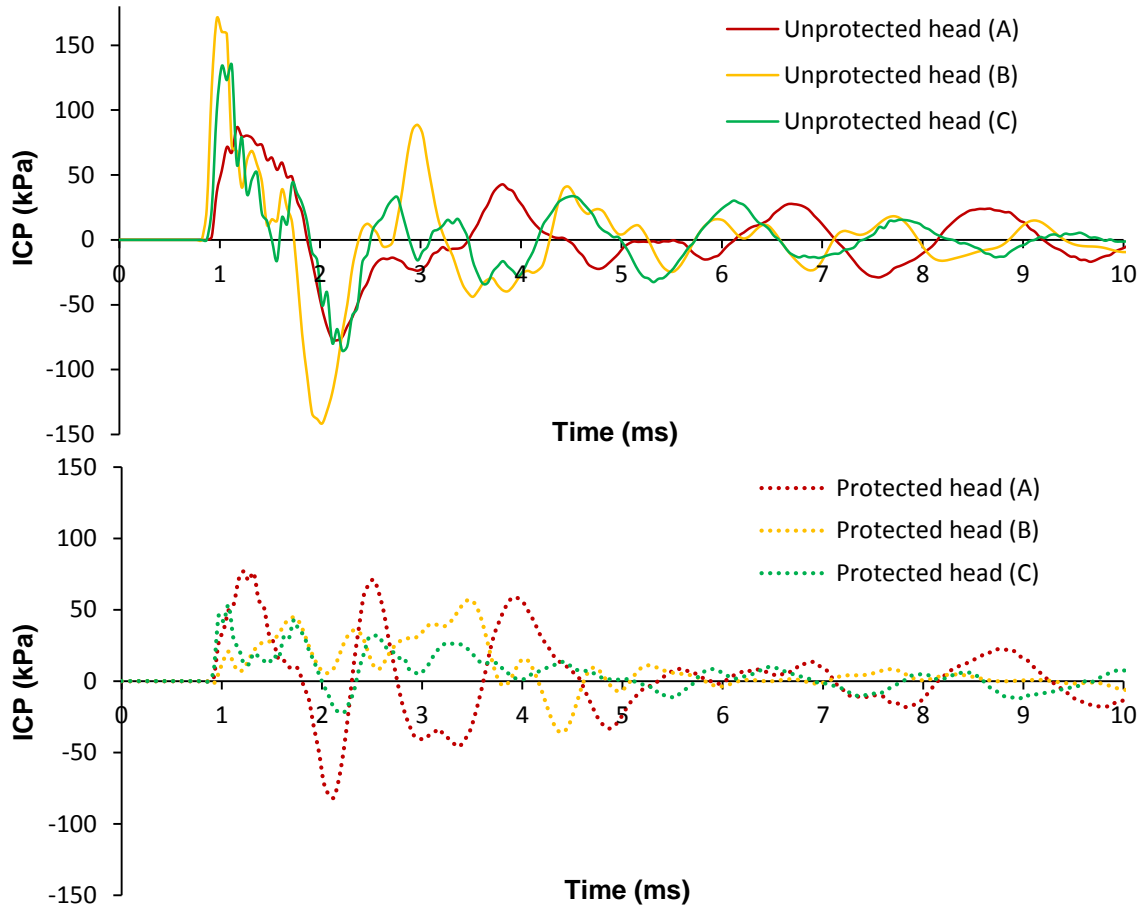
Figure 5-23. Variation of the ICP in the coup site when detonation was; (A) in front, (B) above and (C) back of the head.
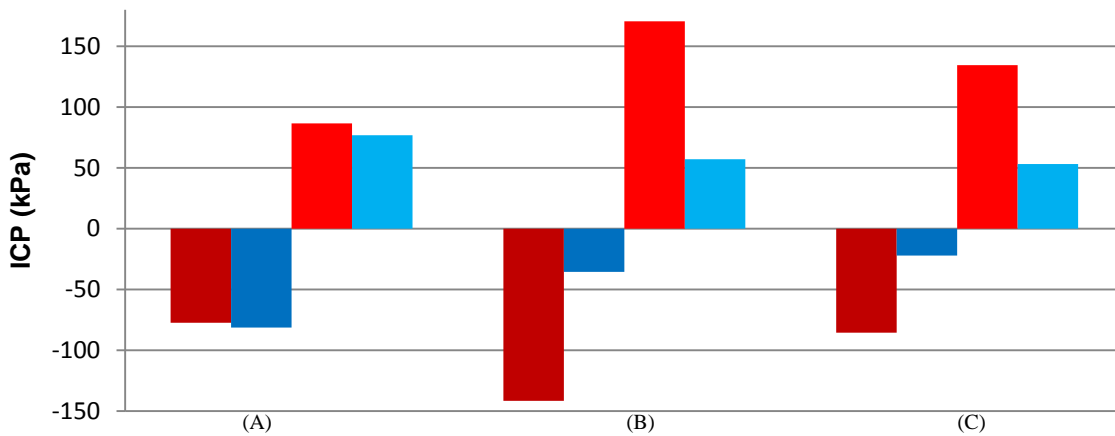
Figure 5-24. Maximum and minimum ICPs in different orientations.

5.7. Inclusion of the Body under Blast

A finite element (FE) model of human head-neck with and without being attached to the body (human body excluding head and neck) has been exposed to blast waves. In this regard, three different models are proposed; *model a*, the head-neck free in space; *model b*, the head-neck fixed at its bottom; and *model c*, the head-neck attached to the body (a more realistic model) (Figure 5-25). To study the effect of the body regarding to the blast orientation, four different blast directions with respect to the head orientation (Figure 5.26) were also considered. These models were utilized to examine the impact of the body on the biomechanical responses of the brain after the blast shock waves hit the head for about 50 *ms*. This specific time interval was selected to monitor the responses of the brain after the blast wave passed through the entire head and was diminished. The body was assumed as a rigid extra part attached to the neck. Mass of the attached body is 85 *kg*.
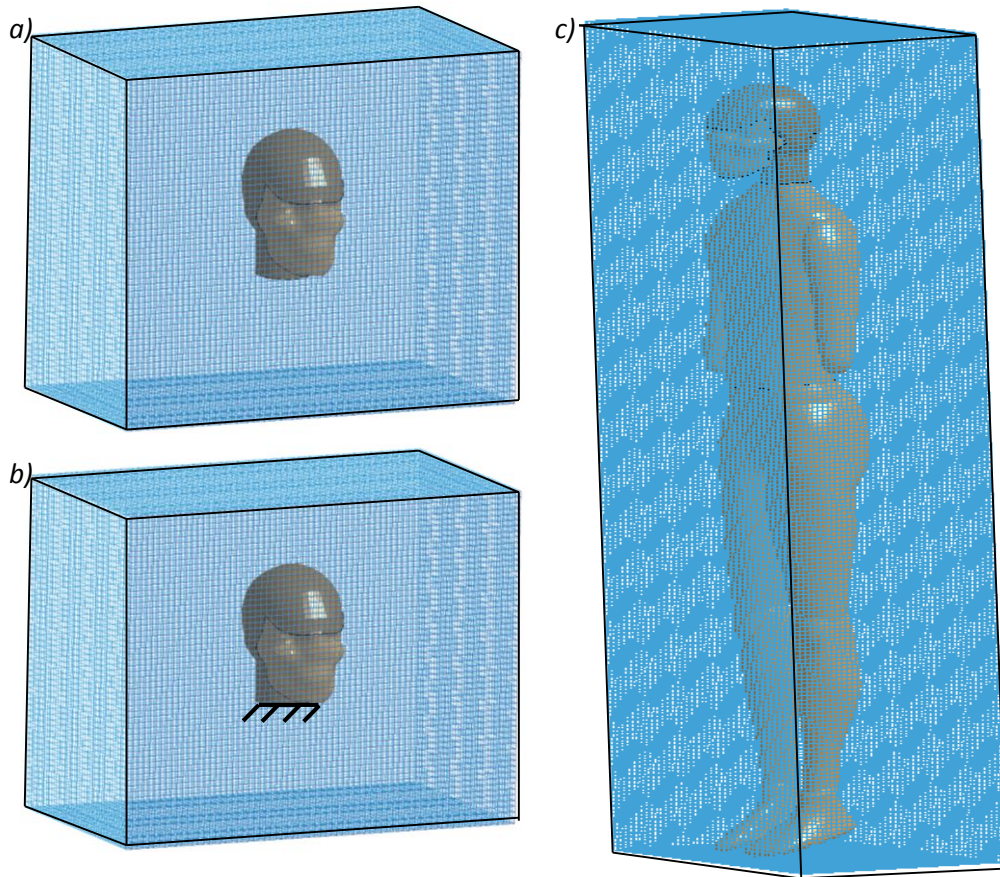
Figure 5-25. Model a) the head-neck model is free; model b) the base of the neck is completely fixed; and model c) head-neck model is attached to the body.
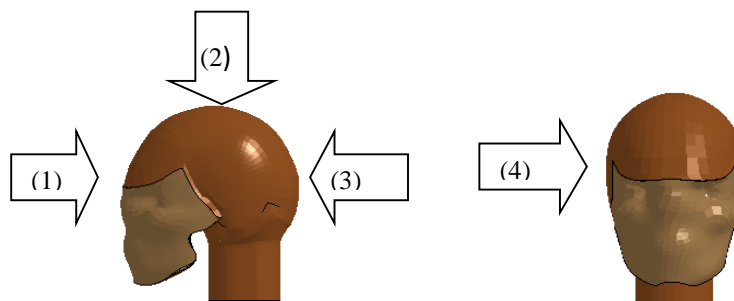
Figure 5-26. Four different blast wave directions with respect to the head orientation; (1) blast waves from the front, (2) blast waves from the top, (3) blast waves from the back, and (4) blast waves from the right side.

Figure 5-27 illustrated the air pressure contours in the blast condition all around the head. Comparison between the top and bottom rows clearly demonstrated the effect of the torso on the propagation of the wave underneath the head. Also, the pressure at several random points around

the head was measured and shown to represent the complexity of the waveform when it passed

around the head (Figure 5-28). The blast wave completely passed the head in less than 2

milliseconds. Due to blast wave reflections from the torso in model c, the overpressure behind

the body (region A) was amplified and washed over the head (denoted in this study as wash-over

effect) while in models a and b, this significant effect of the body was missed. However, for all

cases, when the blast wave passed the head, the time-history over pressure varied around the

head.
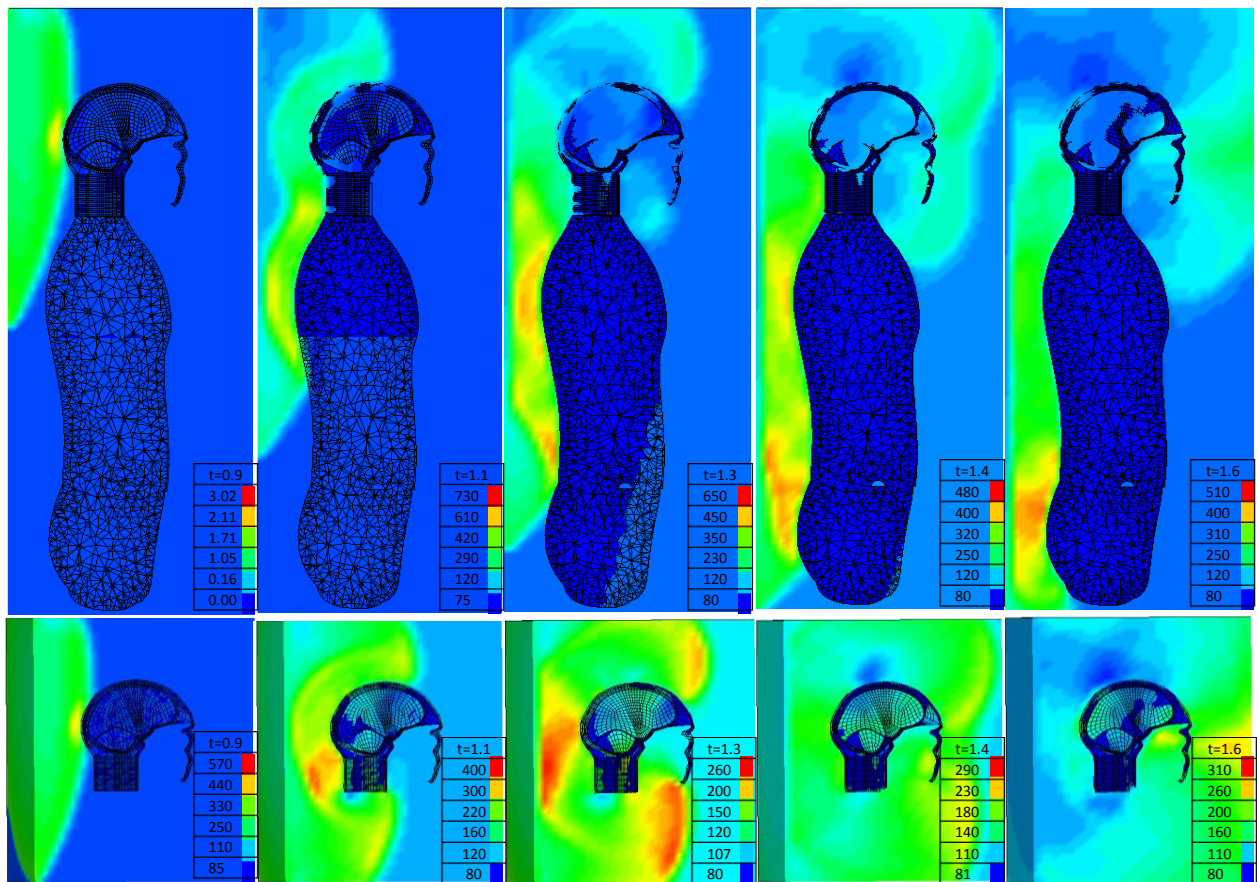
Figure 5-27. Blast wave propagation and variation of the blast overpressure (*kPa*) around the head at different time (*ms*) after the explosion with and without body when blast waves hit the back of the head.
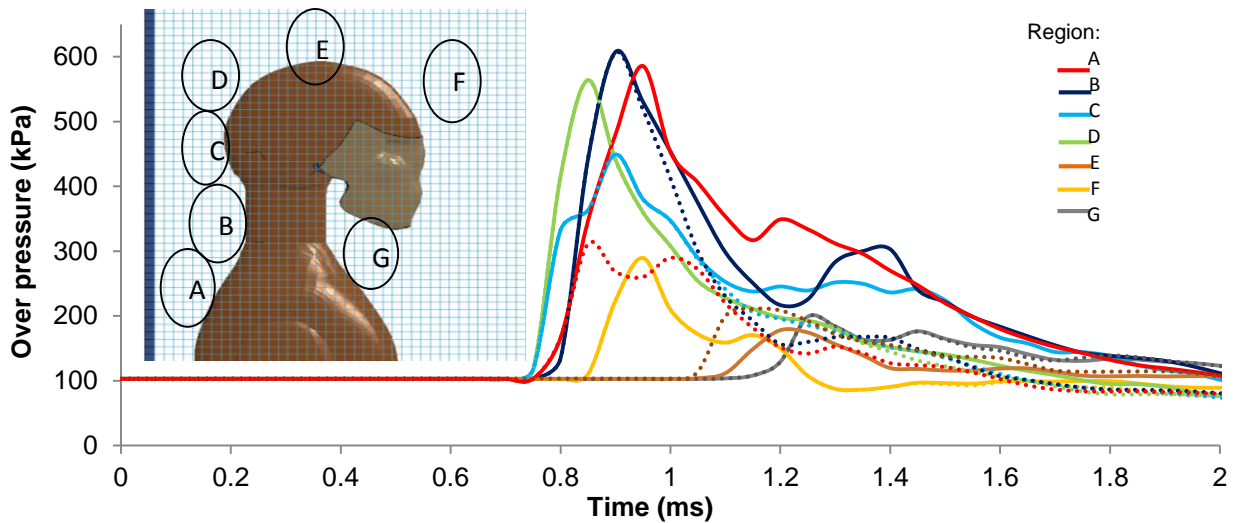
Figure 5-28. Variation of the blast overpressure with time in different regions around the head, with body (solid lines) and without body (dashed lines) when blast waves hit the head from the back.

5.7.1. Brain acceleration

Considering the variation of the center mass acceleration of the brain under the different blast wave directions, the brain experienced the maximum acceleration in the first few milliseconds after being hit by the shock wave. In Figure 5-29, the resultant center mass acceleration of the brain under various loading conditions was presented. The results explained that both the maximum pressure value and the pattern of time-history acceleration, in all three models, were not considerably affected by the inclusion of fixed neck or the trunk. Figure 5-29 showed slight changes which are ignorable compared to the whole wave form. It should be also noted that the level of accelerations were different when their directions were changed. The detonation material ranged from about 180g to 330g for the blast scenarios from the front and the side, respectively. This large discrepancy was because of the complex geometry of the human head model.
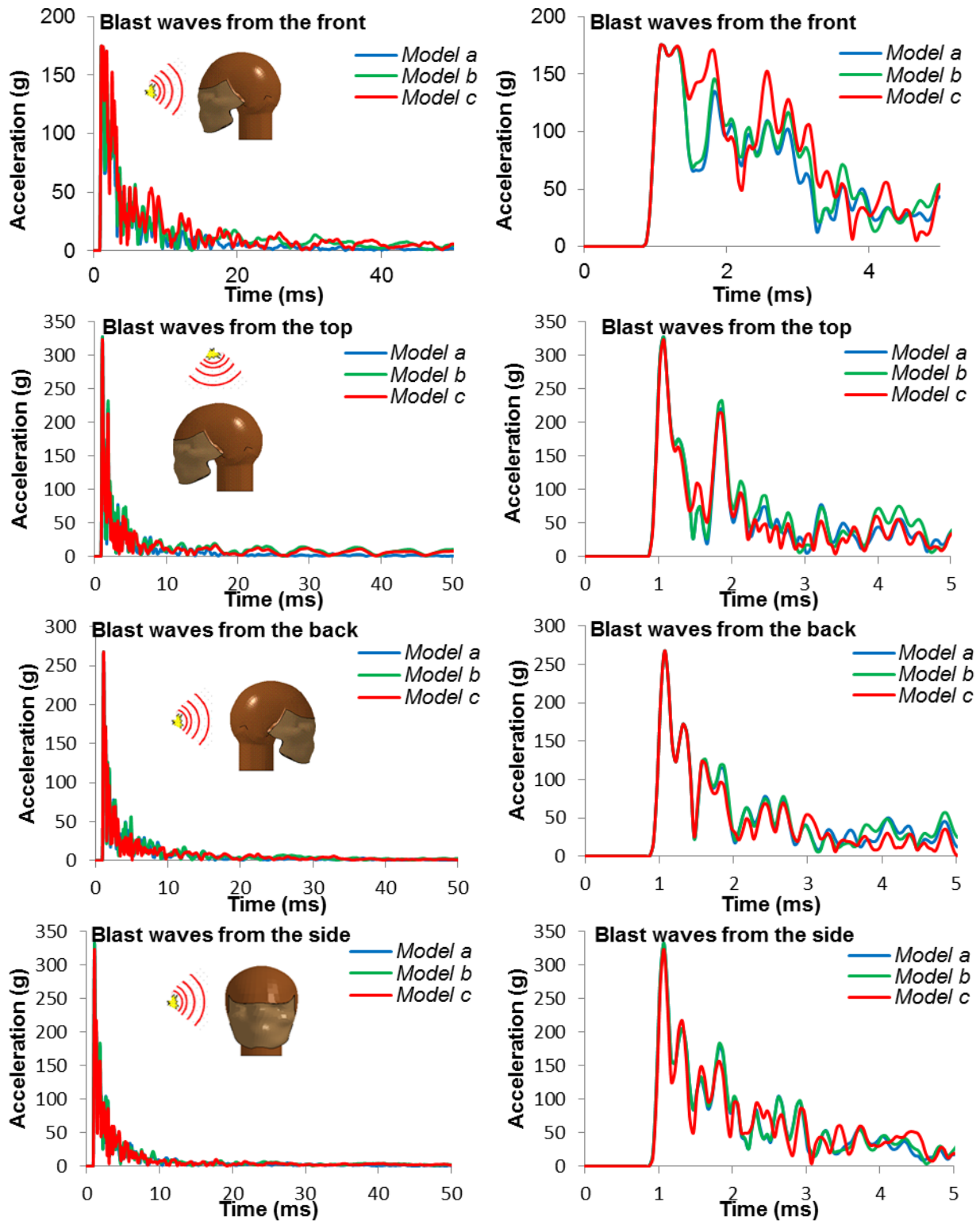
Figure 5-29. Variation of the resultant center mass acceleration of the brain with time for different models under different blast waves directions.

5.7.2. ICP in the coup site

After the impact of the blast waves with the head, the pressure on the brain (average of the sum of the principal stresses) was dramatically changed due to the stress wave and the relative motion of brain with respect to the skull. ICPs distribution of model c at different times were presented in Figure 5.30 when the blast hit the back of the head. As shown, ICPs in the coup and counter coup sites of the brain were changed rapidly.
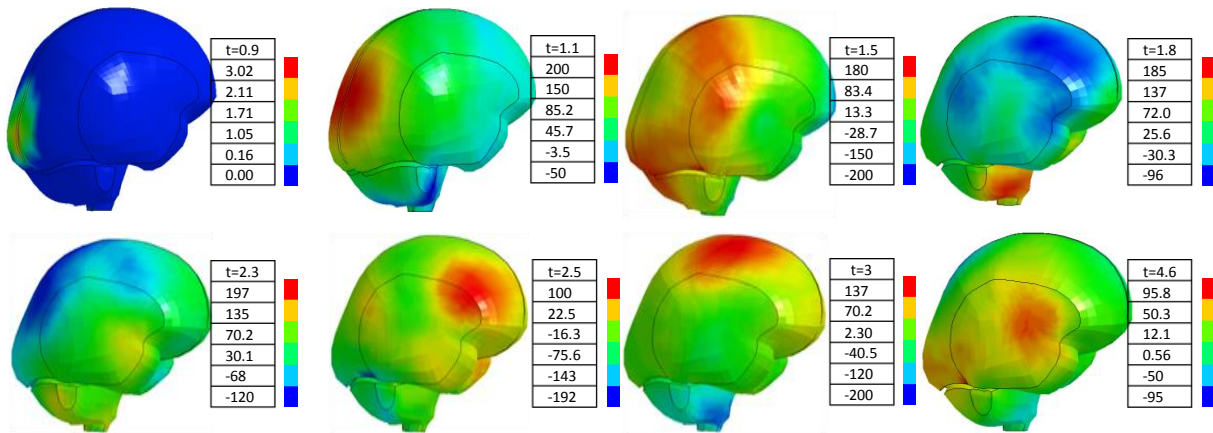
Figure 5-30. Contours of the ICP (*kPa*) at various times (*ms*) after the explosion (blast waves from the back).

Variations of ICP on the brain in different scenarios were shown in Figure 5-311. Similar to the center mass acceleration, the maximum ICPs in different directions varied, with the maximum occurring in the blast waves from the side. The geometries of the head components had a major role in such a difference. Variations of the ICPs in the coup sites indicated that there were no considerable differences for different models except for the blast waves from the front. When the body was attached, however, the changes in ICPs showed about 30% increase when the whole body (model c) is exposed to the blast waves.
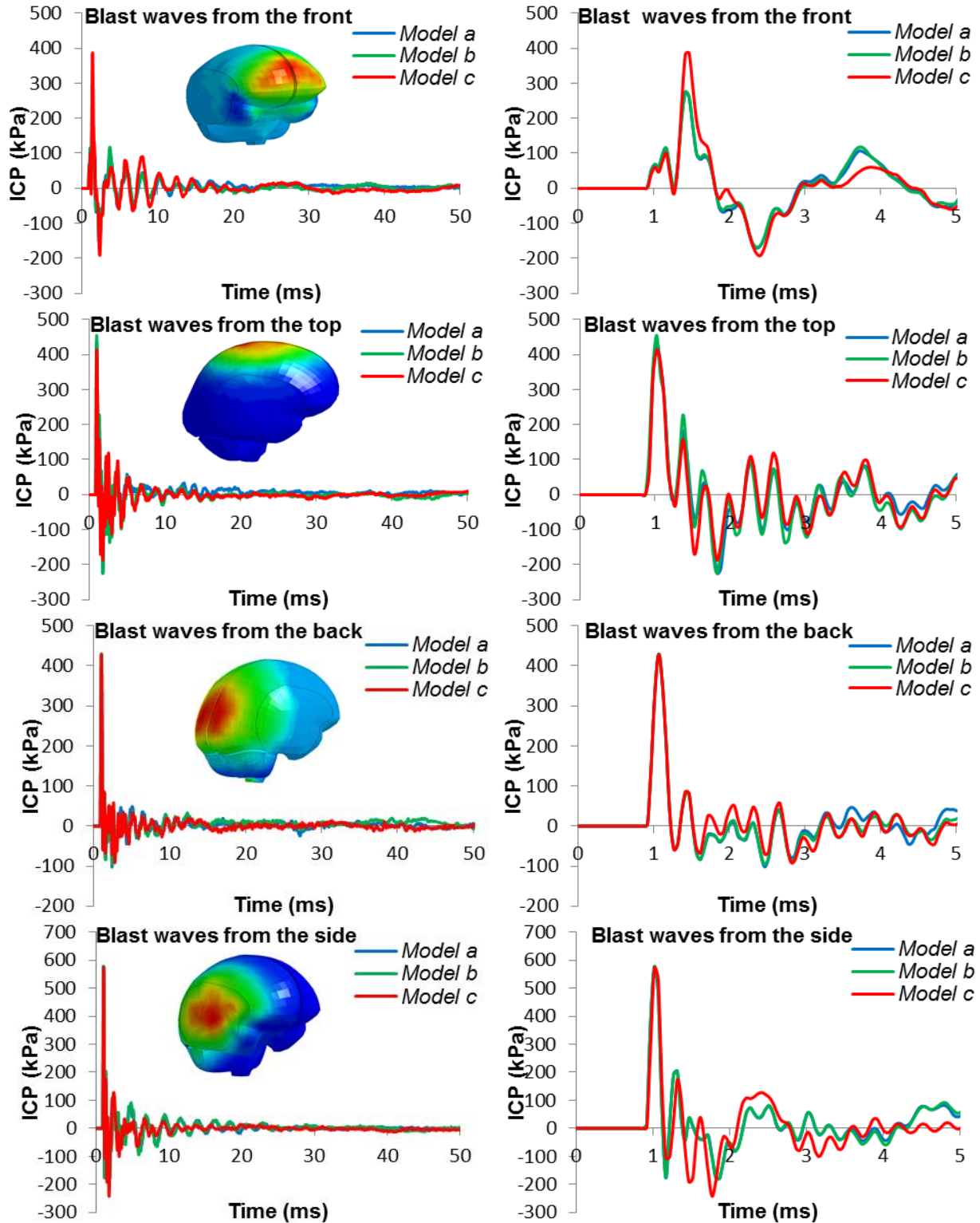
Figure 5-31. Variation of the ICP with time for different models, under different blast waves directions.

The ICP peak values of different models regarding to various blast directions were compared in Figure 5-32. It was clear that the head experienced the highest ICP in the coup location in the blast from the side (around 580 kPa for all models) and the lowest in the blast from the front (around 275 kPa for models a and b). Moreover, the results in the blast from the front showed that models a and b predicted the same peak of ICPs but compared to the model c, they underestimated the actual ICP on the brain due to the wash-over effects and the geometry of the model. It is worth mentioning that the effect of wash-over in various blast wave directions were different but when the blast hit the body from the front, the effect was magnified due the complexity of the face bone that produced stagnation area under the jaw.
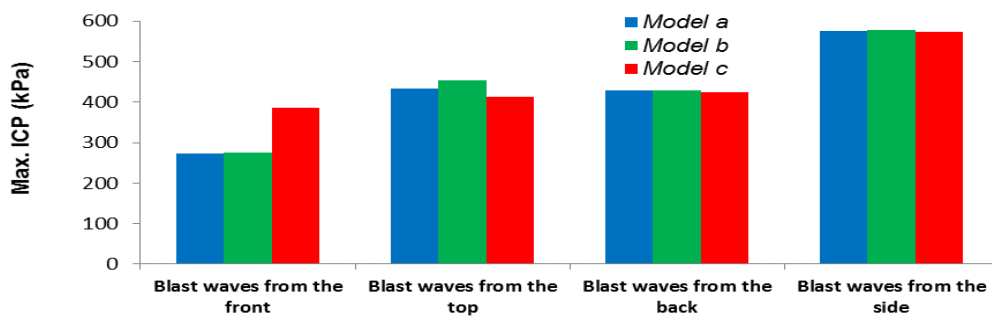
Figure 5-32. The ICP peak value time for different models, under different blast wave directions.

5.7.3. Shear stress on the brainstem

As a result of the development of high shear stresses/strains, diffuse axonal injury (DAI) may occur when the brain comes under a mechanical assault [128]. The shear modulus of the brain is relatively lower than its bulk modulus. The brainstem is the area that maximum shear stress is usually expected under blast waves and kinematical motions. The results indicated that the shear stress response of the brain depended not only on the inclusion of neck or attached body response, but also on the direction of the blast wave (Figure 5-33). The patterns of shear stress for all scenarios were similar during the first few milliseconds. For longer period of time, the response of the fixed neck head in terms of shear stress became unrealistic with fluctuation.
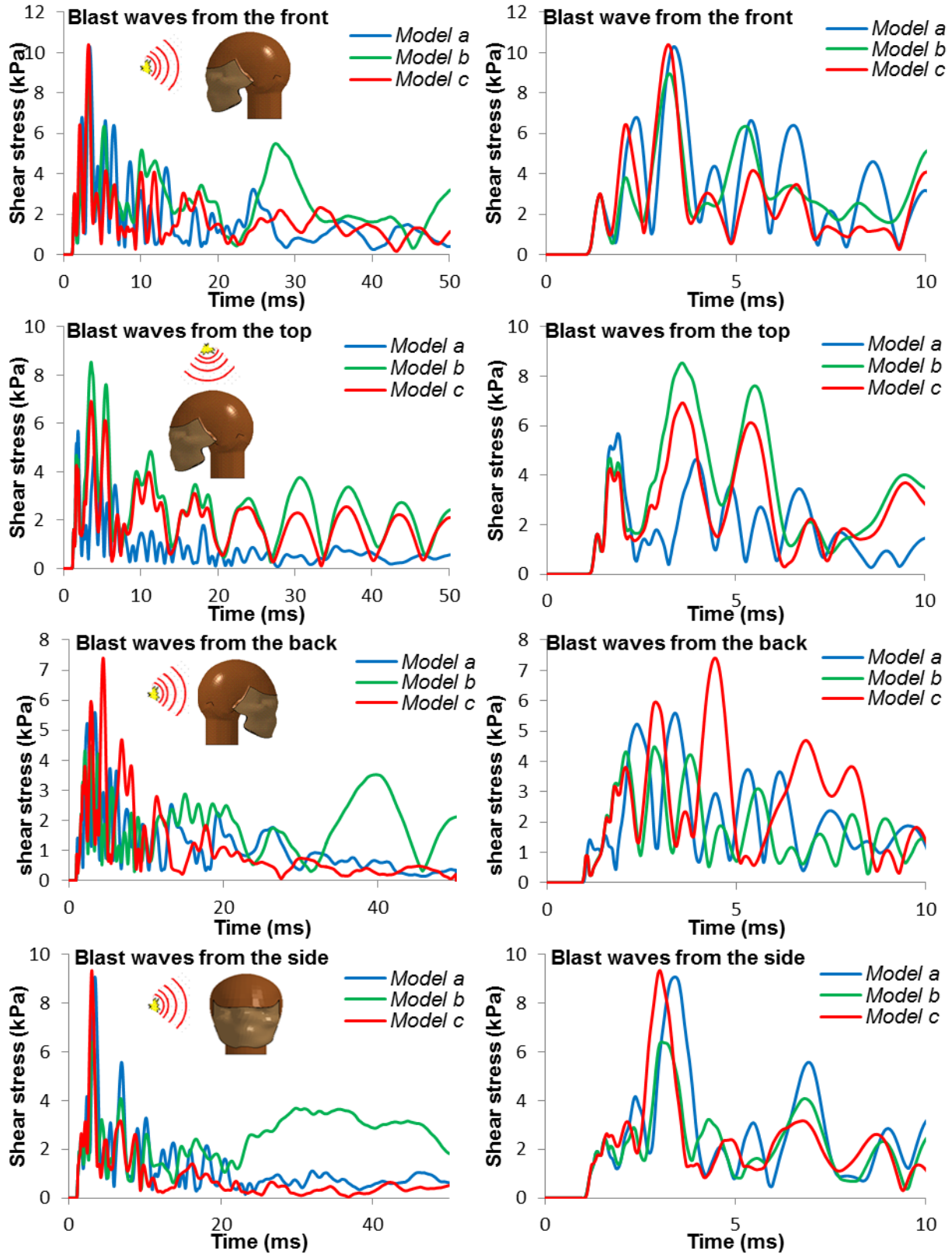
Figure 5-33. Variation of the shear stress in the brainstem for different models under different blast waves directions.

In order to better clarify the effect of different models, maximum level of the shear stresses in the brain stem for separate interval times were measured and demonstrated in Figure . Different directions showed different response of the brain; as it is clearly shown, the brainstem experienced the maximum peak shear stresses under the blast from the front while it was minimum under the blast from the top due to the fact that, in this case, the effect of the blast on the brainstem was mainly compressive load not shear stress. After 10 *ms*, model b overestimated the maximum shear stress in almost all situations. This effect was marked especially after 20 *ms* when the impact of the blast wave completely vanished and the shear stress could be due to the motion of the head itself.
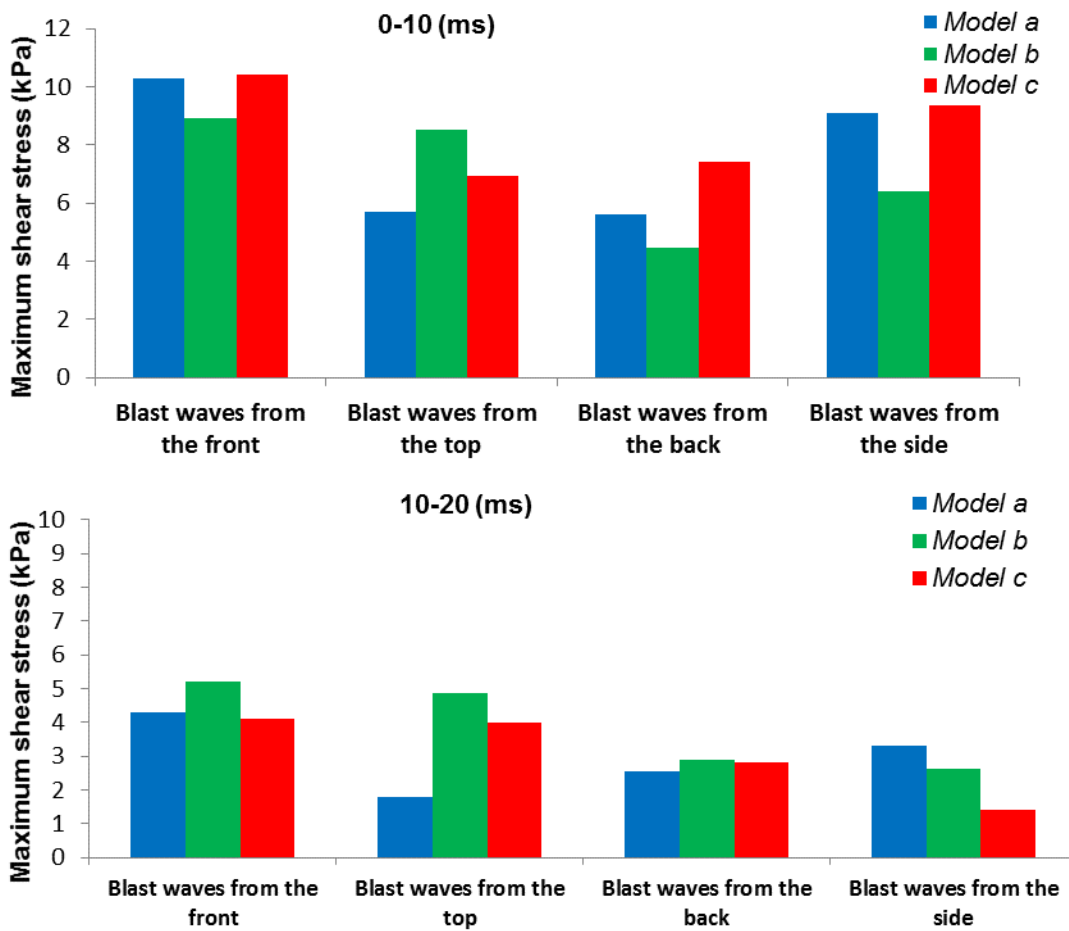
Figure 5-34. Maximum level of the shear stresses in the brain stem for separate interval times.
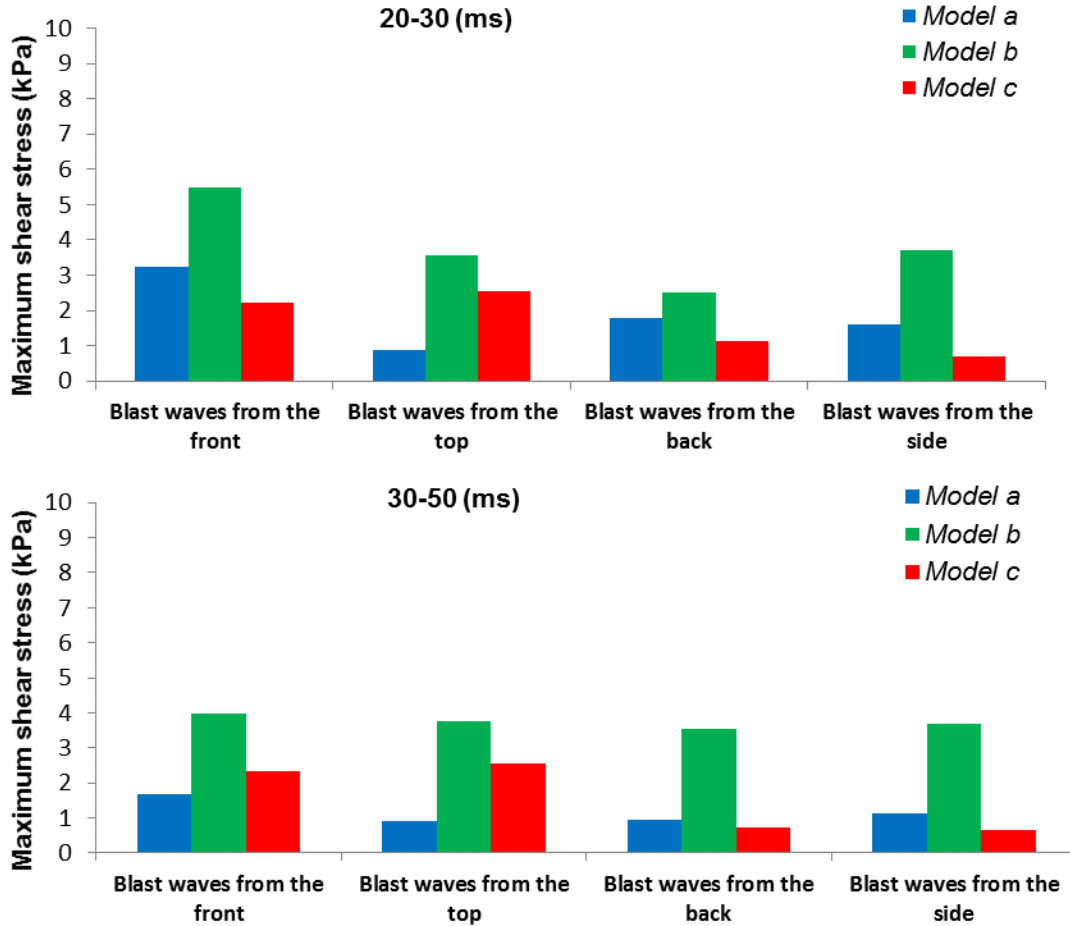
Figure 5-34. Maximum level of the shear stresses in the brain stem for separate interval times (continued).

5.8. Conclusions

A computational study on the effect of wearing a helmet to reduce the level of the brain injury was presented in this part. A coupling of empirical explosive blast load with the multi-material ALE formulation was used to simulate the blast propagation only around the head-neck area. The blast interaction with a solid object was also modeled using a penalty based FSI algorithm. A validated 3-D FE human head-neck model, both with and without a helmet, was exposed to the blast situation. Kinematical and mechanical responses of the brain were recorded and compared for the human protected and unprotected head model. The results of this specific case study indicated that the protected head experienced lower acceleration, lower maximum

ICP, and lower shear stress than the unprotected head. For an explosion of 200 gr TNT at a distance of 1m above the head, the maximum ICP in the coup site region was 180 MPa for the unprotected head. Wearing a ballistic helmet, on the other hand, reduced it to around 1/3 of it to about $60MPa$. Accordingly, maximum linear acceleration of the brain and maximum shear stress in the brainstem of the protected head would decrease to 30% and 78% respectively. Although, it might not be possible to define a critical level of ICP or maximum shear stress, the results indicated that using the helmet provided a notable degree of protection for the brain. The performance of the helmet in regarding to different blast orientations were also considered. The results showed that in any directions the helmet alleviates the level of transferred load to the head. The performance of the helmet, on the other hand, depends on the amount of coverage of the helmet in the blast scenario. In this regard, the helmet can protect the head when the detonation is placed above the head most effectively.

In order to examine the impacts of head orientations with respect to the blast directions as well as the effect of the body on the mechanical response of the brain four different blast scenarios with the head were simulated. Biomechanical responses of the head and brain such as accelerations, brain ICP, and shear stresses were monitored in 50 ms after each explosion. Employing the models of human head in this study showed the extent that the simplified model a and model b without including the body, can be comparable with the realistic model c that the whole body is included. The results contributed to several helpful findings that were summarized as follows:

- In determination of the brain response, the type of head-neck models whether free-floating or fixed without the rest of the body, had little influence on the early interactions of the waves and the brain response. However, this was true only for the

very short period that the neck doesn't realize the effect of head motion. Thus the size of the blast waves had the main contribution to the change of biomechanical parameters in the first few milliseconds.

- The pattern of head acceleration and brain ICP were close and similar for all the three models during the 50 *ms* duration of analysis. There was a difference between the results of model a and model b with the model c with respect to the direction of the blast. The discrepancy came from the fact that in model c, some waves reflected from the torso wash over the head and due to the geometry of the face bone, extra pressure waves hit the head from the jaw. This part was certainly missed in the simplified model a and model b.

- In terms of brain shear stress, the results were different after the initial time; while the three models showed similar behavior for the first milliseconds, those of the fixed-neck (model b) were higher than those of model a after 20 *ms*. This certified the hindering of the motion of the head by fixing the neck overemphasizes the built-in shear stress on the brainstem.

6. SHOCK TUBE

Generation of shock waves that can simulate explosive blast waves, is important to study the bTBI. In the battlefield, blast loads are due to detonation of the explosive materials. The blast waves can be created in several methods for experimental study of the effect of the blast wave loads on structures. One method is obviously through explosive materials that would be dangerous. Using a shock tube that works with compressed gas is an alternative method. A shock tube can produce a plane shock which is propagated along the length of a tube. Shock tubes can be designed at different shapes and sizes. Bauman et al. [129] used a 20.7 m long shock tube with 1 m diameter, while the length of shock tube in the University of Wisconsin was 9.2 m and 25 *cm* square cross section [130].

6.1. Flow through the Shock Tube

Using a constant circular cross section tube and generating a one dimensional flow as a shock wave is the simplest form of shock tubes. Tube is divided to two parts which are separated using a diaphragm. One part which is known as driver has higher pressure air (p_4) and the other part called driven has a lower pressure (p_1) as illustrated in Figure 6.1. Different gases with different properties might be used in the driver and driven sections. When the diaphragm is ruptured, compressed gas in the driver section expands into the driven section and creates a shock wave propagating along the tube with a velocity (V_s). The shock wave rises the pressure and temperature of the gas in driven section and generates a flow following the shock wave at lower velocity. A wave also expands into the driver section as shown in Figure 6.2. A contact surface is created behind the shock wave between the driver and driven gases and follows the shock wave at lower velocity [131] .
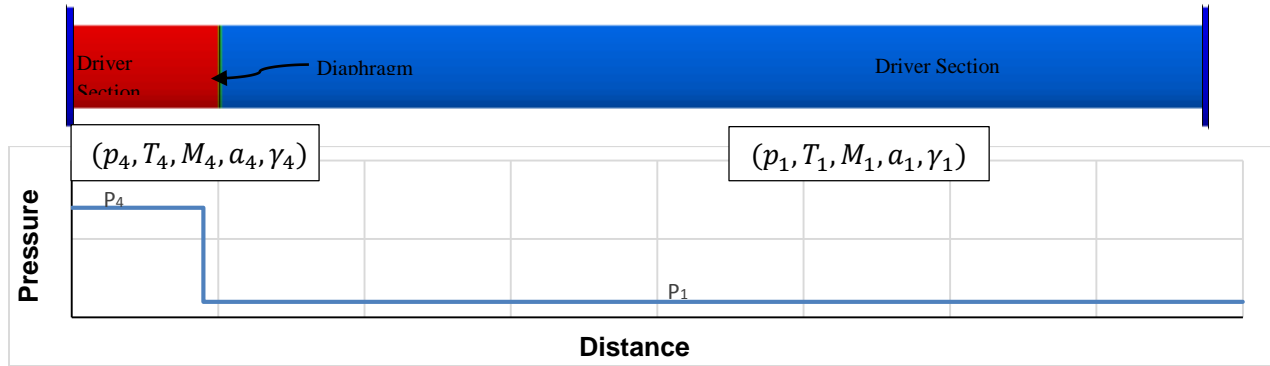
Figure 6-1. Pressure along the shock tube before rupturing the diaphragm (initial condition).
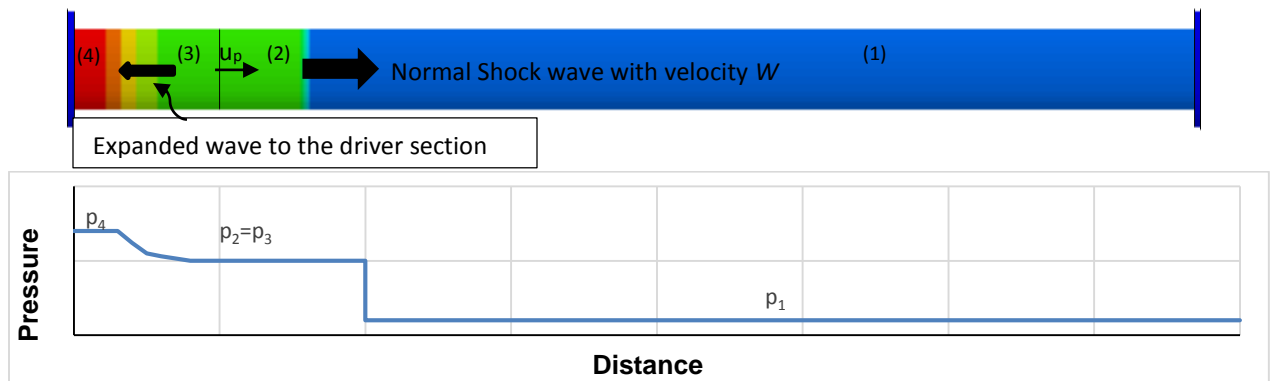
Figure 6-2. Pressure along the shock tube after rupturing the diaphragm.

Shock wave equations can be formed by using the mass, momentum, energy conservation equations in a controlled volume across the shock wave as shown in Figure 6.3.
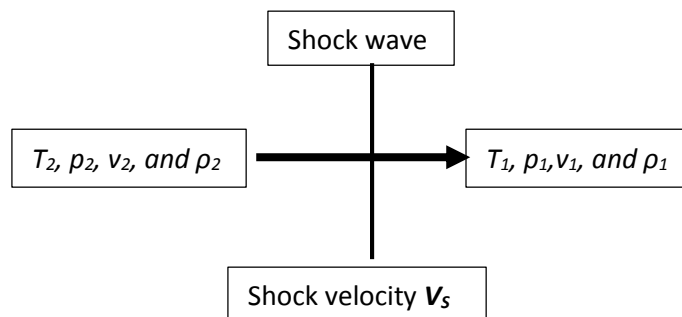
Figure 6-3. Control volume across the shock wave.

In this figure, V_s is the shock wave velocity and v_1 and v_2 are the gas particle velocities ahead and behind the shock wave, respectively. The relative velocities of gas particle to shock

wave velocity ahead and behind the shock wave are $u_1 = V_s - v_1$ and $u_2 = V_s - v_2$, respectively. The conservation equations for the control volume are as follows:

Continuity:
$$\rho_1 u_1 = \rho_2 u_2 \tag{6-1}$$

Momentum:
$$p_1 + \rho_1 u_1^2 = p_2 + \rho_2 u_2^2 \tag{6-2}$$

Energy:
$$h_1 + \frac{u_1^2}{2} = h_2 + \frac{u_2^2}{2} \tag{6-3}$$

Assuming the gas is an ideal gas in which $h = cpT = \frac{\gamma R}{\gamma - 1} T = \frac{\gamma}{\gamma - 1} \frac{p}{\rho}$ and using equation (6.3) leads to:

$$\frac{\gamma}{\gamma - 1} \frac{p_1}{\rho_1} + \frac{u_1^2}{2} = \frac{\gamma}{\gamma - 1} \frac{p_2}{\rho_2} + \frac{u_2^2}{2} \tag{6-4}$$

Using equations (6.1), (6.2), and (6.3) to rearranges equation (6.4):

$$\frac{p_2}{p_1} = \frac{1 - \frac{\gamma - 1}{\gamma + 1} \frac{\rho_1}{\rho_2}}{\frac{\rho_1}{\rho_2} - \frac{\gamma - 1}{\gamma + 1}} \tag{6-5}$$

$$\frac{\rho_2}{\rho_1} = \frac{\frac{\gamma - 1}{\gamma + 1} + \frac{p_2}{p_1}}{(\frac{\gamma - 1}{\gamma + 1}) \frac{p_2}{p_1} + 1} \tag{6-6}$$

Equations (6.5) and (6.6) are Rankine-Hugoniot equation and explain the gases property changes near the shock wave [132].

Substituting the shock Mach number ($M_{as} = \frac{W}{c_1}$) in which $c_1 = \sqrt{\gamma R T_1}$ and assuming $v_1 = 0$ results in:

$$\frac{p_2}{p_1} = 1 + \gamma M_{as}^2 (1 - \frac{\rho_2}{\rho_1}) \tag{6-7}$$

Combining equations (6.6) and (6.7) gives:

$$\frac{p_2}{p_1} = \frac{2\gamma M_{as}^2 - (\gamma - 1)}{\gamma + 1} \tag{6-8}$$

$$\frac{\rho_2}{\rho_1} = \frac{(\gamma + 1)M_{as}^2}{(\gamma - 1)M_{as}^2 + 2} \tag{6-9}$$

Equations (6.8) and (6.9) and available equations for ideal gas leads to:

$$\frac{T_2}{T_1} = \frac{(\gamma M_{as}^2 - \frac{\gamma - 1}{2})(\frac{\gamma - 1}{2} M_{as}^2 + 1)}{(\frac{\gamma - 1}{2})^2 M_{as}^2} \tag{6-10}$$

Theoretical ratios of a shock wave gas properties when it is propagate in the air are illustrated in Figure 6.4 [133].
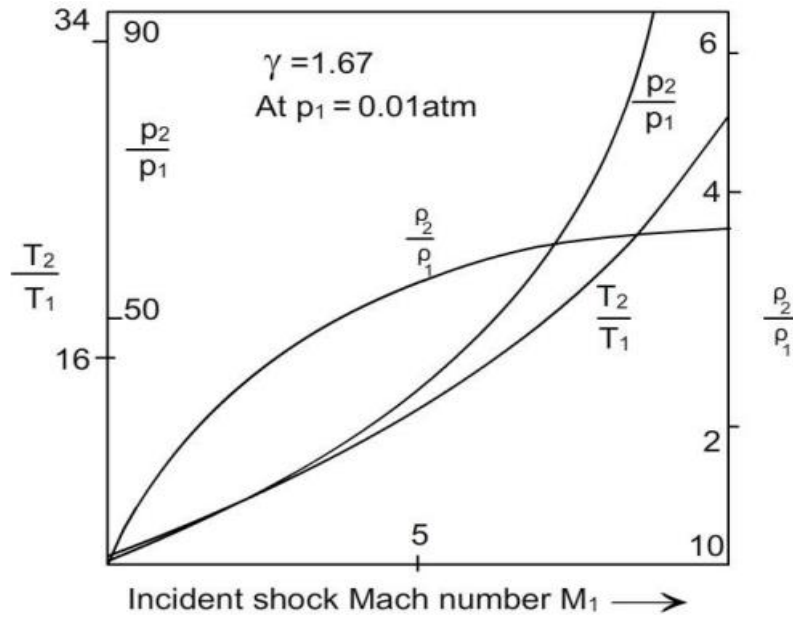
Figure 6-4. Theoretical ratios of a shocked gas properties [133].

6.2. Shock Tube Facility with Actuated Butterfly Valve

The available shock tube facility at NDSU has been fabricated using a low carbon steel tube. The inner diameter of the tube was 20.32 cm. The end of the driver section was closed and the other end of the tube (driven section) has been attached to the test section. Lengths of the driver and driven sections were 6.4 and 1.5 m, respectively. A Solenoid-Controlled Pneumatic-

Actuated Butterfly Valve has been used to separate the driver and driven sections. The pneumatic actuator was used to open the butterfly valve as faster as possible. If inside the driver section is not filled with high pressurized air, the required time for complete opening of the valve is around 500 milliseconds. Figure 6.5 shows the schematic of available shock tube at NDSU.
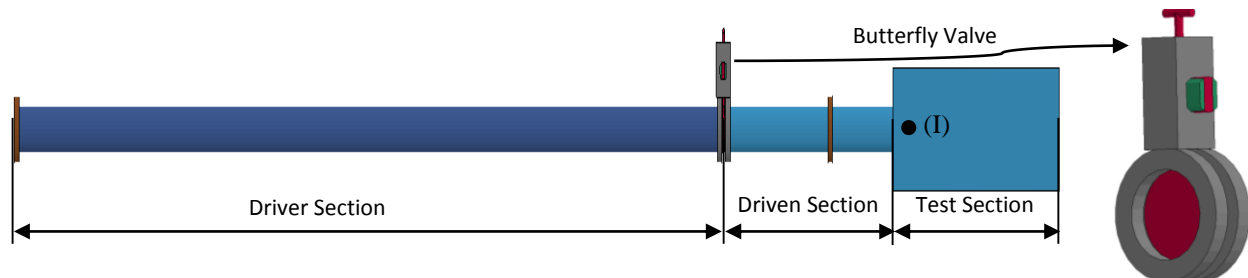
Figure 6-5. A schematic of the available shock tube facility at NDSU.

A dynamic pressure sensor is mounted in front of the driven section to monitor and record the pressure history in the test section as shown by point (I) in Figure 6.5. The sensor (ICP® Pressure Sensor, Model 113B21) is designed for shock tube and blast wave measurements by PCB Piezotronics, Inc. A data acquisition card by National Instruments (NI 9229) with a four analog channel has been used to collect the experimental data. The variation of the pressures when the driver section pressure was 50, 70, and 100 kPa were presented in Figure 6.6.
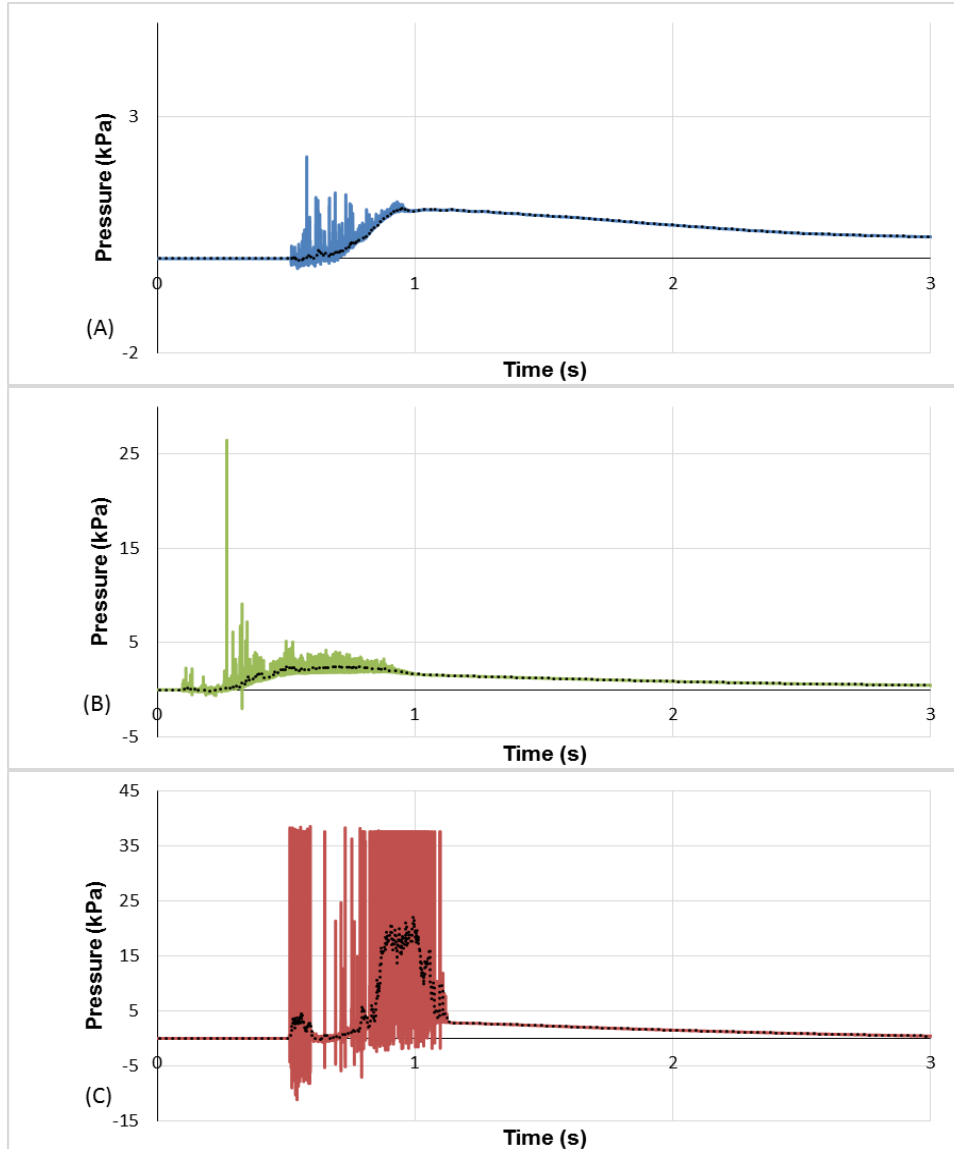
Figure 6-6. Variation of the pressures at point (I) when the driver section's pressure was set; (A) 50, (B) 70, and (C) 100 *kPa*.

The results indicated that the pressure varied in a relatively long period of time (few second versus the few millisecond). Moreover, in all cases, maximum values of the pressure at point (I) were noticeably less than the one at driver section. The produced shock wave at three different opening times for the valves i) 0, ii) 15, and iii)150 *ms* was simulated to better understand the effect of the opening time of the valve on the shock wave. . Variations of the

pressure with time in five different regions, along the shock tube were recorded and evaluated for each opening time of the valve as shown in Figure 6.7.
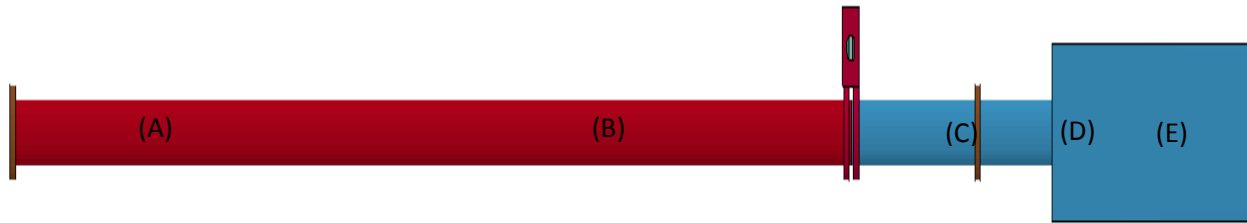
Figure 6-7. Selected regions along the shock tube to monitor the pressure history.

Variations of the pressure with time in different regions along the driver section (A and B), driven section (C), and test section (D and E) were presented in Figure 6.8. The results showed when the valve opening time was longer, the drop of the pressure in the driver section was smoother. However, when the valve was opened immediately (case 1) pressure behind the valve (region B) failed sharply to around 37 *kPa* and remains at this level for a few milliseconds (around 14.5 *ms*). This constant high level pressure would be due to the length of the driver section. After that the pressure decreased to ambient pressure smoothly. Consequently, when the valve was opened instantly the pressure in the driven section (region C) increased rapidly and stayed at a constant level for around 8 *ms*. Variation of the pressure in test section (areas D and E) illustrated that when the valve opening time was zero, the region in front of the driven section (region D) experienced both high over pressure which was similar to front shock wave (section 5.1) and negative pressure that was blow atmospheric pressure.
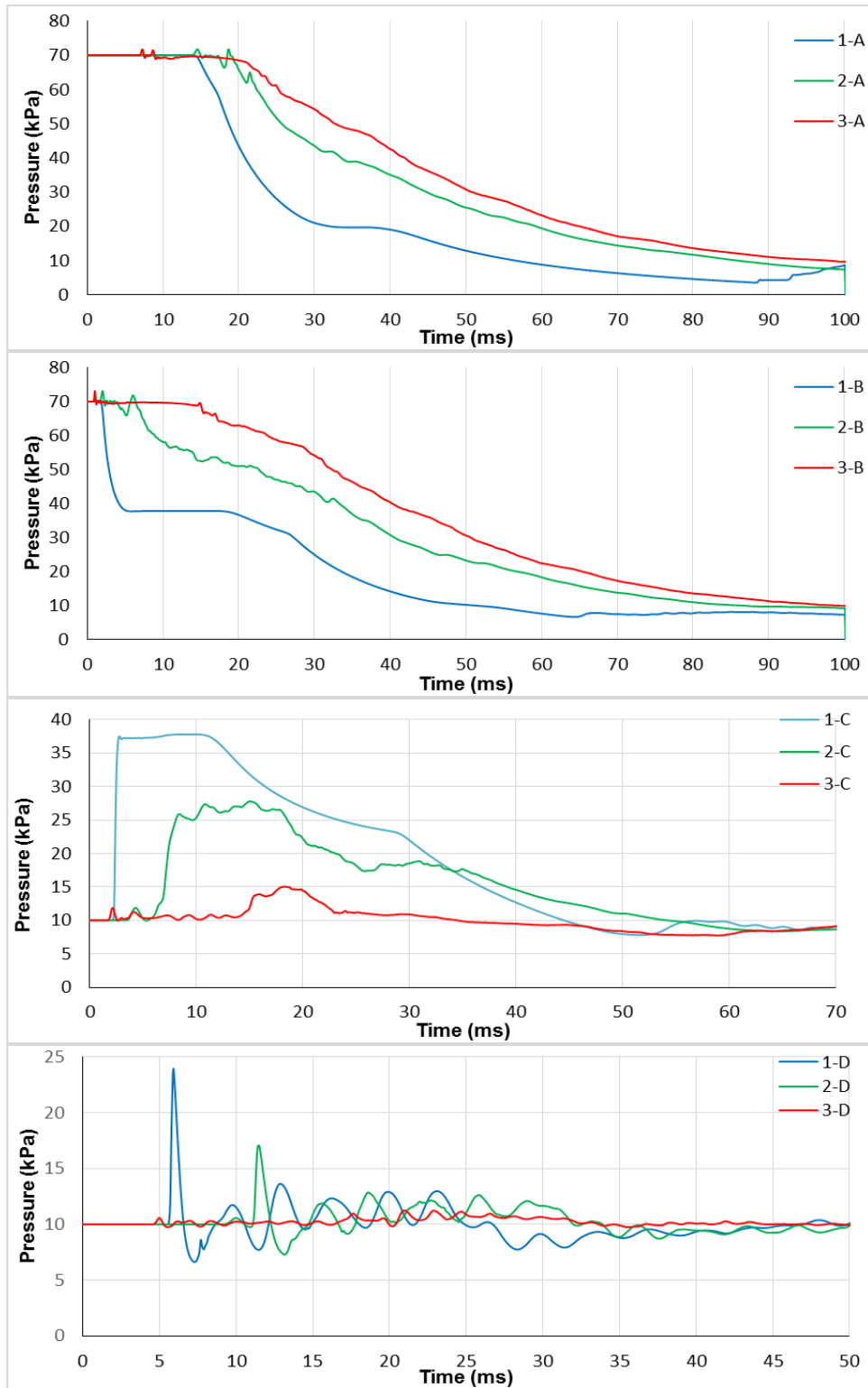
Figure 6-8. Variations of the pressure in selected regions (A, B, C, D, and E) along the shock tube by using different valves; (1) valve was opened immediately, (2) valve opening time was 15 *ms*, and (3) valve opening time was 150 *ms*.

113
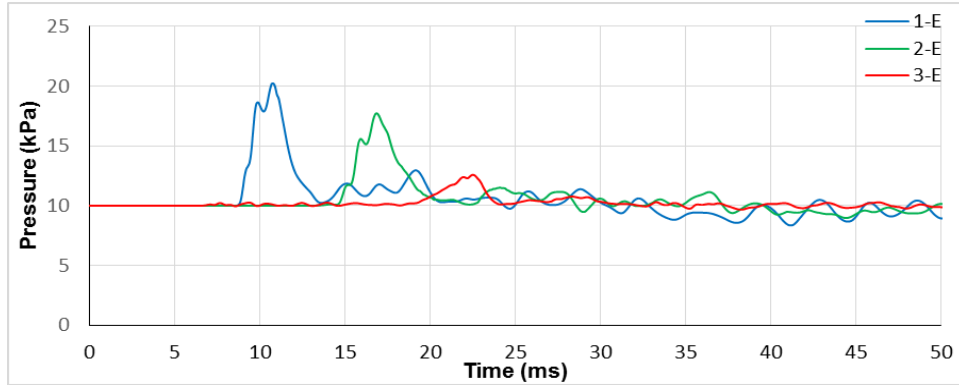
Figure 6.8. Variations of the pressure in selected regions (A, B, C, D, and E) along the shock tube by using different valves; (1) valve was opened immediately, (2) valve opening time was 15 *ms*, and (3) valve opening time was 150 *ms* (continued).

6.3. Conclusion

In this part of the work effect of the opening time of valves on the pressure history along the shock tube was studied numerically. The simulations results shown that the dimensions of driver and driven sections and the valve opening time affected the pressure history in the test section. Indeed, using a valve instead of diaphragm to separate the driver and driven sections introduced significant errors in the results. For future work the shock tube should be modified to acquire the pressure change history similar to what happen in blast situations.

114

7. CONCLUSION AND FUTURE WORKS

To study the mechanical responses of the human head under the ballistic impact and blast wave loads a 3-D nonlinear FE model was developed. The simulated human head neck model used in this work has a close proximity to a real human head geometry and components. The model has been validated against the experimental works. An advanced combat helmet (ACH) was also modeled as a ballistic helmet to be assembled to the human head model. The helmet was assembled with its padding system with its shell modelled as a transversely isotropic material. For ballistic impact simulations four different foam materials were used as padding to absorb the impact loads. Biomechanical responses of the head under the bullet hit from the front side with the helmet on were studied with different velocities of the bullet. Also the efficiency of the ballistic helmet with bullet striking the front of the helmet at different angles and locations (front, side, and back) were examined. Following conclusions were made through the ballistic impact simulations:

1- Material of the padding system has a major influence on the level of the load transferred to the head.

2- Maximum ICP will happen at the time of maximum acceleration of the head.

3- When the bullet hit the front of the helmet perpendicularly, brain experienced the maximum amount of ICP and shear stress.

4- Forefront impact is the most severe scenario due to minimum contact area of the paddings and the helmet in the direction of the load.

The above conclusions applies as long as the foams does not pass their stress-strain plateau constitutive region.

To simulate the blast wave propagation around the head-neck a coupling of empirical explosive blast load with the multi-material ALE formulation was used. The blast interaction with a solid object was also modeled using a penalty based FSI algorithm. A parametric study to obtain the optimum mesh size was done for the air (blast) domain to simulate the FSI of the blast waves and the human head accurately. The blast wave propagation modeling was successfully validated against experimental data in the free-air and other blast wave load simulation methods which other modeling procedures (purely Lagrangian method and ALE-MM method). Using the coupling method saved the computational costs with finer elements in the blast domain. The human head-neck model with and without a helmet, was exposed to some blast scenarios to study the efficiency of the helmet under the blast wave loads. The impact due to head orientation with respect to blast directions and the efficiency of the helmet under different blast scenarios were examined. To have a more realistic model under blast waves and to investigate the over-wash phenomena a torso was modelled attached to head model. The biomechanical responses of the brain with the head-neck model free, fixed, and with the full body were recorded under different blast scenarios. The results were compared and a good conclusions on the boundary conditions of the head were extracted. The following are some of the conclusions made through blast wave simulations:

1- The results indicated that protected heads experienced lower acceleration, lower maximum ICP, and lower shear stress than unprotected ones.

2- The performance of the helmet depended on the amount of coverage of the helmet in blast scenarios.

3- The boundary conditions of the head-neck model either free, fixed, or body included, had little influence on the early interactions with the blast waves and the brain response at the first few milliseconds (up to 6ms).

4- The boundary conditions of the head-neck model, free, fixed, or body included, particularly affected the shear stress after the initial interactions with the waves. In special, fixing the neck overemphasized the shear stress on the brainstem.

5- Overall, it was concluded that the results of the head-model alone is credible enough for the first few milliseconds at the early stages of the assault on the head.

7.1. Suggestions for Future Work

1- Since stress-strain constitutive curves of the padding foam materials are highly strain rate sensitive. It is recommended to characterize the currently used pad materials with different strain rates for modeling purposes.

2- Optimum arrangements of the pads in the padding system of the helmet under ballistic impacts or in interaction with blast waves can be obtained numerically.

3- In the work the effect of the padding material under the ballistic loads were examined. One suggestion is to study the effects of padding system arrangement and its material under blast loads.

4- Underwash phenomena is a noteworthy subject that can happen due to the blast waves. Studying the underwash phenomena with respect to various padding system arrangements under blast waves is also recommended.

5- Finite element modeling results should be validated against experimental data. It is suggested to use proper material and geometry for Hybrid III dummy head model in

blast simulations for reliable experimental results. Also reproduction of blasts

scenarios should be simulated in a more advanced shock tube environment facility.

8. REFERENCES

[1] http://www.sciencekids.co.nz/pictures/humanbody/cerebrumdiagram.html, in, 2014.

[2] E.K. Warrington, L. Weiskrantz, Further analysis of the prior learning effect in amnesic patients, Neuropsychologia, 16 (1978) 169-177.

[3] R.W. Broyles, L. Narine, S.R. Clarke, D.R. Baker, Factors associated with the likelihood of injury resulting from collisions between four-wheel drive vehicles and passenger cars, Accident Analysis & Prevention, 35 (2003) 677-681.

[4] http://www.cdc.gov/traumaticbraininjury/, in, 2014.

[5] http://www.brainline.org/content/2009/06/tbi-basics_pageall.html, (2014).

[6] http://dvbic.dcoe.mil/dod-worldwide-numbers-tbi, in, 2014.

[7] M. Inglese, S. Makani, G. Johnson, B.A. Cohen, J.A. Silver, O. Gonen, R.I. Grossman, Diffuse axonal injury in mild traumatic brain injury: a diffusion tensor imaging study, Journal of neurosurgery, 103 (2005) 298-303.

[8] A. Holbourn, Mechanics of head injuries, The Lancet, 242 (1943) 438-441.

[9] A.E. Hirsch, A.K. Ommaya, Protection from brain injury: The relative significance of translational and rotational motions of the head after impact, in, SAE Technical Paper, 1970.

[10] A.K. Ommaya, A.E. Hirsch, J.L. Martinez, The role of whiplash in cerebral concussion, in, SAE Technical Paper, 1966.

[11] E. Gurdjian, H. Lissner, F. Latimer, B. Haddad, J. Webster, Quantitative Determination of Acceleration and Intracranial Pressure in Experimental Head Injury Preliminary Report, Neurology, 3 (1953) 417-417.

[12] H.J. Mertz, P. Prasad, A.L. Irwin, Injury risk curves for children and adults in frontal and rear collisions, in, SAE Technical Paper, 1997.

[13] S. Standard, SNELL STANDARD FOR PROTECTIVE HEADGEAR For Use With Bicycles, in, 1995.

[14] F.M.V.S.S.A. REGULATIONS, Standard No. 218, in, U.S. DEPARTMENT OF TRANSPORTATION, 1999.

[15] E.S. Gurdjian, V.R. Hodgson, W. Hardy, L. Patrick, H. Lissner, Evaluation of the protective characteristics of helmets in sports, Journal of Trauma and Acute Care Surgery, 4 (1964) 309-324.

[16] C.W. Gadd, Use of a weighted-impulse criterion for estimating injury hazard, in, SAE Technical Paper, 1966.

[17] A. Ommaya, A. Hirsch, Tolerances for cerebral concussion from head impact and whiplash in primates, Journal of biomechanics, 4 (1971) 13-21.

[18] J. Newman, A generalized acceleration model for brain injury threshold (GAMBIT), in: Proc. IRCOBI Conf, 1986, pp. 121-131.

[19] J.A. Newman, N. Shewchenko, A proposed new biomechanical head injury assessment function-the maximum power index, in, SAE Technical Paper, 2000.

[20] A.K. OMMAYA, Head injury mechanisms and the concept of preventive management: a review and critical synthesis, Journal of neurotrauma, 12 (1995) 527-546.

[21] W.C. Moss, M.J. King, E.G. Blackman, Skull flexure from blast waves: a mechanism for brain injury with implications for helmet design, Physical review letters, 103 (2009) 108702.

[22] C. Ward, M. Chan, A. Nahum, Intracranial pressure–a brain injury criterion, in, SAE Technical Paper, 1980.

[23] A.C. Bain, D.F. Meaney, Tissue-level thresholds for axonal damage in an experimental model of central nervous system white matter injury, Journal of biomechanical engineering, 122 (2000) 615-622.

[24] L. Zhang, K.H. Yang, A.I. King, A proposed injury threshold for mild traumatic brain injury, Journal of biomechanical engineering, 126 (2004) 226-236.

[25] J. Galbraith, L. Thibault, D. Matteson, Mechanical and electrical responses of the squid giant axon to simple elongation, Journal of biomechanical engineering, 115 (1993) 13-22.

[26] B. Morrison 3rd, H.L. Cater, C. Wang, F.C. Thomas, C.T. Hung, G.A. Ateshian, L.E. Sundstrom, A tissue level tolerance criterion for living brain developed with an in vitro model of traumatic mechanical loading, Stapp car crash journal, 47 (2003) 93-105.

[27] E.G. Takhounts, R.H. Eppinger, J.Q. Campbell, R.E. Tannous, E.D. Power, L.S. Shook, On the development of the SIMon finite element head model, in, SAE Technical Paper, 2003.

[28] H.-S. Kang, R. Willinger, B.M. Diaw, B. Chinn, Validation of a 3D anatomic human head model and replication of head impact in motorcycle accident by finite element modeling, in, SAE Technical Paper, 1997.

[29] R.W. Anderson, C. Brown, P. Blumbergs, G. Scott, J. Finney, N. Jones, A. McLean, Mechanisms of axonal injury: an experimental and numerical study of a sheep model of head impact, in: Proceedings of the International Research Council on the Biomechanics of

Injury conference, International Research Council on Biomechanics of Injury, 1999, pp. 107-120.

[30] R. Willinger, D. Baumgartner, B. Chinn, M. Neale, Head tolerance limits derived from numerical replication of real world accidents, in: Proceedings of the International Research Council on the Biomechanics of Injury conference, International Research Council on Biomechanics of Injury, 2000, pp. 209-221.

[31] D. Baumgartner, R. Willinger, Numerical modeling of the human head under impact: new injury mechanisms and tolerance limits, in: IUTAM Symposium on Impact Biomechanics: From Fundamental Insights to Applications, Springer, 2005, pp. 195-203.

[32] V. Kostopoulos, Y. Markopoulos, G. Giannopoulos, D. Vlachos, Finite element analysis of impact damage response of composite motorcycle safety helmets, Composites Part B: Engineering, 33 (2002) 99-107.

[33] N. Mills, A. Gilchrist, Finite-element analysis of bicycle helmet oblique impacts, International Journal of Impact Engineering, 35 (2008) 1087-1101.

[34] P.K. Pinnoji, P. Mahajan, Finite element modelling of helmeted head impact under frontal loading, Sadhana, 32 (2007) 445-458.

[35] http://www.fairview.org/healthlibrary/Article/83352, in, 2014.

[36] M. Kozielski, T. Buchwald, M. Szybowicz, Z. Błaszczak, A. Piotrowski, B. Ciesielczyk, Determination of composition and structure of spongy bone tissue in human head of femur by Raman spectral mapping, Journal of Materials Science: Materials in Medicine, 22 (2011) 1653-1661.

[37] J. Van Hoof, D. Cronin, M. Worswick, K. Williams, D. Nandlall, Numerical head and composite helmet models to predict blunt trauma, in: Proceedings of 19th international symposium on ballistics, 2001, pp. 7-11.

[38] D. Baumgartner, R. Willinger, Finite element modelling of human head injuries caused by ballistic projectiles, in: Proceedings of RTO specialist meeting, 2003.

[39] M. Aare, S. Kleiven, Evaluation of head response to ballistic helmet impacts using the finite element method, International journal of impact engineering, 34 (2007) 596-608.

[40] M. Salimi Jazi, Rezaei, A., Karami, G., Azarmi, F., and Ziejewski M, A computational study on biomechanics of brain of a helmeted human head model exposed to blast waves from different orientations, in: Proceedings of the 11th International Symposium, Computer Methods in Biomechanics and Biomedical Engineering Salt Lake City, Utah, USA, 2013.

[41] M.S. Jazi, A. Rezaei, G. Karami, F. Azarmi, M. Ziejewski, Helmet-Head Interactions under the Blast, in: JOURNAL OF HEAD TRAUMA REHABILITATION, LIPPINCOTT

121

WILLIAMS & WILKINS 530 WALNUT ST, PHILADELPHIA, PA 19106-3621 USA, 2012, pp. E40-E41.

[42] M.S. Jazi, A. Rezaei, G. Karami, F. Azarmi, M. Ziejewski, A computational study of influence of helmet padding materials on the human brain under ballistic impacts, Computer methods in biomechanics and biomedical engineering, (2013) 1-15.

[43] A. Anzelius, The effect of an impact on a spherical liquid mass, 1943.

[44] H.S. Chan, Mathematical model for closed head impact, in, SAE Technical Paper, 1974.

[45] V. Kenner, W. Goldsmith, Impact on a simple physical model of the head, Journal of biomechanics, 6 (1973) 1-11.

[46] T.B. Khalil, R.P. Hubbard, Parametric study of head response by finite element modeling, Journal of Biomechanics, 10 (1977) 119-132.

[47] C.H. Hardy, P.V. Marcal, Elastic analysis of a skull, Journal of Applied Mechanics, 40 (1973) 838-842.

[48] R.R. Hosey, Y.K. Liu, A homeomorphic finite element model of the human head and neck, Finite elements in biomechanics, (1982) 379-401.

[49] R. Nickell, P. Marcal, In-Vacuo Modal Dynamic Response of the Human Skull, Journal of Manufacturing Science and Engineering, 96 (1974) 490-494.

[50] T. Shugar, Transient structural response of the linear skull-brain system, in, SAE Technical Paper, 1975.

[51] C.C. Ward, Finite element models of the head and their use in brain injury research, in, SAE Technical Paper, 1982.

[52] A.M. Nahum, Intracranial pressure dynamics during head impact, in: 21st Stapp Car Crash Conference, 1977, 1977.

[53] T.B. Khalil, D.C. Viano, Critical issues in finite element modeling of head impact, in, SAE Technical Paper, 1982.

[54] L. Voo, S. Kumaresan, F.A. Pintar, N. Yoganandan, A. Sances Jr, Finite-element models of the human head, Medical and Biological Engineering and Computing, 34 (1996) 375-381.

[55] J.S. Ruan, T.B. Khalil, A.I. King, Finite element modeling of direct head impact, in: Stapp Car Crash Conference, 37th, 1993, San Antonio, Texas, USA, 1993.

[56] C. Zhou, T.B. Khalil, A. King, A new model comparing impact responses of the homogeneous and inhomogeneous human brain, in: SAE PUBLICATION P-299.

PROCEEDINGS OF THE 39TH STAPP CAR CRASH CONFERENCE, NOVEMBER 8-10, 1995, SAN DIEGO, CALIFORNIA, USA (SAE TECHNICAL PAPER 952714), 1995.

[57] R. Willinger, H.-S. Kang, B. Diaw, Three-dimensional human head finite-element model validation against two experimental impacts, Annals of biomedical engineering, 27 (1999) 403-410.

[58] S. Kleiven, H. von Holst, Consequences of head size following trauma to the human head, Journal of Biomechanics, 35 (2002) 153-160.

[59] A.C. S. Mukherjee, B. Karthikeyan Review of Mechanical Properties of Human Body Soft Tissues in the Head, neck and spine, in.

[60] W.N. Hardy, M.J. Mason, C.D. Foster, C.S. Shah, J.M. Kopacz, K.H. Yang, A.I. King, J. Bishop, M. Bey, W. Anderst, A study of the response of the human cadaver head to impact, Stapp car crash journal, 51 (2007) 17.

[61] K. Baeck, J. Goffin, J. Vander Sloten, The use of different CSF representations in a numerical head model and their effect on the results of FE head impact analyses, in: European LS-DYNA users conference 2011. Proceedings 8th European LS-DYNA users conference, Strasbourg, France, 2011.

[62] P.A. Taylor, C.C. Ford, Simulation of blast-induced early-time intracranial wave physics leading to traumatic brain injury, Journal of biomechanical engineering, 131 (2009) 61007.

[63] T. Horgan, M.D. Gilchrist, The creation of three-dimensional finite element models for simulating head impact biomechanics, International Journal of Crashworthiness, 8 (2003) 353-366.

[64] L.-D.T. Manual, in, Livermore Software Technology Corporation, 2007.

[65] S. Kleiven, W.N. Hardy, Correlation of an FE model of the human head with local brain motion-consequences for injury prediction, in: SAE CONFERENCE PROCEEDINGS P, SAE; 1999, 2002, pp. 123-144.

[66] J. Ruan, T. Khalil, A. King, Human head dynamic response to side impact by finite element modeling, Journal of Biomechanical Engineering, 113 (1991) 276-283.

[67] S. Kleiven, Influence of impact direction on the human head in prediction of subdural hematoma, Journal of neurotrauma, 20 (2003) 365-379.

[68] M. Chafi, G. Karami, M. Ziejewski, Biomechanical assessment of brain dynamic responses due to blast pressure waves, Annals of biomedical engineering, 38 (2010) 490-504.

[69] K. Mendis, R. Stalnaker, S. Advani, A constitutive relationship for large deformation finite element modeling of brain tissue, Journal of Biomechanical Engineering, 117 (1995) 279.

[70] M.S. Jazi, A. Rezaei, G. Karami, F. Azarmi, M. Ziejewski, Effects of Attached Body on Biomechanical Response of the Helmeted Human Head Under Blast, in: ASME 2013 International Mechanical Engineering Congress and Exposition, American Society of Mechanical Engineers, 2013, pp. V03AT03A077-V003AT003A077.

[71] Z. Aslan, R. Karakuzu, B. Okutan, The response of laminated composite plates under low-velocity impact loading, Composite Structures, 59 (2003) 119-127.

[72] W.N. Hardy, C.D. Foster, M.J. Mason, K.H. Yang, A.I. King, S. Tashman, Investigation of Head Injury Mechanisms Using Neutral Density Technology and High-Speed Biplanar X-ray, Stapp Car Crash Journal, 45 (2001) 337.

[73] http://www.militarytrader.com/military-trader-news/the_first_modern_steel_combat_helmet_the_french_adrian, (2014).

[74] http://www.theocadcollection.com/the-m1-helmet-of-world-war-two---a-basic-overview.html, (2014).

[75] http://www.operation-helmet.org/helmet/#PASGT, (2014).

[76] http://www.military.com/equipment/advanced-combat-helmet-ach, (2014).

[77] M.A. Silva, C. Cismaşiu, C. Chiorean, Numerical simulation of ballistic impact on composite laminates, International Journal of Impact Engineering, 31 (2005) 289-306.

[78] P. Viot, L. Maheo, A. Mercier, BEHAVIOUR OF POLYMERIC MULTISCALE FOAM UNDER DYNAMIC LOADING-STUDY OF THE INFLUENCE OF THE DENSITY AND THE WALLS OF BEADS.

[79] L.J. Gibson, M.F. Ashby, Cellular solids: structure and properties, Cambridge university press, 1999.

[80] M. Avalle, G. Belingardi, R. Montanini, Characterization of polymeric structural foams under compressive impact loading by means of energy-absorption diagram, International Journal of Impact Engineering, 25 (2001) 455-472.

[81] J. Miltz, O. Ramon, Energy absorption characteristics of polymeric foams used as cushioning materials, Polymer Engineering & Science, 30 (1990) 129-133.

[82] O. Ramon, S. Mizrahi, J. Miltz, Mechanical properties and behavior of open cell foams used as cushioning materials, Polymer Engineering & Science, 30 (1990) 197-201.

[83] J. Zhang, N. Kikuchi, V. Li, A. Yee, G. Nusholtz, Constitutive modeling of polymeric foam material subjected to dynamic crash loading, International journal of impact engineering, 21 (1998) 369-386.

[84] F. Rueda, L. Cui, M. Gilchrist, Optimisation of energy absorbing liner for equestrian helmets. Part I: Layered foam liner, Materials & Design, 30 (2009) 3405-3413.

[85] L. Cui, F. Rueda, M. Gilchrist, Optimisation of energy absorbing liner for equestrian helmets. Part II: Functionally graded foam liner, Materials & Design, 30 (2009) 3414-3419.

[86] K.H. Digges, Injury measurements and criteria, Models for Aircrew Safety Assessment: Uses, Limitations and Requirements, (1999).

[87] N. Naik, A. Doshi, Ballistic impact behaviour of thick composites: parametric studies, Composite structures, 82 (2008) 447-464.

[88] N. Naik, P. Shrirao, Composite structures under ballistic impact, Composite structures, 66 (2004) 579-590.

[89] N. Naik, P. Shrirao, B. Reddy, Ballistic impact behaviour of woven fabric composites: Parametric studies, Materials Science and Engineering: A, 412 (2005) 104-116.

[90] C.X. Wang, A. Shuaib, Involvement of inflammatory cytokines in central nervous system injury, Progress in neurobiology, 67 (2002) 161-172.

[91] A.W. Carroll, C.A. Soderstrom, A new nonpenetrating ballistic injury, Annals of surgery, 188 (1978) 753.

[92] E. Liden, R. Berlin, B. Janzon, B. Schantz, T. Seeman, Some observations relating to behind-body armour blunt trauma effects caused by ballistic impact, The Journal of Trauma and Acute Care Surgery, 28 (1988) S145-S148.

[93] Z. Qiu, AM17 Protective Functional Evaluation of Helmet against Ballistic Impact, in, Bachelor's Thesis, National University of Singapore 2007, 2008.

[94] J. Yang, J. Dai, Simulation-based assessment of rear effect to ballistic helmet impact, Computer-Aided Design and Applications, 7 (2010) 59-73.

[95] C. Tham, V. Tan, H. Lee, Ballistic impact of a KEVLAR® helmet: Experiment and simulations, International Journal of Impact Engineering, 35 (2008) 304-318.

[96] R. Othman, Finite Element Analysis Of Composite Ballistics Helmet Subjected To High Velocity Impact, in, Universiti Sains Malaysia, 2009.

[97] Y.S. Lee, N.H. Park, H.S. Yoon, Dynamic mechanical characteristics of expanded polypropylene foams, Journal of cellular plastics, 46 (2010) 43-55.

[98] K.H. Yang, H. Mao, C. Wagner, F. Zhu, C.C. Chou, A.I. King, Modeling of the brain for injury prevention, in: Neural tissue biomechanics, Springer, 2011, pp. 69-120.

[99] P.A. Taylor, C.C. Ford, Simulation of head impact leading to traumatic brain injury, in, DTIC Document, 2006.

[100] J.H. McElhaney, J.L. Fogle, J.W. Melvin, R.R. Haynes, V.L. Roberts, N.M. Alem, Mechanical properties of cranial bone, Journal of Biomechanics, 3 (1970) 495-511.

[101] S. Okie, Traumatic brain injury in the war zone, New England Journal of Medicine, 352 (2005) 2043-2047.

[102] D.F. Moore, A. Jérusalem, M. Nyein, L. Noels, M.S. Jaffee, R.A. Radovitzky, Computational biology—modeling of primary blast effects on the central nervous system, Neuroimage, 47 (2009) T10-T20.

[103] A. Courtney, M. Courtney, A thoracic mechanism of mild traumatic brain injury due to blast pressure waves, Medical Hypotheses, 72 (2009) 76-83.

[104] S.C. Matthews, I.A. Strigo, A.N. Simmons, R.M. O'Connell, L.E. Reinhardt, S.A. Moseley, A multimodal imaging study in US veterans of Operations Iraqi and Enduring Freedom with and without major depression after blast-related concussion, Neuroimage, 54 (2011) S69-S75.

[105] S. Ganpule, A. Alai, E. Plougonven, N. Chandra, Mechanics of blast loading on the head models in the study of traumatic brain injury using experimental and computational approaches, Biomechanics and modeling in mechanobiology, (2012) 1-21.

[106] S. Ganpule, L. Gu, A. Alai, N. Chandra, Role of helmet in the mechanics of shock wave propagation under blast loading conditions, Computer methods in biomechanics and biomedical engineering, 15 (2012) 1233-1244.

[107] H.L. Lew, J.H. Poole, S. Alvarez, W. Moore, Soldiers with occult traumatic brain injury, American journal of physical medicine & rehabilitation, 84 (2005) 393-398.

[108] M.S. Xydakis, V.S. Bebarta, C.D. Harrison, J.C. Conner, G.A. Grant, A.S. Robbins, Tympanic-membrane perforation as a marker of concussive brain injury in Iraq, New England Journal of Medicine, 357 (2007) 830-831.

[109] D. Mott, D. Schwer, T. Young, J. Levine, J.-P. Dionne, A. Makris, G. Hubler, Blast-induced pressure fields beneath a military helmet for non-lethal threats, in: APS Division of Fluid Dynamics Meeting Abstracts, 2008.

[110] D.R. Mott, T.R. Young Jr, D.A. Schwer, Blast Loading on the Head Under a Military Helmet: Effect of Face Shield and Mandible Protection1, (2014).

[111] J. Li, K.Y. Seng, A biomechanical computational study of the role of helmet pads in mitigating blast-induced traumatic brain injury, in: 6th World Congress of Biomechanics (WCB 2010). August 1-6, 2010 Singapore, Springer, 2010, pp. 1518-1521.

[112] M. Grujicic, W. Bell, B. Pandurangan, T. He, Blast-wave impact-mitigation capability of polyurea when used as helmet suspension-pad material, Materials & Design, 31 (2010) 4050-4065.

[113] A. Rezaei, Salimi Jazi, and M., Karami, G., Computational Modeling of Human Head under Blast in Confined and Open Spaces- Primary Blast Injury, International Journal for Numerical Methods in Biomedical Engineering, (2012).

[114] M.S. Chafi, V. Dirisala, G. Karami, M. Ziejewski, A finite element method parametric study of the dynamic response of the human brain with different cerebrospinal fluid constitutive properties, Proceedings of the Institution of Mechanical Engineers, Part H: Journal of Engineering in Medicine, 223 (2009) 1003-1019.

[115] L. Gu, M.S. Chafi, S. Ganpule, N. Chandra, The influence of heterogeneous meninges on the brain mechanics under primary blast loading, Composites Part B: Engineering, 43 (2012) 3160-3166.

[116] T.P. Slavik, A coupling of empirical explosive blast loads to ALE air domains in LS-DYNA®, in: IOP Conference Series: Materials Science and Engineering, IOP Publishing, 2010, pp. 012146.

[117] W.E. Baker, Explosions in air, University of Texas Press Austin, 1973.

[118] C.N. Kingery, G. Bulmash, Air blast parameters from TNT spherical air burst and hemispherical surface burst, Ballistic Research Laboratories, 1984.

[119] M. Larcher, Simulation of the Effects of an Air Blast Wave, JRC Technical Note, Pubsy JRC41337, Ispra, (2007).

[120] I.O. Pericevic, M. Moatamedi, Application of the penalty coupling method for the analysis of blood vessels, European Journal of Computational Mechanics/Revue Européenne de Mécanique Numérique, 16 (2007) 537-548.

[121] H. Huang, M. Lee, S. Lee, W. Chiu, L. Pan, C. Chen, Finite element analysis of brain contusion: an indirect impact study, Medical and Biological Engineering and Computing, 38 (2000) 253-259.

[122] J.H. Stuhmiller, Blast injury, translating research into operational medicine, Military Quantitative Physiology: Problems and Concepts in Military Operational Medicine, (2008) 267-302.

[123] A.I. King, K.H. Yang, L. Zhang, W. Hardy, D.C. Viano, Is head injury caused by linear or angular acceleration, in: IRCOBI conference, 2003, pp. 1-12.

[124] J. Hutchinson, M.J. Kaiser, H.M. Lankarani, The head injury criterion (HIC) functional, Applied mathematics and computation, 96 (1998) 1-16.

[125] P.A. Lockhart, Primary blast injury of the head: numerical prediction and evaluation of protection, (2010).

[126] J.H. Stuhmiller, Y. Phillips, D. Richmond, The physics and mechanisms of primary blast injury, Conventional warfare: ballistic, blast, and burn injuries. Washington, DC: Office of the Surgeon General of the US Army, 241270 (1991).

[127] J.M.J.R.V.L.P.H.D.U.o.M.H.S.R.I.P.O.N.C. McElhaney, Dynamic characteristics of the tissues of the head, Perspectives in Biomedical Engineering. Proceedings of a Symposium., (1973) 215-222.

[128] M. Ziejewski, G. Karami, W. Orrison Jr, E. Hanson, Dynamic response of head under vehicle crash loading, in: 21st International Technical Conference on the Enhanced Safety of Vehicles. Stuttgart, Germany, paper, 2009.

[129] R.A. Bauman, G. Ling, L. Tong, A. Januszkiewicz, D. Agoston, N. Delanerolle, Y. Kim, D. Ritzel, R. Bell, J. Ecklund, An introductory characterization of a combat-casualty-care relevant swine model of closed head injury resulting from exposure to explosive blast, Journal of neurotrauma, 26 (2009) 841-860.

[130] M. Anderson, B. Puranik, J. Oakley, P. Brooks, R. Bonazza, Shock tube investigation of hydrodynamic issues related to inertial confinement fusion, Shock Waves, 10 (2000) 377-387.

[131] A. Al-Falahi, M. Yusoff, T. Yusaf, Development of a short duration hypersonic test facility at Universiti Tenaga Nasional, Institution of Engineers, Malaysia. Journal, 69 (2008) 19-25.

[132] N.N. Kleinschmit, A shock tube technique for blast wave simulation and studies of flow structure interactions in shock tube blast experiments, (2011).

[133] J.D. Anderson, Modern compressible flow with historical perspective, 2003.